Measurement of Localized Oxygen Extraction Fraction in Brain using Magnetic Resonance Imaging



Caitlin Fern O'Brien

Supervisors: Professor Peter Jezzard, Dr Thomas Okell

University of Oxford

This dissertation is submitted for the degree of

Doctor of Philosophy

Jesus College Trinity 2019

List of publications arising from this thesis

Journal Articles

1. **O'Brien C**, Okell TW, Chiew M, Jezzard P. Volume-localized measurement of oxygen extraction fraction in the brain using MRI. *Magn Reson Med* . 2019; 82(4): 1412–1423

Conference Proceedings

1. **O'Brien C**, Okell T, Jezzard P. Spatially localised measurements of oxygen extraction fraction using SL-TRUST. In Proc. Intl. Soc. Mag. Reson. Med., Honolulu, HI, 2017.
2. **O'Brien C**, Okell T, Jezzard P. Regional OEF measurements in the middle cerebral artery territory using combined SL-TRUST and WET saturation scheme. In Proc. Intl. Soc. Mag. Reson. Med., Paris, France, 2018.
3. **O'Brien C**, Okell T, Jezzard P. Reproducibility of SL-TRUST for Regional Cerebral OEF. In Proc. Intl. Soc. Mag. Reson. Med., Montreal, CA, 2019.
4. **O'Brien C**, Okell T, Chiew M, Jezzard P. Oxygen Extraction Fraction Mapping using Remote Sensing: Spatially Encoded T2-Relaxation-Under-Spin-Tagging (SE-TRUST). In Proc. Intl. Soc. Mag. Reson. Med., Sydney, Australia, 2020.
5. Tong Y, Jezzard P, **O'Brien C**, Clarke W. Mapping oxygen extraction fraction using a tailored parallel transmission RF pulse at 7 T. In Proc. Intl. Soc. Mag. Reson. Med., Sydney, Australia, 2020.

Acknowledgements

If I were to give any new student about to embark on a PhD some advice it would be to pick the supervisor rather than the project, and I could not have picked better in Peter and Tom. Over the past few years Peter has dedicated a tremendous amount of his time to helping, guiding, and teaching me, and has also provided sympathy and advice in tough times. Tom, and his dynamic duo/partner in crime Mark, have been so generous with their genius and input (and code!) at every stage. I am so grateful for all of your advice and patience.

A big thanks to everyone at FMRIB, especially Alex, Will, Rob, and Joe for their help and the unsung heroes in the IT department, Dave, Geoff, and Duncan. FMRIB also granted me some incredibly inspiring female role models in Karla, Liv, Emma, Nadine, Joanna, Kiyana, Irene, and Janine, however a special thanks goes to Sophie and Amy for helping form the new generation of female physicists at WIN.

Thank you to Jesus College for their continued financial support which has allowed me to attend multiple international conferences in every corner of the globe, at no personal financial cost.

Thank you to Alison, Peter & the nurses at AVIC for their time and support. You made data collection enjoyable, even in the most overwhelming and stressful of times.

The team at SPMIC, and especially Matt Brookes, for fostering my interest in medical physics all those years ago and for always looking out for me. Thank you for allowing me to continue to be a part of your family at every ISMRM, and at every visit back to the centre. You make MR feel like home.

It has been a crazy journey these past four years huge thanks to those who joined me, and helped me through. There have been so many friendships built both in laughter and in adversity.

Thank you to my various flatmates and other residents of HP throughout the years, for good times and good food. My original girl gang, the varsity gymnastics group of 2015, shine on you crazy diamonds. Thank you to Gina, Kathy, Becca, Daisy, Elliot, the

McDermott family, Consti, Sam, Izzie, Sinthuja, Emma, and the ONBI 2015 cohort, especially Sven, Gilad, and Emma, for your support and continued friendship.

To Adam, words aren't enough. Thank you for bringing such joy and love into my life.

To the best group of people ever to have walked this planet, salsa danced in London, and pole danced at weddings: Adam, David, Alex, Dan, Jakob, Warren, Tim and all of your +1s. You are my people and I can't imagine living life without you there every step of the way.

ChrisO and Jillbo, you gave me opportunities I never dreamed of. To the girls of OUWLRC, especially my Boat Race crews of 2018 & 2019, and EUSA crew of 2019, it is a privilege to have shared the very best as well as the very worst moments with you. We are superwomen.

Finally, Emma, Susannah, Jenny, Terry, Mum, and Dad. The knowledge that you will catch me if I fall, has allowed me to take leaps bigger than I ever imagined. I am extraordinarily lucky to be just one in a line of Dr Fern's/O'Brien's. I love you all. Takk fyrir mig.

Abstract

Magnetic resonance imaging (MRI) is a non-invasive medical imaging technique which, thanks to the variety of both structural and functional information it provides, is increasingly used throughout the world for clinical diagnosis. Due to the different magnetic properties of haemoglobin when it is bound to oxygen, MRI is sensitive to the oxygen saturation levels of the blood, however, accurate measurement of this property remains challenging in the brain. Specifically, there does not yet exist a robust MR method for quantifying regional differences in brain tissue oxygenation, which can provide important diagnostic information in cases where oxygen delivery to a specific region of the brain may be impaired, e.g. in stroke. In this thesis a new method for measuring the oxygen extraction fraction of tissue in the brain on a regional level is presented. The technique is called Selective Localized T2-Relaxation-Under-Spin-Tagging, or SL-TRUST and measures the oxygen saturation of outflowing venous blood in the superior sagittal sinus.

Using SL-TRUST venous oxygen saturation measurements are achieved in individual brain hemispheres and in a smaller tissue region, approximately 70x70x80 mm^3, above the middle cerebral artery. Comparison of two contralateral regions can be achieved in a scan time of less than 5 minutes. The robustness of SL-TRUST is assessed in healthy volunteers in a reproducibility study and the coefficients of variation for regional measurements found to be comparable to those of global measurements.

SL-TRUST is developed further as a method of mapping the oxygenation of venous blood from across the whole brain using phase encoding methods. Low resolution T2 maps in healthy volunteers are obtained as proof-of-concept of this method.

Table of Contents

Table of Contents x

List of Figures xiii

List of Tables xvi

List of Abbreviations xvii

Chapter 1 Motivation and thesis outline 1

1.1 Thesis Outline 2

Chapter 2 Introduction 5

2.1 Blood and brain physiology 5

2.1.1. Oxygen transportation and haemoglobin 6

2.1.2. Oxygen extraction fraction (OEF) 9

2.1.3. Brain vascular system 12

2.2 Measuring blood oxygen saturation 14

2.2.1 Positron-emission tomography (PET) 15

2.2.2 Near infrared spectroscopy (NIRS) 16

2.2.3 Magnetic resonance imaging (MRI) 17

2.3 MRI sequence building blocks 18

2.3.1 Adiabatic pulses 21

2.3.2 Phase cycling 23

2.4 Image formation 26

2.4.1 Partial Fourier sampling 28

2.4.2 Image reconstruction: coil combination methods 30

2.5 Isolating blood signal in MRI 33

2.5.1 Background saturation & suppression 34

2.5.2 Imaging moving blood 37

2.5.3 Velocity and acceleration selective techniques 38

2.5.4 Flow or velocity compensated imaging 40

2.6 MRI perfusion imaging 41

2.6.1 Arterial spin labelling (ASL) 42
2.7 MRI oxygen imaging 45
2.7.1 Calibrated BOLD 45
2.7.2 T2 based methods 49
2.7.3 QUIXOTIC 51
2.7.4 VSEAN 52
2.7.5 TRU-PC 53
2.7.6 TRUST 54
Chapter 3 Selective Localized T2-Relaxation-Under-Spin-Tagging 57
3.1 Introduction 57
3.2 T2-Relaxation-Under-Spin-Tagging 58
3.3 Selective Localized T2-Relaxation-Under-Spin-Tagging 60
3.4 Optimizing sequence timings 64
3.4.1 Inversion time TI 64
3.4.2 Repetition time TR 66
3.5 Spatial saturation 69
3.5.1 WET saturation 70
3.5.2 Cosine modulation 72
3.6 Signal instability 75
3.6.1 Flow-compensated readout 77
3.6.2 Background suppression 79
3.7 Post processing 83
3.7.1 Motion correction 84
3.7.2 Adaptive combine coil reconstruction 85
3.8 Discussion 88
Chapter 4 Spatially localized measures of OEF using SL-TRUST 93
4.1 Introduction 93
4.2 Measuring venous blood haematocrit using MRI 94
4.2.1 Measuring T1 97
4.3 SL-TRUST reproducibility study 98
4.3.1 Data collection 100
4.3.2 Coefficients of Variation 101
4.3.3 T2 and OEF for TRUST and SL-TRUST using uniform haematocrit 102
4.3.4 T2 and OEF for TRUST and SL-TRUST using subject-specific haematocrit 108

4.3.5 Sensitivity to changes in OEF 109
4.4 Application of SL-TRUST in a stroke population 113
4.5 Discussion 116
Chapter 5 Remote reconstruction of SL-TRUST T2 maps using phase encoding 119
5.1 Remote spatial encoding in NMR 120
5.1.1 VENTI: Venous Territory Imaging using Remote Sensing 123
5.1.2 Theory & phantom reconstruction 124
5.2 Remote reconstruction in SL-TRUST 130
5.2.1 Acquisition 131
5.2.2 Reconstruction 132
5.2.3 Partial Fourier reconstruction 135
5.3 Validation and optimization 139
5.3.1 Validation: spatial dependence 139
5.3.2 Optimization: TI dependence 142
5.4 T2 mapping in healthy controls 143
5.5 Discussion 147
Chapter 6 Conclusions, recommendations & future work 151
6.1 Summary 151
6.2 On-going and future work 153
6.2.1 Inversion time recommendations 153
6.2.2 SL-TRUST without pairwise subtraction 154
6.2.3 Compressed sensing in phase encoded SL-TRUST 157
6.2.4 Applying SL-TRUST at 7 Tesla 158
6.3 Final remarks 159
References 160

List of Figures

Figure 2.1 Oxygen dissociation curve 7

Figure 2.2 Increase in OEF following stroke due to reduced CBF 11

Figure 2.3 Cell death of cells distal to the capillaries as a result of a drop in venous partial pressure 12

Figure 2.4 A gadolinium enhanced MR Venogram (MRV) showing the superior sagittal sinus 13

Figure 2.5 Absorption spectra for oxygenated and deoxygenated haemoglobin 16

Figure 2.6 Amplitude and frequency sweep of an adiabatic hyperbolic secant inversion pulse 22

Figure 2.7 Path of vector M for an adiabatic hyperbolic secant inversion pulse 23

Figure 2.8 Effect of pulse phase on a 90° excitation pulse 24

Figure 2.9 Relationship between k-space and image domain characteristics 27

Figure 2.10 Gradients (top) and k-space trajectory (bottom) for EPI 28

Figure 2.11 Conjugate (Hermitian) symmetry of k-space 29

Figure 2.12 Magnitude, phase, real, and imaginary images 31

Figure 2.13 Whole brain slice reconstruction (centre) from a 32-channel coil 33

Figure 2.14 Bloch simulation of a WET saturation scheme 36

Figure 2.15 Flow-compensated trapezoidal slice select gradient 40

Figure 2.16 Example of slice positioning for a PCASL experiment 43

Figure 2.17 TRU-PC measuring the venous oxygenation in different parts of the sagittal sinus 54

Figure 3.1 Control, tag, and difference images for TRUST at varying eTE 59

Figure 3.2 TRUST pulse sequence diagram 59

Figure 3.3 Bloch simulation of T2 encoding module 61

Figure 3.4 Bloch simulations for for two effective echo times eTE = 40 & 200 ms 62

Figure 3.5 Geometric placement of each component of SL-TRUST 63

Figure 3.6 SL-TRUST pulse sequence 63

Figure 3.7 Inversion time for TRUST and SL-TRUST 65

Figure 3.8 T2 values for SL-TRUST for a range of repetition times TR = 4, 6, 8 s at TI = 1200 ms 69

Figure 3.9 Poor saturation profile of standard product saturation pulses 70

Figure 3.10 Comparison of two saturation schemes 71

Figure 3.11 Cosine modulating a sinc pulse 74

Figure 3.12 Illustration of the target MCA territory and the placement of two WET saturation bands 75

Figure 3.13 Signal instability (blue and red) for regional SL-TRUST 76

Figure 3.14 TRUST vs SL-TRUST percentage error (N = 12) 79

Figure 3.16 Scaling of error bars in TRUST vs SL-TRUST 80

Figure 3.17 Simulation (LEFT) and experimental data (RIGHT) for a range of $T1_{opt}$ values. 82

Figure 3.18 Percentage error on SL-TRUST T2 without and with BGS (N = 4) 83

Figure 3.19 Comparison of sum of squares and adaptive combine methods 87

Figure 3.20 Example T2-decay curves using the final developed protocol for SL-TRUST 89

Figure 4.1 Relationship between venous blood oxygenation and venous blood T2 95

Figure 4.2 Example images and resulting inversion recovery curve for T1 measurement 98

Figure 4.3 Average and standard deviation of T2 values across all scan sessions 104

Figure 4.4 Bland-Altman correlation plots for T2-measurements 105

Figure 4.5 Fluctuation in T2 in a single subject over three scan sessions on separate days 110

Figure 4.6 T2-decay curves for regional SL-TRUST in two stroke patients 115

Figure 5.1 Structure of a phorus phantom using remote spatial encoding 122

Figure 5.2 Illustration of the principle of remote reconstruction for SL-TRUST 123

Figure 5.3 Example of phase encoding bands on a phantom within k-space 127

Figure 5.4 Phantom reconstructions at varying resolutions 129

Figure 5.5 Pulse sequence diagram for SL-TRUST with phase encode gradients 130

Figure 5.6 Magnitude and phase image at zero phase encoding of a cos encoded phantom 133

Figure 5.7 Reconstruction of k-space 134

Figure 5.8 Example of k-space matrix transformed into image space via a 2D IFT 135

Figure 5.9 Example of smearing in zero filling partial Fourier reconstruction 136

Figure 5.10 Iterative pipeline for POCS 138

Figure 5.11 Comparison of POCS and Zero Filling reconstruction 139

Figure 5.12 Whole brain reconstruction demonstrating the removed signal 141

Figure 5.13 Comparison of remote reconstruction following WET saturation **141**

Figure 5.14 Inversion time dependence for phase encoding remote reconstruction **143**

Figure 5.15 Two T2 remote reconstructed maps from healthy controls **145**

Figure 5.16 Maps at varying eTE for a single subject and the T2 decay curves **146**

Figure 6.1 T2 decay curves for SL-TRUST with and without pairwise subtraction **156**

Figure 6.2 Selecctive excitation RF pulses to give a 3D spatially selective inversion **158**

List of Tables

Table 2.1 Summary of some literature findings of elevated OEF in disease..... 10

Table 2.2 Comparison of CP, CPMG, and MLEV-4 phase cycling 26

Table 3.1 T2 dependence on TR for 4 subjects..... 68

Table 4.1 Summary of studies determining the linear relationship for T2 and hct..... 96

Table 4.2 Coefficients of Variation for TRUST Liu et al. 2013 99

Table 4.3 Coefficients of Variation for TRUST and SL-TRUST 104

Table 4.4 OEF values calculated using uniform haematocrit values.....107

Table 4.5 Comparison of Inter-subject CoV for uniform and subject specific haematocrit.....109

Table 4.6 Subject-specific T1 and corresponding haematocrit and OEF.....111

Table 5.1 Example measurement acquisition order for a 3x3 map with two T2-encode points.....131

Table 6.1 T2 values (mean ± std) for SL-TRUST with and without pairwise subtraction.....156

List of Abbreviations

ASL	Arterial Spin Labelling
BGS	Background Suppression
BOLD	Blood Oxygen Level Dependent (imaging)
CBF	Cerebral Blood Flow
$CMRO_2$	Cerebral Metabolic Rate of Oxygen
CPMG	Carr-Purcell-Meiboom-Gill
CSF	Cerebral Spinal Fluid
DWI	Diffusion Weighted Imaging
eTE	Effective Echo Time
FFT	(Discrete) Fast Fourier Transform
GM	Grey Matter
HCT	Haematocrit
MCA	Middle Cerebral Artery
MLEV	Malcom-Levitt (preparation scheme)
NIRS	Near-infrared-spectroscopy
OEF	Oxygen Extraction Fraction
PET	Positron emission tomography
QUIXOTIC	Quantitative Imaging of eXtraction of Oxygen and Tissue Consumption
RF	Radio-Frequency (pulse)
RHS	Right Hand Side
ROI	Region of Interest
SL-TRUST	Selective Localised T2-Relaxation-Under-Spin-Tagging

SNR	Signal to noise ratio
T1	Longitudinal relaxation time
T2	Transverse relaxation time
TE	Echo time (readout)
TI	Inversion time
TR	Repetition time
TRUST	T2-Relaxation-Under-Spin-Tagging
TRU-PC	T2-Relaxation-Under-Phase-Contrast
VSEAN	Venous Oxygenation Mapping using Velocity-Selective Excitation and Arterial Nulling
WET	Water suppression Enhanced through T1 effects
WM	White Matter
Y_v	Venous Oxygenation

Chapter 1 Motivation and thesis outline

Starting with the discovery of x-rays in 1895, imaging techniques and the ability to image the internal structures and functions of the body have accelerated our understanding of the inner workings of the human body. On the forefront of current day human imaging is magnetic resonance imaging (MRI). MRI is distinguished from many other forms of imaging methods due to the variety of both structural and functional information it provides, without the use of potentially harmful radiation, and is therefore increasingly used throughout the world for clinical diagnosis. There is now a particular drive to obtain more quantitative information using MRI, to better understand the underlying physiological parameters in disease and how these change over time.

One such physiological parameter is cerebral oxygenation. The rate of oxygen metabolism in the brain can be a key indicator of tissue health and has been shown to become elevated in brain tissue distress and death, for example due to tumours, stroke, tissue hypoxia, and even during the normal aging process.

The current gold standard for obtaining quantitative cerebral oxygenation maps remains positron emission tomography (PET), which is limited in its availability and applicability due to the use of radioactive tracers with short half-lives (1). There is therefore a desire to develop new, more accessible, and more flexible methods for

measuring regional cerebral oxygenation levels. Thanks to the different magnetic properties of oxygenated and deoxygenated blood, oxygen can be used as an endogenous contrast agent in MRI, removing the requirement for external contrast agents. Unlike PET, MRI is suitable for longitudinal assessment (repeated scans over a period of time), and basic research in healthy controls and patients.

Whilst whole brain, or "global", measurements of cerebral oxygenation have been achieved readily using MRI, regional quantification is a key challenge that is yet to be addressed fully.

The aim of this thesis is to develop a new MR method for quantitatively measuring oxygenation of cerebral tissue, specifically one which can compare oxygenation across different brain regions or acquire oxygenation "maps" of the brain. Together with other MR measures such as cerebral blood flow, a successful method would be able to provide an insight into the underlying physiology of regionally specific cerebrovascular conditions and potentially aid diagnosis and treatment.

1.1 Thesis Outline

The body of this thesis consists of one background chapter and three research chapters. The first two research chapters are concerned with the development and testing of a novel sequence SL-TRUST for measuring oxygen extraction fraction (OEF) in pre-specified regions of the brain. The third chapter is an extension of the SL-TRUST method which aims to produce T2 maps using a remote spatial encoding method. The structure of this thesis is as follows:

Chapter 2 introduces the role of oxygen in brain physiology and maintaining cellular function. An overview of existing techniques for quantification of blood oxygenation, both in MR and other imaging modalities, is provided. The building blocks and fundamentals of MR sequences specific to imaging blood are introduced.

Chapter 3 documents the different development stages of a novel MR sequence, Selective Localized T2-Relaxation-Under-Spin-Tagging (SL-TRUST) and the steps required to obtain robust regional measures of the transverse relaxation rate T2 of venous blood in the brain.

Chapter 4 presents a reproducibility study of SL-TRUST conducted in healthy controls. A method for measuring venous blood T1 is also outlined in this chapter, with the aim of estimating subject specific haematocrit without an invasive blood sample and therefore measure absolute OEF, as well as relative changes. The chapter concludes with the application of SL-TRUST in a stroke population.

Chapter 5 presents an extension to the SL-TRUST method and proof of concept and initial optimisation steps of a method which enables reconstruction of low resolution blood T2 maps of the brain.

Chapter 6 presents some on-going work, and discusses possible extensions and future directions. These include application at 7 Tesla, and use of compressed sensing to speed up the T2 mapping.

Chapter 2 Introduction

This chapter sets the scene for the thesis by describing the role of oxygen in maintaining cellular brain function and introducing some key imaging techniques that are currently used to measure oxygenation in the brain: Positron Emission Tomography (PET), Near Infra-Red Spectroscopy (NIRS), and Magnetic Resonance Imaging (MRI).

The key building blocks of MRI sequences are explained, with a particular focus on specific techniques which provide some background to the pulse sequences developed in this work. Finally, there is some discussion of existing techniques for measuring cerebral blood flow and oxygenation using MRI.

This chapter is not intended to be an introduction to MR physics. It is assumed that the reader already has an understanding of key concepts such as spin, precession, relaxation, and the Bloch equations, more complete descriptions of which can be found in many standard text books (2-4).

2.1 Blood and brain physiology

The adult brain is only around 2% of the total body weight, yet is one of the most energy hungry organs in the human body. The primary source of fuel for this energy in the brain is glucose, which is used to produce adenosine tri-phosphate (ATP) via oxidative

phosphorylation. This process occurs within the mitochondria of the cell (hence why the mitochondria is commonly termed the powerhouse of the cell) and requires a number of other components such as fatty acids, and of course, oxygen. ATP may be generated via two processes, anaerobic or aerobic glycolysis:

$$1 \text{ glucose} \rightarrow 2 \text{ ATP} \qquad \text{(anaerobic)}$$

$$1 \text{ glucose} + 6\ O_2 \rightarrow 36 \text{ ATP} \qquad \text{(aerobic)}$$

Whilst aerobic glycolysis is a more efficient method of producing ATP, it is slower than anaerobic glycolysis and requires a supply of oxygen molecules in order to provide the additional ATP molecules. The oxygen molecules facilitate an electron transport chain which creates an electrochemical gradient across the mitochondrial membrane. H^+ ions flow along this gradient, in the process passing through an enzyme which harnesses this flow to add a phosphate to ADP (adenosine diphosphate), thus forming ATP. Oxygen sits at the end of this chain reaction and is the final electron acceptor, without it the flow of electrons is halted and ATP production is stopped. Thus, the consumption of both glucose and oxygen in the brain are an indicator of ATP production and hence tissue metabolism. As the brain does not contain any fuel stores, it relies on a constant supply of glucose and oxygen from the blood to maintain healthy brain function.

2.1.1. Oxygen transportation and haemoglobin

Blood is an "aqueous fluid" meaning it is in essence water. Approximately 55% of human blood consists of plasma and platelets (water, salt, enzymes, and proteins). The two other

main components are white blood cells (leukocytes) (<5%), and red blood cells (erythrocytes) (40-45%). Despite their important role in maintaining the immune system and coagulation, due to their relatively small contribution to the total blood volume and limited role in oxygen transportation, white blood cells are not considered in any further detail here.

Red blood cells, on the other hand, form a vital role in oxygen transportation as they contain the protein haemoglobin. Each molecule of haemoglobin has an iron atom that can bind four molecules of oxygen. Oxygen diffuses into the plasma from the lungs, before binding to the haemoglobin, to form oxyhaemoglobin. A small fraction of the oxygen remains dissolved in the plasma.

Oxygen and carbon dioxide concentrations in the blood are expressed as partial pressures (kPa or mmHg), and the amount of oxygen held by the haemoglobin is referred to as the oxygen saturation and is often expressed as a percentage. Figure 2.1 shows an oxygen dissociation curve which illustrates how the *oxygen saturation* and partial pressure of oxygen in the blood relate to one another and also how this relationship is shifted left or right, by blood pH, temperature, and dissolved carbon dioxide.

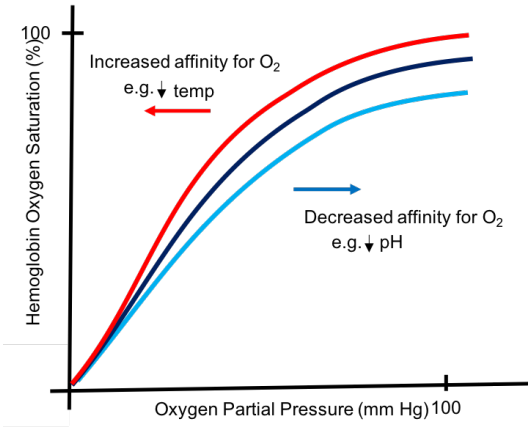


Figure 2.1 Oxygen dissociation curve

When the partial pressure of oxygen is high (for example in the lungs), the oxygen binds readily to the haemoglobin. However, when the haemoglobin molecule finds itself in a region of lower partial pressure, for example in brain tissue, the haemoglobin can no longer maintain fully bound oxygen in this lower pressure state, and therefore begins to release the oxygen into the tissue. As the concentration of oxygen decreases it is replaced with carbon dioxide (CO_2) which is a waste product of aerobic glycolysis, which binds to the haemoglobin, and is removed in outflowing venous blood.

Maintaining a constant and healthy supply of blood and therefore oxygen in the brain is critical as neuronal cells have a higher rate of metabolism than other kinds of cells, and the brain has minimal energy reserves compared to other organs in the body (5). The terms cerebral blood flow (CBF) and perfusion are often used interchangeably, with both quoted as units of ml blood/100 g brain tissue/minute, and refer to the delivery of blood to the capillaries in order to deliver oxygen and essential nutrients to the surrounding tissue.

Even short interruptions to the blood supply can have long lasting impacts on neuronal cellular function. For this reason the brain has a variety of auto regulatory mechanisms designed to maintain oxygen partial pressure at an optimal point. Vessels dilate and reduce resistance (vasodilation) to allow more blood and therefore more oxygen through if the oxygen content or carrying capacity of the blood is poor. In doing so the cerebral blood volume (CBV) increases in an attempt to maintain constant oxygen delivery. The ability of the brain to increase the perfusion is also called the cerebrovascular reserve (CVR) (6). Understanding the interplay between these mechanisms and how they work to maintain physiologically stable conditions under stress is important in establishing the

underlying causes or differences in disease. Another biomarker which is used as an indicator of underlying tissue health and oxygen metabolism is the oxygen extraction fraction.

2.1.2. Oxygen extraction fraction (OEF)

The oxygen extraction fraction (OEF) is the relative difference in oxygen concentration between arterial (Y_a) and venous (Y_v) blood and can be expressed either as a fraction or as a percentage, $\mathrm{OEF} = \frac{Y_a - Y_v}{Y_a}\ x\ 100$. The OEF of healthy cerebral tissue is around 40%, however there is a range in reported values of OEF even in healthy populations (7-9). Changes in OEF have been reported using PET and MRI studies in a variety of conditions and disease stages, such as moyamoya, sickle cell disease, and even as a prognostic biomarker for stroke (10-14). In all of these cases OEF becomes elevated as a result of tissue distress and neuronal cell death. A summary of some example literature OEF values measured using PET and MRI in disease are shown in Table 2.1. Note how, in PET studies the OEF values are in the region of 35-50%, the expected physiological range, whereas for MRI studies the absolute OEF values can be more variable. However, both methods demonstrate similar relative differences.

Table 2.1 Summary of some literature findings of elevated OEF in disease (11,12,14-16). This is not a comprehensive literature review. † pre vs post-operative changes within subjects. *healthy vs affected hemisphere in same subject

Study	**Disease**	**Modality**	**$OEF_{healthy}$**	**$OEF_{disease}$**
Watchmaker, 2018	Moyamoya	MRI	29-38%	39-45%
Kaku, 2012	Moyamoya†	PET	40%	61%
Derdeyn, 2002	Stroke	PET	~41%	~53%
Fan, 2019	Stroke*	MRI	25%	29%
Aanerud, 2012	Aging	PET	~40%	~42%

OEF is dependent on a variety of factors at play in the brain, for example, the volume percentage of red blood cells (haematocrit), end tidal CO_2 (the amount of CO_2 at the end of exhalation), and the ability of the brain to adapt to maintain stable CBF (the cerebrovascular reserve as described above) (11,17). For that reason the exact underlying cause of changes in OEF can be difficult to determine and disentangle from other effects (18). For example, an equal increase in OEF could arise from the following two cases: 1. Reduced oxygen carrying capacity and normal CBF, or 2. Normal oxygen carrying capacity but reduced CBF. Despite this, OEF can be considered a superior biomarker of tissue distress than say the metabolic rate of oxygen consumption ($CMRO_2$) or perfusion alone, which can remain stable well into the advanced stages of disease (10,19).

For the case of reduced CBF consider the oxygen disassociation curve for blood as it transits through the vasculature shown in Figure 2.2. As the blood moves from the arterial to the venous side oxygen is extracted from the red blood cells. At first the partial pressure (pO_2) changes slowly as the haemoglobin within the red blood cells releases an oxygen molecule every time one is lost to the tissue to maintain the partial pressure, however, approaching the venous end of the tree more oxygen is being extracted than is being released and the overall oxygen partial pressure decreases. At the end point of the venous tree the oxygen saturation is approximately 65%, giving an OEF of 35%, this corresponds to the partial pressure required to maintain the oxygen delivery to the cells furthest from the capillaries. For reduced CBF, as a result of stroke or other disease, the venous pO_2 is reduced beyond the viability point, leading to cell death of these distal cells, as illustrated in Figure 2.3, and an increase in OEF according to the oxygen dissociation curve in Figure 2.2.

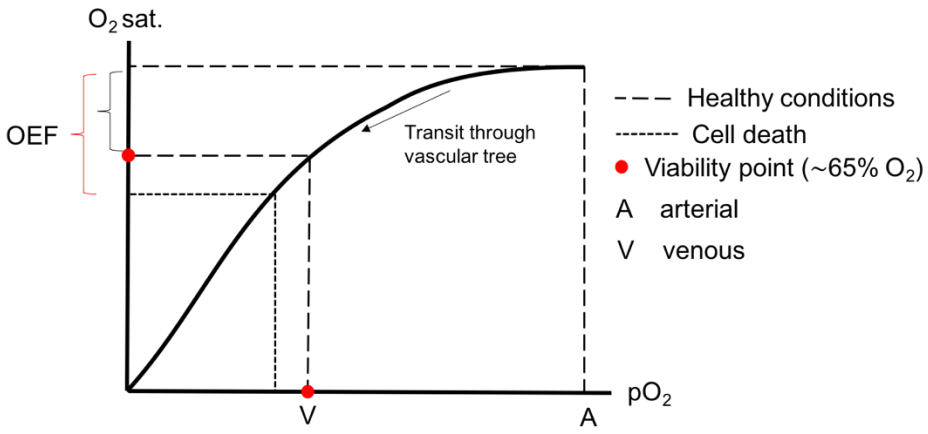


Figure 2.2 Increase in OEF following stroke or tissue disease as the oxygen saturation levels decrease due to reduced CBF

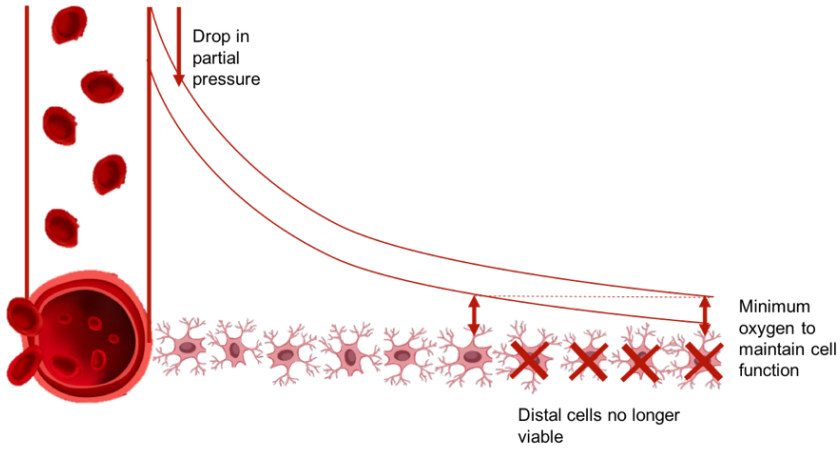


Figure 2.3 Cell death of cells distal to the capillaries as a result of a drop in venous partial pressure. The partial pressure has fallen below the viability point for these cells.

2.1.3. Brain vascular system

Oxygen is transported around the body in the blood via an intricate network of arteries and other blood vessels. Whilst any organ will suffer in cases of constricted blood supply, the brain is particularly vulnerable. As a result, along with the autoregulation methods described above, the vascular system is designed to include a number of safeguards to maintain a continuous supply of blood and nutrients. The two major sources of vascular supply are the internal carotid arteries, and the vertebrobasilar arteries. These are connected via the Circle of Willis at the base of the brain. This protects the blood supply to many regions of the brain even if one of these major arteries becomes occluded (5). From the Circle of Willis other arteries such as the anterior cerebral artery (ACA), the middle cerebral artery (MCA), and the posterior cerebral artery (PCA) branch off. In the

case of a stroke in any of these arteries, the artery affected can generally be diagnosed based on the collection of symptoms. The ACA feeds the frontal lobe of the brain which is associated with logical thinking, personality traits, and contains some of the motor cortex responsible for voluntary movement, symptoms may therefore include difficulty walking. The PCA feeds the temporal and occipital lobes, strokes in this artery can have a wide range of symptoms but are often visual in nature. Finally, the largest branch and the most commonly affected by stroke is the MCA, this feeds the speech and motor cortices which leads to the symptoms typically associated with stroke such as slurred speech and weakness in the limbs (20).

Once the blood has made its way from the arteries and through the deeper structures of the brain it arrives in the venous drainage system of the brain. This system can be divided into two: superficial and deep. The superficial veins are not actually veins in terms of their structure, instead they are dura mater, a thick membrane of connective tissue. These veins are referred to as sinuses and run along the surface of the cerebrum, surrounded by cerebrospinal fluid (CSF). The

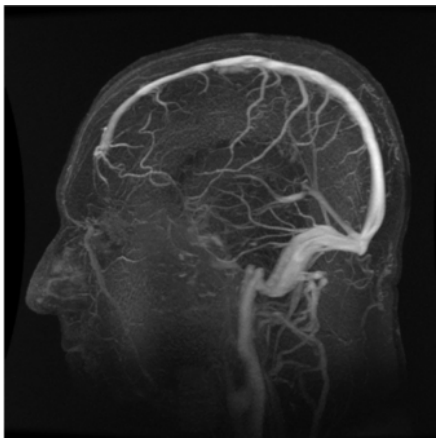


Figure 2.4 A gadolinium enhanced MR Venogram (MRV) showing the superior sagittal sinus draining blood from the cerebral vasculature into the jugular veins. Image obtained under CC license[1]

[1] https://www.flickr.com/photos/reighleblanc/4018615874

largest of these sinuses is the superior sagittal sinus which runs sagittal along the brain, see Figure 2.4.

The deep veins merge with the inferior sagittal sinus to form the straight sinus, which then joins the larger superficial sinuses at the confluence of sinuses. These then drain the blood into the internal jugular veins which are parallel to the arteries in the neck.

The two key pathways discussed and utilized in this work are the tissue territories fed by the MCA, and the venous blood in the superior sagittal sinus.

Compared to the arterial vasculature there is more variation in the venous system between individuals, and less literature investigating which regions of the brain drain to which veins or sinuses (21). Similarly, it has not been well characterised what proportion of the blood ends up being drained through the superior sagittal sinus, however it is often reported as being the most common site of venous thrombosis (a blood clot in a vein) in the brain (22,23).

2.2 Measuring blood oxygen saturation

With OEF proven to be an important biomarker and indicator of disease in neuronal tissue, it is important to be able to accurately and quantitatively measure the oxygen content of the blood. Some of the properties of haemoglobin described previously enable quantification of blood saturation levels using a variety of methods such as optics and magnetic resonance imaging (MRI). In the following section three key methods for determining blood and/or tissue oxygenation are outlined: Positron-emission tomography, near-infrared-spectroscopy, and finally MRI.

2.2.1 Positron-emission tomography (PET)

Positron-emission tomography (PET) is a functional imaging technique for observing metabolic processes in the body. Positron-emitting isotopes are produced using a cyclotron and then introduced into the body on a biological molecule called a radioactive tracer. As the isotopes undergo radioactive decay they emit a positron which annihilates when it comes into contact with an electron and emits two gamma photons which are detected by an array of sensors surrounding the patient. PET is not a structural imaging technique and is therefore used in conjunction with a CT X-ray scan which is often combined in the same machine such that the two images can be registered together accurately.

The most widely used PET tracer is fluorodeoxyglucose (FDG), an analogue of glucose, which incorporates a fluorine-18 isotope. This isotope accumulates in glucose-hungry areas of the body and as such is most often used in imaging cancer.

Another radioactive isotope used in PET to investigate cerebral metabolism is oxygen-15. The half-life of oxygen-15 is only 123 s (versus approximately 2 hours for fluorine-18) and therefore an on-site medical cyclotron is a requirement for these scans. This severely limits the availability and applicability of the method. In addition to this the process of achieving an OEF map of the brain using oxygen-15 has three separate stages: oxygen-15 gas inhalation, oxygen-15 labelled water injection, and inhalation of oxygen-15 carbon monoxide (24). These are conducted in three separate PET scans. This results in a significant total radiation dose, limiting the number of repeat scans. This further restricts research applications, especially those involving longitudinal changes in oxygen

metabolism. Yet, PET is still considered to be the gold-standard for regional mapping of metabolic activity in the brain.

2.2.2 Near infrared spectroscopy (NIRS)

Near Infrared Spectroscopy (NIRS) is a non-invasive optical imaging technique that utilizes the different optical properties of oxygenated and deoxygenated blood. The absorption peaks of both oxy- and deoxy-haemoglobin lie close to each other in the 400-600 nm range. However between the 600-2000 nm range the two absorption spectra diverge, see **Error! Reference source not found.**. Therefore optical sources and detector probes use low level light in the wavelength range 780 – 2500 nm to determine the relative changes in the volume of oxygenated versus deoxygenated blood.

Compared to other imaging modalities NIRS provides a cheap method of measuring relative changes in tissue oxygenation over time. The devices are also small and portable, increasing the reach of the technique to populations and patient groups that may not otherwise have access to brain imaging techniques. The portable aspect of NIRS means it

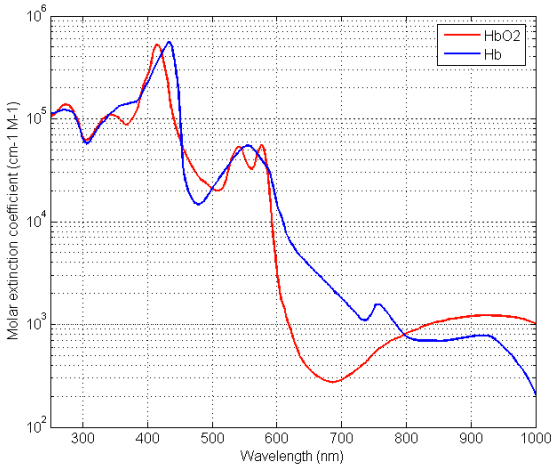


Figure 2.5 Absorption spectra for oxygenated and deoxygenated haemoglobin. Image reproduced with permissions from the author.[2]

[2] https://omlc.org/spectra/hemoglobin/

can also be used for continuous monitoring or measurements during unconstrained motion tasks.

The most successful application of NIRS has been in neonatal cerebral imaging, where the combination of smaller head sizes and thinner skull bone that is not yet fully formed means light can penetrate through to the brain tissue and vasculature. The BRIGHT project (BRain Imaging for Global HealTh) has performed some functional NIRS (fNIRS) studies, examining brain function and hemodynamic responses to visual stimuli in infants in Africa (25).

The key disadvantages of NIRS are the lack of quantitative information regarding blood oxygenation levels, the limited coverage of the sensor, and limited penetration depth of the NIRS signals due to the skull. This final point severely limits successful applications in adults. For this reason, NIRS is not widely considered to be at the forefront of mapping cerebral oxygen techniques. That is not to say that it is not a powerful tool for investigating cerebral oxygenation in certain patients and populations, as described above, however it is agreed that it is a tool with limitations (26).

2.2.3 Magnetic resonance imaging (MRI)

MRI is perhaps the most powerful imaging tool, with scope to measure a wide range of physiological parameters and no limit to the depth or orientation at which one can image the body. MRI does not involve any ionising radiation and is therefore not hazardous for longitudinal studies. Despite being a relatively new clinical method its popularity is growing rapidly worldwide.

Blood is an endogenous contrast agent in MRI thanks to the different magnetic properties of haemoglobin, depending on whether or not it is bound with oxygen. As described in 2.1.1 the iron site in the haemoglobin has 4 oxygen binding sites. In fully oxygenated blood all iron sites are bound to oxygen then the spin S = 0, making it *diamagnetic*. Deoxygenated blood has four unpaired electrons, thus giving it a spin S > 0, and is described as being *paramagnetic*. The magnetic susceptibility χ (the tendency of a molecule or material to interact and distort a magnetic field) is proportional to N(N+2) where N is the number of unpaired electrons. It is this difference in susceptibility that gives MRI its sensitivity to changes in oxygenation. The MR property T2, the transverse relaxation time, is altered depending on the number of bound oxygen molecules, and is proportional to the square of the magnetic susceptibility (χ^2) (27). MRI methods to quantify oxygenation content of the blood therefore aim to measure either the susceptibility or T2 of blood or blood vessels in the brain. Some key methods are outlined in more detail in 2.7.

2.3 MRI sequence building blocks

MRI involves manipulating the resonance frequency of nuclei which interact with a large external magnetic field. In theory it is possible to measure signal from any nucleus which has a magnetic moment which is not equal to zero. However, the vast majority of MR methods focus solely on the manipulation and imaging of hydrogen, as it is the most abundant molecule in the human body.

Unless otherwise stated, the static magnetic field B_0 throughout this thesis is that of a 3 Tesla MR scanner, which by convention, points in the positive *z*-direction. When placed in this main magnetic field B_0, the bulk of the hydrogen spins will align either parallel or anti-parallel with the field. Of these two options the lower energy state is to align parallel to the field and this bias is sufficient to result in a net magnetisation vector **M**, in the same direction as the external field. The spins precess about the B_0 axis at the Larmor frequency ω_0 which is proportional to B_0 and the gyromagnetic ratio of the nucleus (42.576 MHz/T for hydrogen):

$$\omega_0 = \gamma B_0$$

Equation 2.1

Applying a gradient across a sample results in resonance frequencies which are spatially dependent. Equation 2.1 can now expanded to include terms for the local field ΔB_0 (due to susceptibility differences) and the gradient $G(r)$ varying spatially across the sample:

$$\omega_L(r) = \gamma B_0 + \gamma \Delta B_0 + \gamma \cdot G(r)$$

Equation 2.2

The use of gradients to achieve spatial localisation was a key step in translating nuclear magnetic resonance (NMR) into a clinical imaging technique. Spins can now be targeted based on their spatial location by tuning a radio frequency (RF) pulse to a specific frequency bandwidth centred on ω_L. The RF-pulse acts to perturb the bulk magnetisation **M** of the targeted spins out of alignment with B_0. The longer the duration of this RF-pulse (t), the larger the angle (α) the magnetisation is rotated away from the longitudinal axis:

$$\alpha = \int \gamma B_1(t)\, t\ dt$$

Equation 2.3

RF pulses can be any arbitrary angle, but the most commonly used in MR sequences are 90° and 180° pulses, referred to as excitation and inversion or refocusing pulses respectively.

Excitation of a slice with width Δz, is achieved using an RF-pulse with a range of frequencies $\Delta\omega$, centered on the frequency ω_L of the spins corresponding to the spatial position z_0. The simplest frequency profile that translates into a uniform slice profile in the spatial domain is a sinc pulse. The sinc pulse is an amplitude-modulated sine wave with base frequency ω_L:

$$B_1(t) = sinc(\Delta\omega\pi t)\sin(2\pi\omega_L t)$$

Equation 2.4

The design, shape, and manipulation of the RF-pulse is important for achieving the best results in an MR experiment as it becomes increasingly difficult to achieve uniform slice profiles at higher field strengths.

There are also a number of practical considerations when it comes to designing the gradients used for spatial localisation as the amplitude and duration of the gradients are constrained by a number of properties of the hardware used to produce them. A perfect step gradient with infinite slope, is impossible to achieve. Instead the gradient is “ramped up” and “ramped down”, the speed of which is limited to the slew rate of the scanner

hardware. As such the gradients typically form a trapezoidal shape. A consequence of fast ramp times is gradient shape imperfections due to induced eddy currents. Eddy currents are generated to oppose the flux of the rapidly changing magnetic field, and scale in proportion with the speed at which the gradients change. These can be particularly problematic in fast imaging sequences where the gradients change rapidly and require eddy current compensation methods either pre- or post- acquisition to minimise image distortion.

2.3.1 Adiabatic pulses

Adiabatic pulses are a special class of RF pulses which help achieve uniform inversion of the magnetisation in the presence of B_1 inhomogeneities (28). The relationship between the flip angle and the applied field B_1 given in Equation 2.3 is not valid for these pulses. Instead, to achieve an adiabatic pulse the amplitude and frequency of the B_1 field is varied to produce an effective field B_{eff}. The direction and amplitude of B_{eff} varies over time and is a product of the vector sum of the amplitude and frequency of the pulse.

The adiabatic pulses used in this work are hyperbolic secant inversion pulses. The amplitude and frequency profiles of this pulse are shown in Figure 2.6 and the resulting B_{eff} and the effect on the magnetisation vector **M** over the course of the duration of the pulse is shown in Figure 2.7. At t = 0 the amplitude of the pulse is zero but the frequency is completely off resonance, therefore the effective field B_{eff} is aligned with **M**. As the pulse traverses through both an amplitude and a frequency sweep the effective field B_{eff} rotates and drags **M** with it until eventually it is completely inverted.

The beauty of adiabatic pulses is that the amplitude of the pulse does not have to be exact (as shown by the dashed lines in Figure 2.6) in order to achieve the exact same flip angle. Therefore, even in the presence of B_1 inhomogeneities, resulting in deviations in the pulse amplitude, a uniform flip angle will still be achieved across the sample.

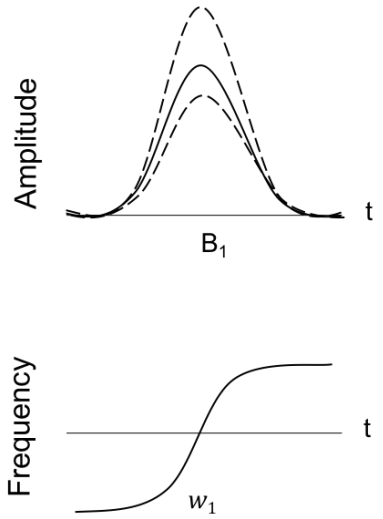


Figure 2.6 Amplitude and frequency sweep of an adiabatic hyperbolic secant inversion pulse

This is only valid, however, if the pulse satisifies the adiabatic condition. This states that the magnetisation **M** will only rotate with B_{eff} if the amplitude of the pulse is large enough, and the frequency sweep applied slowly enough. However, if the pulse duration is too long then magnetisation is lost through T2 decay.

Adiabatic inversion pulses are utilised throughout this work where accurate inversion pulses are critical.

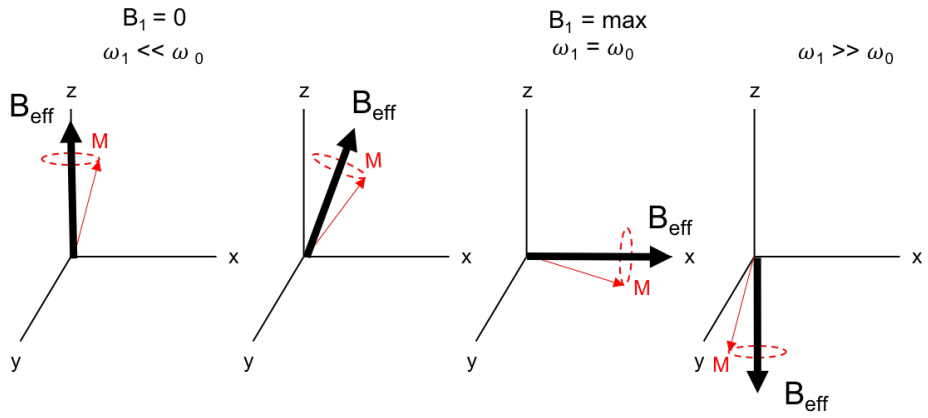


Figure 2.7 Path of vector M as an amplitude and frequency sweep are applied to produce B_{eff} for an adiabatic hyperbolic secant inversion pulse.

2.3.2 Phase cycling

Returning to conventional pulses, the flip angle of the pulse determines the rotation from the *z*- axis. However the orientation of the resulting magnetisation in the rotating reference frame is dependent on the phase angle of the pulse. An example of different types of phase that can be applied to an excitation pulse are shown in Figure 2.8. Phase cycling is used to correct or compensate for hardware or pulse imperfections.

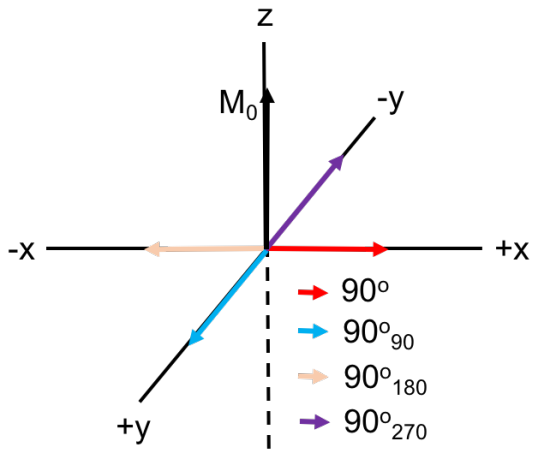


Figure 2.8 Effect of pulse phase on a 90° excitation pulse

An example of hardware induced artefacts would be a baseline offset in the signal receiver which creates an additional uniform signal intensity across at each point in k-space. A uniform signal, when Fourier transformed, becomes a single peak, and as a result this effect appears as a bright spot at the centre of the image called the DC artefact. Phase cycling can be used to remove this artefact by changing the phase of the RF-pulses along opposite directions as phase-encoding is performed. Thus the polarity of adjacent points in k-space is modulated with alternating positive and negative signs. This is equivalent to applying a linear phase modulation which results in a spatial shift in image space. However, the baseline offset is not affected by the shift and remains at the centre of the image. When the image is restored to its original position the DC artefact is now at the edge of the image.

Phase cycling is also used to correct for imperfect RF-pulses. Consider a simple Hahn spin echo sequence where a 180° pulse removes the dephasing that occurs in the transverse plane through reversible mechanisms and thus enables measures of T2 instead

of T2*. However the sequence is prone to diffusion errors. Any spins undergoing diffusion occurring between the initial excitation pulse and the refocusing pulse will not be refocused properly, resulting in a T2 measurement that is a product of both T2 decay and diffusion decay, giving a shorter apparent T2. The longer the echo time, the larger this effect becomes. This effect occurs in the blood due to exchange between intra and extra-cellular water and the naturally occurring mesoscopic field gradients.

Carr and Purcell (29), introduced the concept of using a train of multiple refocusing pulses to correct for this effect, called a CP sequence. However, if the pulses are not perfect 180° (for example due to B1 inhomogeneity) then there is still considerable signal loss in the transverse plane during the CP sequence due to repetition of these pulses, which is cumulative depending on how many pulses are used.

Meiboom and Gill (30) reduced this effect by phase cycling the refocusing pulses with respect to the excitation pulse. That is, if the excitation is applied in the x direction, then the refocusing pulses are applied along y.

The main difference between the two sequences is the direction of the magnetisation after the refocusing pulses. For the case described above, in a CP sequence the magnetisation alternates between the +y and -y directions with each refocusing pulse. In the CPMG sequence the magnetisation always points along the +y direction (31).

A further extension of the CPMG method is an MLEV pattern (Malcom Levitt) whereby pairs of refocusing pulses are cycled, see Table 2.2, to give superior refocusing of signal in the case of pulse imperfections. As this form of phase cycling is for pairs of pulses an

MLEV strategy uses 2^n pulses and are therefore referred to as MLEV-4 or MLEV-16 etc. depending on how many pulses are used (32).

A CPMG sequence, or variants thereof, is often used when trying to measure the T2 of moving or diffusing spins (33). The shorter the inter-echo spacing between consecutive refocusing pulses the better as the spins have less time to travel/diffuse.

Table 2.2 Comparison of CP, CPMG, and MLEV-4 phase cycling

	90	180	180	180	180	90
CP	**-x**	**-x**	**+x**	**-x**	**+x**	**+x**
CPMG	**-x**	**+y**	**-y**	**+y**	**-y**	**+x**
MLEV-4	**-x**	**+y**	**+y**	**-y**	**-y**	**+x**

2.4 Image formation

Image formation is achieved using additional gradients to perform what is generally known as frequency and phase encoding. Mathematically these are the same process as they both result in a phase accumulation within the spins that is dependent on their spatial location in the sample. Together, they impose spatial frequencies within the slice and as the gradients are varied “drive around” and populate a complex k-space matrix. This matrix is transformed into image space via an inverse Fourier transform. The spacing

between consecutive points in k-space determines the field of view (FOV) in image space, and the maximum k-space value k_{max} determines the image resolution, see Figure 2.9. Calculating the discrete inversion Fourier transform (DFT) is very time consuming, therefore a fast inversion Fourier transform is often performed (FFT) (as long as k-space is sampled evenly).

In theory k-space is infinite and continuous but in practice k-space sampling methods are finite and discrete. There are many different ways to sample k-space, each with their own benefits and limitations: single-shot or multi-shot readouts, and Cartesian or non-Cartesian trajectories. Ultimately the aim is to sample as efficiently as possible, maximising information within time-constraints, and reducing artefacts. The readout strategy used in this thesis is an echo- planar readout (EPI), shown in Figure 2.10.

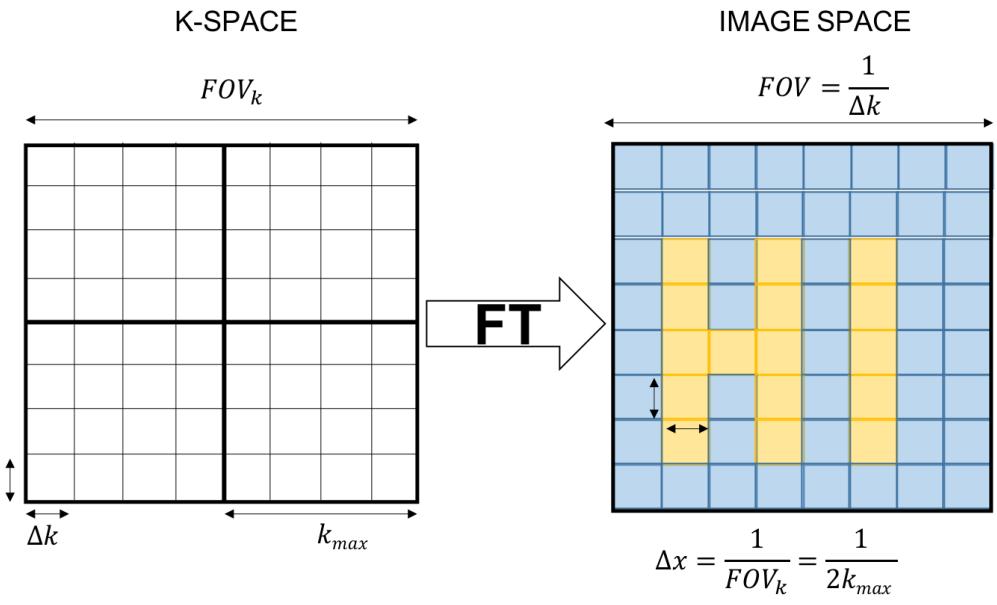


Figure 2.9 Relationship between k-space and image domain characteristics.

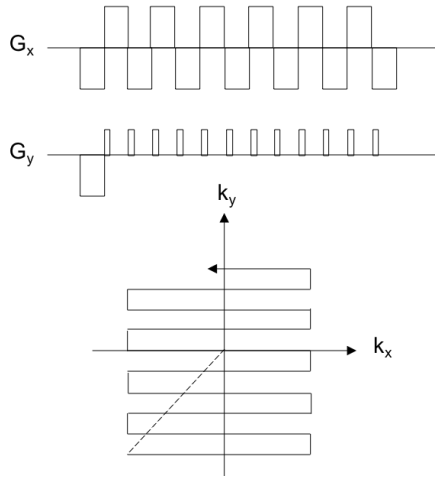


Figure 2.10 Gradients (top) and k-space trajectory (bottom) for EPI. The G_x gradient samples each line of k-space whilst the G_y gradient "blip" moves to the next line.

Due to the information rich nature and mathematical properties of k-space matrix and the Fourier transform it is possible to reduce the sampling of k-space but still reconstruct a complete image in the spatial domain.

2.4.1 Partial Fourier sampling

Partial Fourier imaging is a method in which just over half of k-space is acquired without loss of information in the image space reconstruction. This is possible due to the conjugate symmetry of k-space under certain conditions. If the image is entirely real, pairs of points on opposite sides of k-space are complex conjugates of each other, meaning they have identical amplitude and opposite phase. In theory therefore, half of k-space is redundant and can be generated by taking the complex conjugate of the sampled half. In reality, there is some phase variation across the image due to B_0 inhomogeneity, susceptibility effects and motion, meaning that k-space is not exactly symmetrical (2).

Sampling of slightly more than 50% of k-space is therefore required in order to estimate the phase and improve the prediction of the missing k-space points.

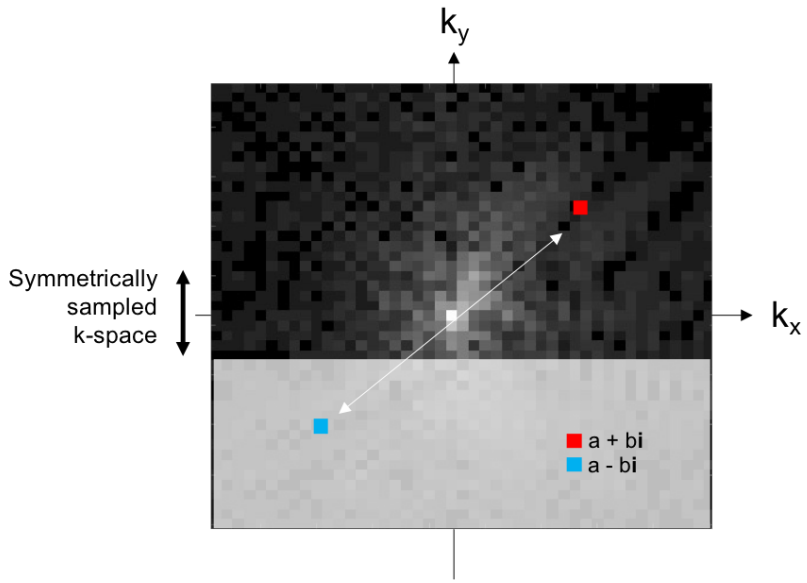


Figure 2.11 Conjugate (Hermitian) symmetry of k-space. The two points (red and blue) are in diagonally opposite locations and have identical real components but imaginary components of the opposite sign.

Partial Fourier can be performed along either the phase or frequency encoding directions. Phase-conjugate symmetry performs top-to-bottom synthesis of k-space data, such as is shown in Figure 2.11, at the cost of image SNR. Read-conjugate symmetry on the other hand is performed left-to-right and does not provide large time-savings as the number of phase encode steps acquired remains the same. Instead it enables the shortening of the readout echo time TE by sampling only part of the echo. This approach is typically used to reduce flow and diffusion artefacts(34).

There are various methods for synthesising the missing k-space points and reconstructing a complete image in the spatial domain. In the simplest case the k-space points are left unfilled (zero-filling). This can result in ringing artefacts on the image due to the sudden and discrete boundary between the sampled data and empty k-space points. A more sophisticated approach is to estimate and fill the missing k-space points using phase constrained reconstruction methods. Here the area of k-space which is symmetrically sampled, provides an estimation of the phase variation across the whole of k-space and is used to perform phase correction across the rest of the image. One such method is called projection onto convex sets (POCS). Both the zero-filling and POCS methods are outlined in more detail in Chapter 5.

2.4.2 Image reconstruction: coil combination methods

The MR signal due to the precession of the magnetisation after an RF pulse is measured using an array of coils around the object, and each coil can be considered as having two channels. The two channels detect magnetic flux signals which are phase shifted by 90° relative to each other and are referred to as the real and the imaginary components. This enables the distinction between positive and negative frequencies (relative to γB_0) of the same amplitude. An MR image can be visualised in four different ways: (1) as a *real* image, (2) as an *imaginary* image, (3) as a *magnitude* image, and (4) as a *phase* image. Examples of each type of image are shown in Figure 2.12. Most clinical applications use the magnitude image, however certain sequences such as flow or susceptibility MRI, use information contained in the phase images.

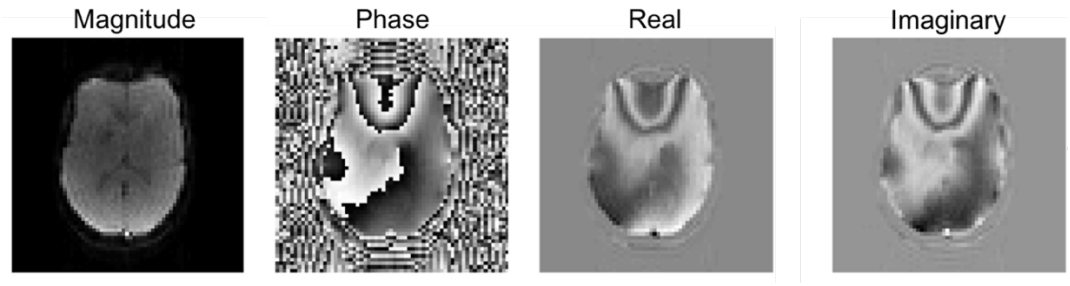


Figure 2.12 Four different ways in which the information from the MR signal may be visualised: magnitude, phase, real, and imaginary components.

How the information from individual coils is combined or reconstructed to form an image can have a significant impact on image quality, SNR, or artefact removal. As illustrated in Figure 2.13, the maximum signal contribution from each coil is naturally in the region of tissue it is closest to with the remaining area in the image made up largely of noise. Unless the images are completely real, simply adding these coil images together to form a complete image would result in areas of cancellation due to differing phase across coils.

The most common method of coil combination is root-sum-of-squares (RSS), where the combined image is the square root of the sum of the squared magnitudes of each coil image:

$$m(r) = \sqrt{\sum_{i=1}^{N_c} |m_i(r)|^2}$$

Equation 2.5

where $m_i(r)$ is the image from a single coil and N_c is the total number of coils. By squaring the signal magnitude, the signal phase is ignored and no adverse cancellation

effects are present. For sequences with inherently high SNR this is sufficient, however it is not suitable for methods with low SNR as it can lead to artefact and noise amplification in the reconstructed image (35). This approach is also not appropriate for methods which rely on the phase information.

Instead, it is more optimal to use the coil sensitivity profiles to weight individual coil contributions. It is possible to measure the coil sensitivities on the scanner, using a body coil as a reference, which has relatively uniform signal reception. However it is problematic and prone to error (35,36). In 2000 Walsh et al. introduced a reconstruction technique, adaptive combine, which estimates optimal weights for each coil based on a statistical matched filter framework (37). For any given voxel, the neighbouring voxels are taken to be multiple statistical samples of the central voxel, and the first eigenvector of the estimated coil-correlation matrix identifies the optimal combination weights. The conjugate of this complex vector forms the weights for each point in space for each coil, preferentially weighting areas of high sensitivity and unwinding the coil-specific phase offsets, and conversely down-weighting contributions from areas of low sensitivity.

An assessment of the SNR improvements provided using adaptive combine reconstruction in comparison to root-sum-of-squares is provided in 3.7.2.

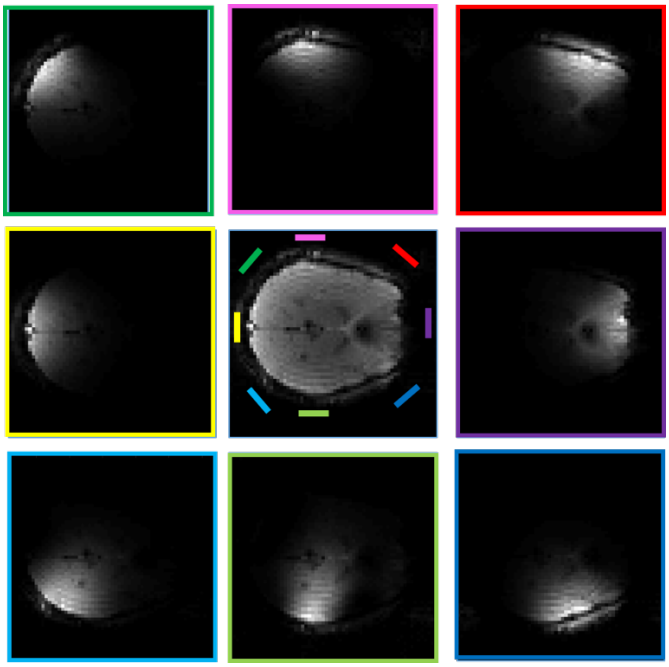


Figure 2.13 Whole brain slice reconstruction (centre) from a 32-channel coil, with example sensitivity patterns from 8 individual coils spaced around the head.

2.5 Isolating blood signal in MRI

Optimizing the k-space acquisition or coil reconstruction methods are two ways in which an MR technique with inherently low SNR can be improved. There are many cases however where additional steps must be taken within the sequence to minimise physiological noise or contaminating signals, before the point of MR signal readout. In this section some of these techniques are outlined, with a focus on those applicable to isolating blood signal.

2.5.1 Background saturation & suppression

Background suppression refers to the attempt to remove signal from a source which may interfere with the MR signal of interest in some way. One example is in MR spectroscopy where the abundance of hydrogen that is usually advantageous in MR imaging results in a large water peak which dominates the spectrum, leaving the spectra of other metabolites of interest virtually undetectable. In imaging, the most common form of background suppression is fat saturation, where the aim is to suppress the signal of fat within the FOV in order to improve the contrast in the image.

For clarity background suppression techniques are separated here into two broad categories: **saturation** methods using 90° RF pulses to excite and then dephase unwanted signal, and **suppression** methods using a combination of 180° inversion RF pulses to null the signal from unwanted tissue at the point of acquisition.

Saturation methods use a spatially or spectrally selective 90° pulse to rotate the magnetisation into the transverse plane and cause maximum phase dispersion of the spins. These are often followed by a strong spoiler gradient to further remove any residual magnetisation in the transverse plane (38). Whilst spatially selective saturation methods aim to dephase the spins within a slice, spectrally specific saturation methods have the added component that the saturation pulse is tuned to a resonant frequency other than water. These pulses target specific chemical components, the most common being fat, and are therefore commonly called “fat-sat” pulses. This approach is also called Chemical Shift Selective saturation (CHESS) (39). Variants of CHESS have been developed over the years for specific purposes such as multi-voxel spectroscopy, or to remove sensitivity

to local T1 and B1 inhomogeneities. These commonly use a combination of multiple pre-saturation pulses, with multiple flip angles, and interpulse delays.

An example of a saturation scheme using multiple flip angles is Water suppression Enhanced through T1 effects (WET) (40). As the name suggests WET was developed for application in MR spectroscopy for water peak spectra suppression. Here, a train of RF pulses is used to minimise the residual magnetization at a time point t following the final pulse in the train. The flip angles of these pulses are varied and optimized for a range of T1 and B1 values, thus making the sequence robust against a range of T1 and B1 inhomogeneities (40). A Bloch simulation of the magnetisation evolution for a range of B1 and T1 values during a WET saturation scheme, starting with spins in an inverted state, is shown in Figure 2.14.

Suppression methods utilize the natural null point of a signal as it undergoes inversion recovery following a 180° RF pulse. If the T1 of the desired tissue to be removed is known the inversion pulse can be timed such that the magnetisation crosses the null point at the time of acquisition. Multiple inversion RF pulses can be combined to target a range of T1 values, and can be both selective and nonselective pulses. This class of methods is called Multiple Inversion Recovery (MIR) suppression. Most MIR methods use two pulses (double inversion recovery, DIR), but three or four pulse methods also exist (41). Multiple inversion recovery (MIR) suppression methods were first introduced for angiographic sequences (42,43) to remove background signal from static brain tissue and thus improve isolation of blood signal. More recently Ye et al. 2000 developed these methods further for applications in noise reduction in 3D perfusion imaging, Attenuating the Static Signal In arterial Spin Tagging (ASSIST) (44).

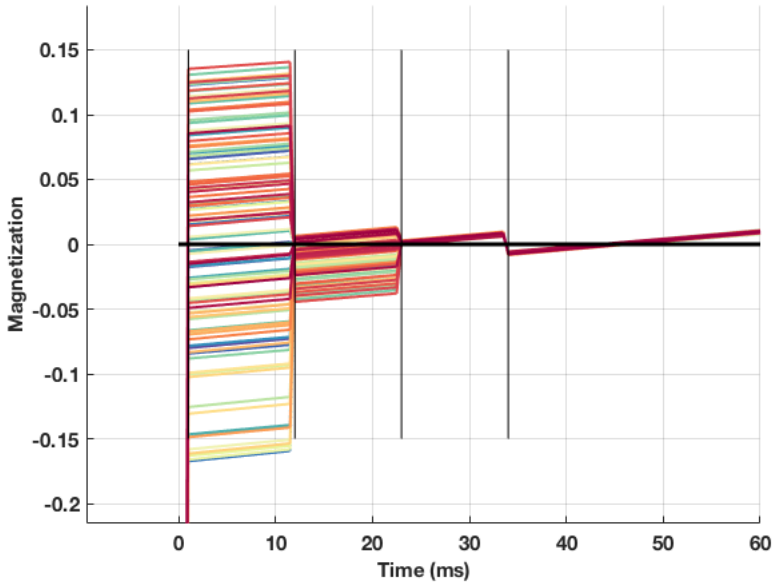


Figure 2.14 Bloch simulation of the longitudinal magnetisation path during a WET saturation scheme with varying flip angles, starting from an inverted state. Each line represents the path of magnetization for a randomly chosen T1 and B1 within the range: T1 = 1400-1700 ms and 10% B1 field inhomogeneity. Each black vertical line represents an RF pulse in the scheme. 10 ms spacing between the pulses to simulate a 5 ms RF pulse and a 5 ms spoiler gradient. The simulation assumes instantaneous RF pulses.

Here assuming the static tissue signal in the readout slice has been saturated using a pre-sat pulse, two nonselective inversion pulses are played out at, τ_1 and τ_2, prior to the readout in order to null the signal of components with T1 relaxation rates R_{1opt} and $0.5\ x\ R_{1opt}$ (44,45):

$$\tau_{1,2}(TI) = TI + \frac{2}{R1_{opt}}\log((0.5 \pm 0.25) + (0.5 \mp 0.25)e^{-0.5 \cdot TI \cdot R1_{opt}})$$

Equation 2.6

One consequence of MIR methods is that if the inversion pulses are not ideal then the net effect of multiple pulses can be to reduce the overall signal amplitude of the signal of interest.

2.5.2 Imaging moving blood

All derivations found in this section are courtesy of Bernstein et al. 2004, more complete intermediary steps may be found in Chapters 9 & 10 of the book (2).

Due to the continuous movement of blood through the magnetic field whilst gradients are being played out, the spins accumulate an additional phase shift compared to stationary spins as they experience varying magnetic gradients (46). The resulting flow related dephasing effects gives MRI an intrinsic sensitivity to flow which can be both a helpful property and a source of artefacts. Approaches to either exploit or remove this effect involve manipulating the phase accrual of a stationary or moving spins (depending on the aim of the sequence) by balancing a series of gradient moments.

As shown in the third and final term of Equation 2.2 a stationary spin experiencing a spatially varying magnetic field generated by a gradient will experience a frequency shift. For a given spatial location $r = x$ this equation can be re-written to give the phase accrual for a temporally varying gradient:

$$\phi(t) = \gamma \int_0^t G\,(t)x(t)dt$$

Equation 2.7

Now consider an object or spin at x_0, which is moving at velocity v_0, and acceleration a_0, (using a Taylor series expansion):

$$x(t) = x_0 + v_0 t + \frac{1}{2} a_0 t^2 + \cdots$$

Equation 2.8

Substituting Equation 2.8 into Equation 2.7 and expanding gives a phase accrual of:

$$\phi(t) = \gamma x_0 m_0(t) + \gamma v_0 m_1(t) + \gamma \frac{1}{2} a_o m_2(t)$$

Equation 2.9

Where $m_n(t)$ denotes the nth order gradient moment:

$$m_n(t) = \int_0^t G(t) t^n dt$$

Equation 2.10

The gradient moments can be calculated based on the shape of the gradient G.

2.5.3 Velocity and acceleration selective techniques

Velocity selective or velocity encoding techniques aim to apply a series of gradients such that spins travelling at a maximum target velocity V_{ENC} accrue a maximum phase shift that uniquely maps velocity to phase (180°). The gradients are designed such that all moments that are of lower order than the desired encoding are zero (e.g. for acceleration encoding both the zeroth and first order moments equal zero). For velocity encoding the

zeroth moment, or gradient area, equals zero. To achieve this, bipolar gradients are typically used (gradients with equal and opposite amplitude). It is the first order moment which is then manipulated to induce phase differences which are proportional to the underlying spin velocities and thus enable sensitivity to spins travelling at different velocities.

For the case of perfect (symmetrical and in the absence of eddy current errors) bipolar gradients, the first order moment is the area of just one of the gradient lobes with amplitude A and duration T. Substituting $m_1 = AT$ and $m_0 = 0$ into Equation 2.9, and assuming the duration of the gradients to be fixed, the gradient amplitude to produce a 180° phase shift ($\phi = \pi$) for a given V_{ENC} is:

$$A = \frac{\pi}{\gamma T V_{ENC}}$$

Equation 2.11

Equation 2.11 shows that the area of the gradients is inversely related to the target encoding velocity, therefore an acquisition targeting slow moving spins requires high amplitude gradients. The bipolar gradients for low V_{ENC} scans are therefore more prone to eddy current errors. Eddy currents are generated that oppose the flux of the rapidly changing magnetic field that bipolar gradients create, and scale in proportion with the speed at which the gradients change. The net result is that the area under the gradients, and therefore the phase accrual, may not be exact. Eddy current correction is therefore often required to correct for these effects.

Choosing an appropriate V_{ENC} is critical, and will depend on the target vessel. Studies will often do repeat acquisitions using different V_{ENC} around an estimated value to achieve optimal results.

2.5.4 Flow or velocity compensated imaging

In the case of flow compensation, the gradients are designed to satisfy and null both the zero **and** first order components (47). For a trapezoid slice-select gradient G_s, simply adding a second lobe to form a bipolar set of gradients would not satisfy the first order component therefore two additional gradient lobes G_1 & G_2 are inserted, as shown in Figure 2.15.

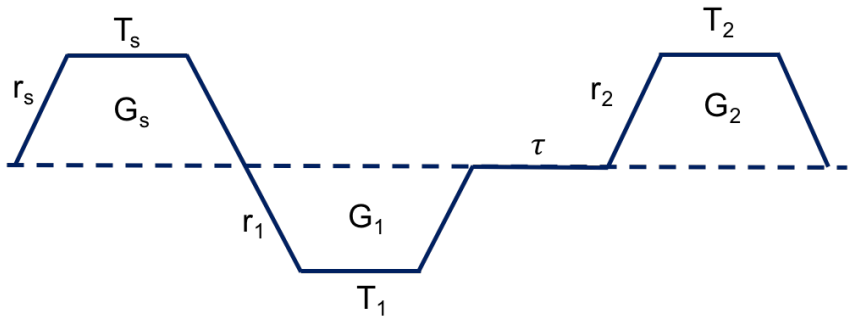


Figure 2.15 Flow-compensated slice-selection for a trapezoidal slice select gradient of total area $G_s.r$ denotes the ramp up/down time which is constrained by the scanner slew rates, T is the duration of the gradient flat-top and the gradients have amplitudes A_s, A_1 and A_2 respectively. An additional short time delay τ is sometimes inserted between the additional lobes if necessary to balance the moments, however often $\tau = 0$.

Balancing the zeroth moment requires $G_1 = G_2 + G_s$ (absolute values of gradient area). The first order moment can be solved to form a quadratic for the unknown gradient lobe

amplitudes (see Bernstein et al. 2004), however sometimes they may have to be determined empirically (2).

In order to achieve the most compact gradients and thus minimise lengthening the gradient duration, the maximum possible amplitudes are chosen for a given slew rate.

2.6 MRI perfusion imaging

Whilst MRI is typically described as non-invasive and non-ionizing, historically the use of additional contrast agents has been the best mechanism for imaging and measuring perfusion of blood in the body. Dynamic Contrast Enhanced (DCE)-MRI and Dynamic Susceptibility Contrast (DSC)-MRI both use intravenous injection of a paramagnetic contrast agent, gadolinium (Gd).

DCE-MRI exploits T1 shortening effects of the gadolinium in the extracellular space. Repeated T1-weighted images before, during, and after the bolus injection measure the transit of gadolinium, the rate of which is determined by perfusion and permeability parameters of the blood and surrounding tissue. Typical imaging times are in the range of 5-10 minutes (48,49).

DSC-MRI measures T2 or T2* (the signal loss induced by the susceptibility difference of the contrast agent) as the bolus travels through the vasculature and from this extracts perfusion parameters such as blood volume, blood flow, and mean transit time. DSC-MRI is performed rapidly following injection as it is reliant on the first pass of the contrast agent through the vascular system and therefore has a short imaging time of around 2 minutes (48,49).

One example of an application of DSC-MRI is to provide perfusion weighted images in PWI/DWI (perfusion weighted imaging/diffusion weighted imaging) mismatch in acute ischemic stroke. Here the mismatch between the reduced signal on perfusion images (due to reduced blood flow to the ischemic region), and the increased diffusion signal (due to the influx of water across the cell membrane as a result of impaired ion transport) is used to identify the ischemic stroke.

Whilst DSC-MRI and DCE-MRI are commonly used clinically (50) although there is an increasing amount of literature showing evidence of gadolinium deposits remaining in the body long after imaging, which have thrown up questions regarding its use in research (51). Arterial Spin Labelling techniques quantitatively measure perfusion using only blood as an endogenous contrast agent, and is therefore more routinely used in research for perfusion imaging.

2.6.1 Arterial spin labelling (ASL)

Arterial spin labelling (ASL) is a completely non-invasive method of quantifying cerebral perfusion, using the blood water protons as an endogenous tracer. The basic principle of ASL is to produce pairs of images whereby the static tissue signals are identical but the magnetization of the blood is different. Subtraction of these two images therefore removes all background signal, yielding an image consisting only of the blood spins.

The development of fast imaging techniques and improved reconstruction methods means ASL MRI has evolved from single-slice acquisitions to high-quality whole brain images, and can even achieve vessel encoded ASL to visualise the perfusion territories of individual blood vessels (52). However, the key steps are the same: there is a labelling

process (usually an inversion) whereby blood spins are targeted, followed by an inflow time, and then a readout.

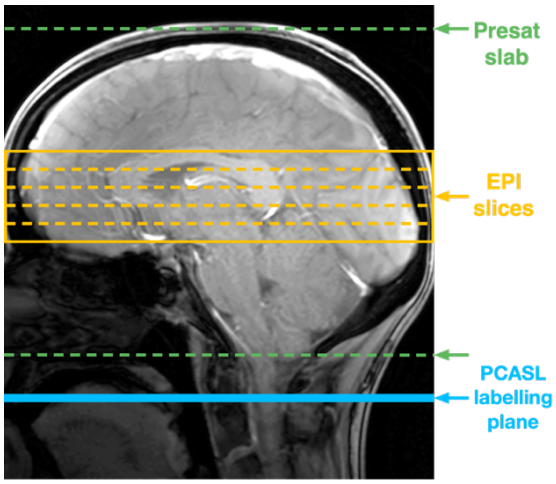


Figure 2.16 Example of slice positioning for a PCASL experiment. Figure created by J. Woods and used with permission

The main forms of ASL are: pulsed ASL (PASL), continuous ASL (CASL), a hybrid of the two, pseudo-continuous ASL (PCASL), and velocity-selective ASL (VSASL). PASL uses short RF pulses (usually inversions) to invert the spins of blood in a slice which then flow into an adjacent imaging plane. In contrast CASL applies a continuous pulse as the spins flow through the labelling region and into the imaging plane, this gives a higher perfusion sensitivity however is more SAR intensive and not all clinical scanners have the ability to produce such pulses. PCASL uses repeated rapid RF-pulses to mimic the continuous labelling approach of CASL and can achieve a similar sensitivity without the limitations of CASL mentioned above (53). The labelling location is typically a slice through the key arteries that feed the brain, as shown in Figure 2.16.

Whilst all of the methods above label the blood spins based on their spatial location, VSASL targets blood spins based on their velocity. VSASL uses bipolar gradients to target spins that have deaccelerated during the acquisition (see 2.5.3) thus the resulting image is weighted towards arterial blood (as blood deaccelerates as it moves from the arteries into smaller vessels) (54,55). Here the labelling is typically performed using saturation pulses rather than inversion pulses and thus the SNR is approximately halved in comparison to other ASL methods (48). As such, despite the potential advantages of VSASL, PCASL remains the most commonly used ASL technique.

The key limitation of ASL is the inherently low SNR. The blood signal is only approximately 0.5-1.5% of the total signal and decays under T1 effects, therefore for longer inflow times the contrast and SNR decreases (56). In VSASL, as well as halving the SNR due to use of a saturation rather than inversion, since only a subset of blood spins are tagged the SNR is even further reduced in comparison to other ASL techniques.

As a positive benefit, however, this inflow delay time provides a reasonable amount of "dead-time" into which additional pulses can be inserted. This time is often used to apply background suppression techniques which have been crucial in improving the SNR of ASL MRI. The ASSIST method described above is one such method used to reduce the signal magnitude (and hence subtraction error) of the static tissue whilst maintaining the blood signal (44).

Despite the limitations described above, ASL MRI has provided significant advantages over the use of intravenous tracers and has started to make the transition from research into the clinic (50).

2.7 MRI oxygen imaging

The origins of the sensitivity of MRI to blood oxygen levels stems from the difference in magnetic susceptibility between oxygenated and deoxygenated blood. The size of the resulting local field distortions depends not only on the susceptibility of the blood inside the vessel (the amount of bound oxygen) but also the size and angle of the vessel relative to the main magnetic field. The distortion in the local magnetic field causes dephasing of the spins which shortens the measured T2* of the surrounding tissue. Similarly, within the vessel the direct influence of the oxygen content of the blood results in a shortening of T2 due to the stronger interaction between the deoxygenated blood and the water spins. T2* is the combined effect of both these (non-refocusable) spin-spin interactions (T2) and the changes in precession due to the local field inhomogeneities (T2′):

$$\frac{1}{T2^*} = \frac{1}{T2} + \frac{1}{T2'}$$

Equation 2.12

The T2′ decay can be refocused using a spin-echo. BOLD contrast approaches therefore measure the influence of blood oxygen on both the T2 and T2′ decay, whereas other methods try to measure T2 directly. Some key methods using both approaches are outlined below.

2.7.1 Calibrated BOLD

BOLD imaging is often used to describe the methods underpinning functional MRI (fMRI) experiments which aim to measure changes in neuronal activation during a task

(57). T2* sensitive images are acquired using a GRE sequence with an echo time TE comparable to the T2* (TE ~ T2*). However, fMRI is not a quantitative method and is based on identifying a statistical difference from an arbitrary baseline.

The neurophysiology underpinning changes in the BOLD signal is based on the increase in CBF that arises due to neural activation, leading to increased blood oxygenation levels. With less deoxygenated blood in the voxel the MR signal increases, resulting in a positive BOLD effect (58). However, the percentage volume of deoxygenated blood in the voxel is also altered. Disentangling the complex relationship between these parameters, CBF, CBV, and the concentration of deoxyhaemoglobin in the blood [dHb] remains a challenging task and an ill-posed problem. Obtaining a quantitative measure of the BOLD response is complicated further by its dependence on the baseline physiological state, driven by the blood haematocrit, resting OEF, and CBV.

The most successful class of methods which aim to quantitatively measure voxelwise BOLD signal changes and thus changes in oxygen metabolism are known as calibrated BOLD. Gas inhalation techniques are used to create a baseline, or "calibration constant", M, from which changes during activation are measured.

These use multi-parametric models, based on the Davis model to relate the BOLD signal to the physiological parameters underlying the metabolic demand such as CBF and $CMRO_2$ (59):

$$\frac{\Delta BOLD}{BOLD_0} = M\left(1 - \left(\frac{CBV}{CBV_0}\right)\left(\frac{[dHb]}{[dHb]_0}\right)^{\beta}\right)$$

Equation 2.13

where M is dependent on the echo time TE, CBV_0 and [dHb] (the subscript 0 indicates the baseline state). Using Fick's principle: $CMRO_2 = CBF(Y_a - Y_v)C_a$ (C_a represents the oxygen carrying capacity of blood and is related to haematocrit) and the Grubb power law: $\Delta CBV = \Delta CBF^{\alpha}$ (where the exact value of α is under debate but varies with experimental conditions between 0.2-0.5 (60,61)) this becomes:

$$\frac{\Delta BOLD}{BOLD_0} = M\left(1 - \left(\frac{CMRO_2}{CMRO_{2,0}}\right)^{\beta}\left(\frac{CBF}{CBF_0}\right)^{\alpha-\beta}\right)$$

Equation 2.14

The two most commonly used gas challenges are CO_2 enriched air (hypercapnia) and O_2 enriched air inhalation (hyperoxia) (62). Hypercapnia causes vasodilation, which increases CBF but does not alter $CMRO_2$. Therefore, any changes in $CMRO_2$ due to a stimulus or disease can be measured relative to this "baseline" $CMRO_2$ value, so long as the measurement parameters are kept constant.

Hyperoxia however, allows for absolute measure of $CMRO_2$ by changing the oxygen saturation of the blood Y (63). Under these conditions the calibration equation becomes:

$$\frac{\Delta BOLD}{BOLD_0} = M\left(1 - \left(\frac{CBF}{CBF_0}\right)^{\alpha}\left(\frac{[dHb]}{[dHb]_0} + \frac{CBF_0}{CBF} - 1\right)^{\beta}\right)$$

Equation 2.15

thus allowing OEF to be calculated from the measured change in [dHb]. An oxygen gas challenge is advantageous as it only affects the venous side of the vascular tree and therefore provides a more independent measure. Hyperoxia also has fewer noticeable side effects than hypercapnia. However its effect is much smaller and therefore has a lower SNR.

An approach whereby both O_2 and CO_2 gas challenges are combined is called dual-calibrated functional MRI (dcfMRI) and aims to quantify both CBF and venous oxygenation in the same acquisition and thus obtain a more accurate measure of $CMRO_2$ (63,64).

The benefit of the above methods is that they use simple GRE sequences which are available on most scanners. However performing a gas challenge is not trivial in either healthy or clinical populations, and inhalation methods may not be well tolerated by patients where consistent deep breathing is difficult. Generally, it has been found that hyperoxia is better tolerated than hypercapnia, with fewer noticeable side effects.

The models are calibrated using constraints from healthy physiology but struggle in disease when the parameters lie outside the usual bounds. Changes in physiology due to stroke or similar conditions may undermine the assumptions made during calibration. Even within healthy participants, the hyperoxia model assumes that CBF is unchanged during O_2 inhalation, which may not be accurate. Similar to ASL these methods also

suffer from inherently low SNR with only ~3% of the voxel volume made of up deoxygenated blood in the grey matter. Recent work has also started using asymmetric spin echo (ASE) sequences, which aim to refocus the dephasing effects of the deoxyhaemoglobin on the MR signal and thus do not require a gas challenge (65).

2.7.2 T2 based methods

T2-based methods rely on a theoretical and empirically derived relationship between the transverse relaxation time T2 of the blood, and the oxygenation levels in the blood. These methods are also distinguished from the BOLD-based methods as they aim to isolate the blood signal from the tissue component. The vast majority of these methods maximise the sensitivity of the T2 blood measurement by using a form of the CPMG sequence described in 2.3.2. The relationship between blood T2 and blood oxygenation is then derived from a model using a compartment weighted sum of relaxation rates from plasma, and haemoglobin contributions inside the red blood cells (erythrocytes):

$$\frac{1}{T_2} = R_{2,0} + hct \cdot (1 - hct) \cdot (\Delta w)^2 \cdot \tau \left[1 - \frac{2\tau}{\tau_{CPMG}} tanh \frac{\tau_{CPMG}}{2\tau}\right]$$

Equation 2.16

Where $R_{2,0}$ is the relaxation rate factor from plasma and erythrocytes, hct is the haematocrit of the blood, Δw is the susceptibility shift difference due to diamagnetic, oxygenated and deoxygenated blood contributions, τ is the exchange lifetime, and τ_{CPMG} is the inter-echo spacing in the CPMG encoding sequence (66). From this equation the following relationship can be derived:

$$\frac{1}{T2} = A + B \cdot (1 - Y) + C \cdot (1 - Y)^2$$

Equation 2.17

Where Y is the blood oxygenation level. Assuming arterial blood to be fully oxygenated $(1 - Y_v)$ gives OEF. A, B, and C are parameters which in turn are dependent on the haematocrit of the blood:

$$A = a_1 + a_2 \cdot hct + a_3 \cdot hct^2$$

$$B = b_1 \cdot hct + b_2 \cdot hct^2$$

$$C = c_1 \cdot hct \cdot (1 - hct)$$

Equation 2.18

These coefficients have been derived via *in vitro* experiments using bovine blood by Lu et al. (2012) for a range of τ_{CPMG} values (5, 10, 15 & 20ms) (67). Bovine blood is used as it has similar properties to human blood in terms of erythrocyte size, haemoglobin content, and diffusion permeability (66).

Whilst each method uses a similar T2-encoding method, they differ in their approach to isolating the blood signal from the surrounding static tissue. The method on which this work is based is T2-Relaxation-Under-Spin-Tagging (TRUST) and is outlined in more detail in Chapter 3. Briefly however, TRUST uses the same principles as ASL described above to subtract the background tissue. Pairs of images are acquired with different magnetization conditions applied to the blood spins. Where TRUST differs from ASL is that these conditions are applied to the blood in the cerebral vasculature, and measured

in the venous system, rather than in the arterial blood as is done in ASL. Whilst it has proven robust, the method lacks any spatial specificity.

Three other key methods: QUIXOTIC, VSEAN, and TRU-PC, which have come closest to spatially specific measurements of cerebral oxygenation through measurement of T2 in blood vessels are introduced here below.

2.7.3 QUIXOTIC

Quantitative Imaging of eXtraction of Oxygen and Tissue Consumption (QUIXOTIC) also takes principles from ASL, specifically VSASL (68). Velocity-selective spin labelling methods (venular-targeted VSSL (VT-VSSL)) are used to isolate postcapillary venular (PCV) signal. Two velocity-selective modules VS1 and VS2 are applied: VS1 selects slow moving spins such as those in capillaries and small venules using a low V_{CUTOFF}, and VS2 is alternated between another user-defined cut off velocity V_{CUTOFF} and disabling the velocity selection (V_{CUTOFF} = infinity) to provide the control and tag conditions respectively. Therefore, the image is weighted towards any spins that have accelerated through V_{CUTOFF} during the delay between VS1 and VS2, thus targeting venous spins. A T2-encoding module similar to the CPMG module is inserted in VS2. By repeating the experiment for different T2-weightings an estimate of the venous blood T2 is acquired. An additional inversion pulse is inserted between VS1 and VS2 in order to null any T1 relaxation effects from arterial blood.

Through these means QUIXOTIC provides voxel wise maps of venous blood T2, and thus estimates parameters such as Y_v, OEF, and when combined with perfusion information, $CMRO_2$. However, the method is not without limitations and deficiencies.

Firstly, accurate assumptions of V_{CUTOFF} and an appropriate delay between the two VS modules is necessary to maximise the targeted blood signal. Additionally, as the flow-sensitive gradients are not used in both conditions (tag and control) there is risk of contamination of the venous signal by CSF water diffusion (54). The arterial nulling pulse is also detrimental to the overall SNR as the venous blood signal is also affected. Finally, the method also assumes laminar and uniform flow between the arteries, capillaries and venous blood.

2.7.4 VSEAN

Venous Oxygenation Mapping using Velocity-Selective Excitation and Arterial Nulling (VSEAN) is a further MR strategy for mapping oxygenation in the brain and was designed to improve on the limitations of the QUIXOTIC method described above (69). The arterial nulling inversion pulse is selective and placed below the imaging plane so that it does not interfere with the venous blood signal in the slice, thus improving the SNR. The velocity-selective gradients are then timed to coincide with the null point of any arterial blood which may have flowed into the slice. Additional phase cycling is introduced to the velocity selective module such that static tissue can be separated from the venous signal based on a $\pi/2$ phase shift.

There are a number of aspects within the VSEAN sequence that are still being optimised to improve the performance of the method. These are largely focused on the T1 nulling approach as it is sensitive to changes in arterial transit time that may occur in disease, and also limits the technique to a single-slice acquisition.

2.7.5 TRU-PC

A third method, T2-Relaxation-Under-Phase-Contrast (TRU-PC) MRI also utilizes the relationship between venous blood T2 and oxygenation levels, and the bipolar flow gradients similar to those used in QUIXOTIC and VSEAN (70). What separates TRU-PC from these two methods however is that the polarity of the flow encoding gradients are flipped during the control condition, instead of simply being switched off as is done in the earlier methods. As a result, the phase of the venous spins during the tag and control conditions is $+\phi$ and $-\phi$ respectively. The complex difference between the tag and control conditions therefore removes the static tissue signal, and upweights the venous blood signal by $2M_{blood}|sin(\phi)|$.

This method is also sensitive to eddy current errors and at low V_{ENC} values, the T2 (and thus Y_v) of venous blood in the sagittal sinus has been found to be overestimated due to these effects (71).

The method has been used to target venous blood in different ocations through the superior sagittal sinus, as well as other draining veins as small as 1-2 mm in diameter, and has been validated using gas and caffeine challenges (71).

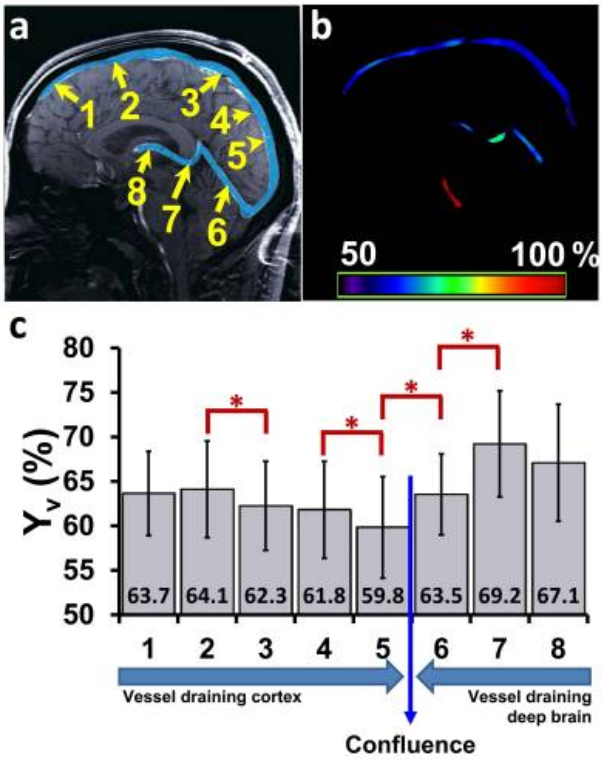


Figure 2.17 TRU-PC measuring the venous oxygenation in different parts of the sagittal sinus. Figure by Krishnamurthy et al. (70) and used with permission from Wiley publishing.

2.7.6 TRUST

Whilst promising approaches, the methods described above are still in their infancy of development and going through incremental changes and improvements. In comparison, the TRUST method generally has higher SNR, and less confounding factors to contend with. The sequence is fairly well established, and has been tested in diseases such as sickle cell anaemia (72), Alzheimer's (73), and normal aging (74). Validation studies have been done using hypercapnia (75), and caffeine challenges (76). Its reproducibility has been demonstrated in both a test-retest study (77) and in a multi-site study with over 250 healthy volunteers (78). TRUST has also been applied in abdominal MRI, to assess

renal function of the kidneys (79). In general, there is evidence of sufficient robustness for clinical use, which has not been established with other MR methods.

Overall, this makes TRUST a good candidate for further development as a regional method.

Chapter 3 Selective Localized T2-Relaxation-Under-Spin-Tagging

3.1 Introduction

The MR sequence developed in this work is based on an existing MR method called T2-relaxation-under-spin-tagging (TRUST). TRUST was first developed by Lu et al. as a method of measuring whole-brain OEF via measurement of venous blood T2 in the superior sagittal sinus (67). The superior sagittal sinus is one of the largest draining veins and is conveniently situated running down the back of the head and therefore making it easily identifiable, as shown in Figure 2.4. The sensitivity of TRUST to changes in venous blood oxygenation has been verified in a number of diseases and conditions. However, due to the global nature of the measurement it is insufficient for those applications in cerebrovascular disease where the changes to venous oxygenation may be more localized. This work aims to address the limitations of TRUST and obtain spatially localized measurements of venous blood T2. This new sequence is called Selective Localised TRUST (SL-TRUST).

3.2 T2-Relaxation-Under-Spin-Tagging

As briefly outlined above T2-Relaxation-Under-Spin-Tagging (TRUST) is a non-invasive MR method for measuring global cerebral OEF (67). Referring back to the framework outlining ASL, described in 2.6.1, it is possible to describe TRUST as a form of "upside-down" ASL.

TRUST performs an interleaved on/off inversion tagging pulse, however rather than performing this on inflowing blood in the main arteries, it is instead performed in a large slab in the brain, targeting blood spins in the venous vasculature. The imaging slice is then placed downstream of this tagging slab, capturing the blood spins of venous blood as they flow out of the brain. The imaging slice is positioned to intersect the superior sagittal sinus, and played out at a time TI following the inversion. An advantage of working in this venous sinus is that the vessel walls are not permeable to water molecules and therefore there is no contribution from the effects of proton exchange between the blood and the tissue, which is of concern in ASL (67).

In order to acquire a T2-sensitive measurement of blood the TRUST sequence utilizes an MLEV-4 T2- encoding module, as described in 2.3.2. T2-encoding of the draining blood is performed just before the readout and, whilst it is applied globally, due to the pairwise subtraction of tag and control images only the T2 of tagged spins are left in the final difference image. The magnitude of the T2-weighting, and thus the attenuation of the venous blood signal measured in the superior sagittal sinus, is determined by the number of repeated echo blocks, the (progressively increased) total duration of which is called the effective echo time (eTE). The full TRUST pulse sequence is shown in Figure 3.2.

The venous blood T2 value can therefore be calculated from the decay time constant of a plot of signal intensity against eTE, using the mono-exponential given in Equation 3.1:

$$\Delta S = S_0 e^{eTE(\frac{1}{T_{1v}} - \frac{1}{T2_v})}$$

Equation 3.1

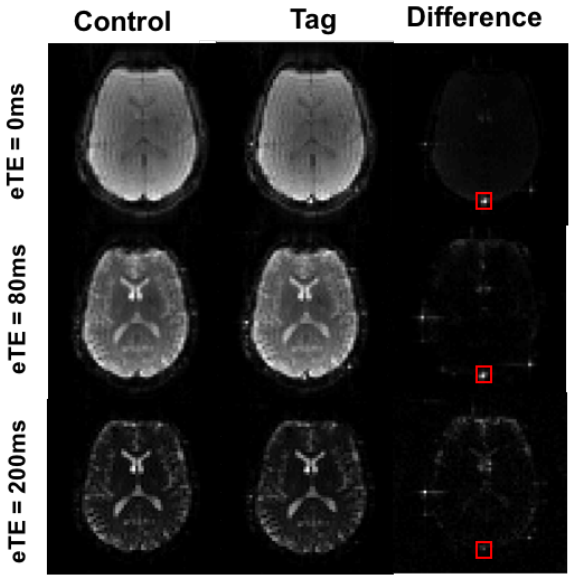


Figure 3.1 Control, tag, and difference images for TRUST at varying eTE. The sagittal sinus ROI is identified in red

Where S_0 is the pure venous blood signal when no T2 weighting is applied, and T_{1v} is fixed at a representative value of 1612 ms, derived from $R_{1v} = 0.62s^{-1}$ (80).

Example tag, control, and difference images for TRUST, with the sagittal sinus highlighted in red are displayed in Figure 3.1.

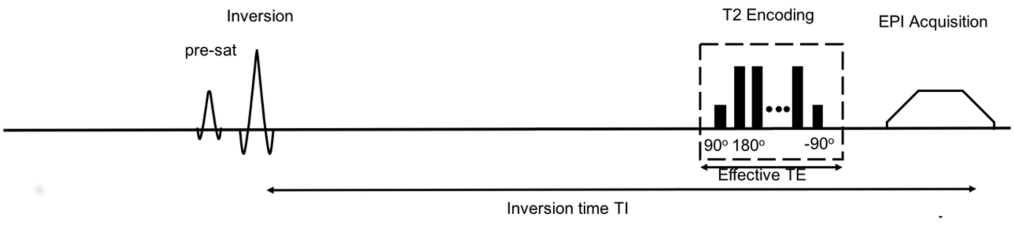


Figure 3.2 TRUST pulse sequence diagram

3.3 Selective Localized T2-Relaxation-Under-Spin-Tagging

Whilst it has been a highly influential method of evaluating cerebral OEF the TRUST method described above is restricted to whole-brain measurements of OEF, with no way to distinguish between blood spins which have originated from different regions of the brain. This is in large part due to the position of the T2-weighting module. With the T2-encoding immediately before the readout, the measured signal is always a sum of spins which have originated from all over the brain, with no method of distinguishing between them.

The first step towards a localized measurement is to move this T2-encoding module further away from the readout. The T2-encoding is therefore moved to the beginning of the sequence, prior to the inversion tag pulse, enabling the T2 of the blood to be encoded into the signal while the blood spins are still in the small local draining venules and veins, rather than in the major sagittal sinus vein. The sequence in this form is called Global SL-TRUST as it is still a global measurement but capable of regional localisation following the next step. Figure 3.3 and Figure 3.4 show the path of the magnetisation at the start of a global SL-TRUST sequence, as the T2-prep using an MLEV-4 strategy is performed followed by an inversion.

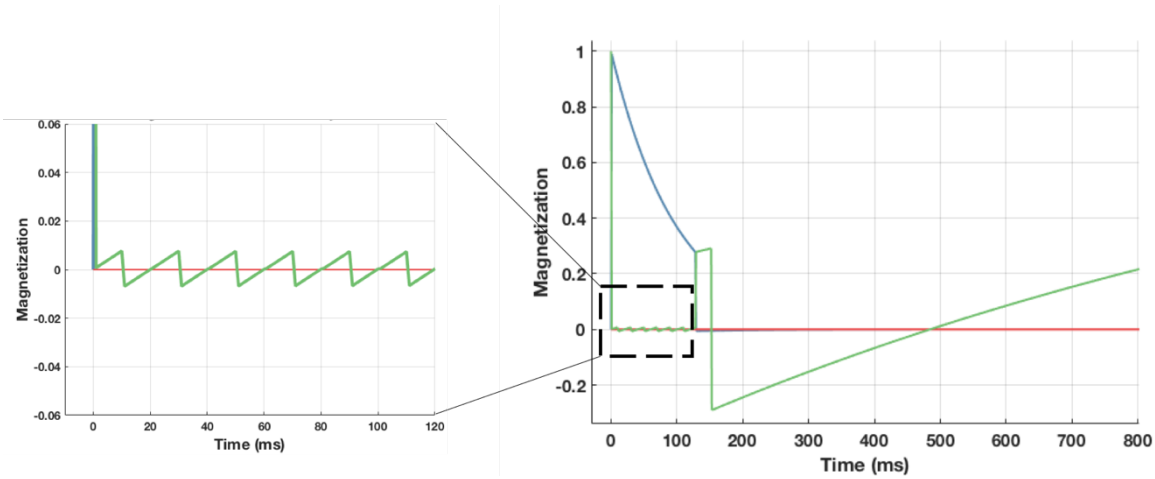


Figure 3.3 Bloch simulation of the evolution of both the transverse (blue) and longitudinal (green) magnetisation during the T2-prep module followed by an inversion. The T2-prep uses an MLEV-4 strategy whereby multiple 180° pulses continuously refocus the magnetisation (phase cycling not shown).

Moving the T2-encoding module allows the insertion of spatial saturation pulses between the T2-encoding and the signal measurement. The role of this spatial saturation scheme is to null or dephase the spins in areas of the brain which are not of interest, so that they do not contribute to the overall signal eventually measured in the sagittal sinus. An additional two inversion pulses are inserted in-between the spatial saturation and the readout, for background suppression of static tissue signal. Both the method of spatial saturation and the purpose of the background suppression pulses are explained in more detail in 3.5 and 3.6.2 respectively.

The equation for the venous blood signal between the tag and control scans ΔS for SL-TRUST is given by:

$$\Delta S = S_0 e^{-\frac{eTE}{T2_v}}$$

Equation 3.2

Where S_0 contains the exponential term for the T1 recovery over the inversion time TI: $e^{-\frac{TI}{T_{1v}}}$. Equation 3.2 differs from the equation for TRUST given in Equation 3.1 as in the TRUST sequence the time during which the signal undergoes T1 recovery changes depending on eTE, $t = TI - eTE$.

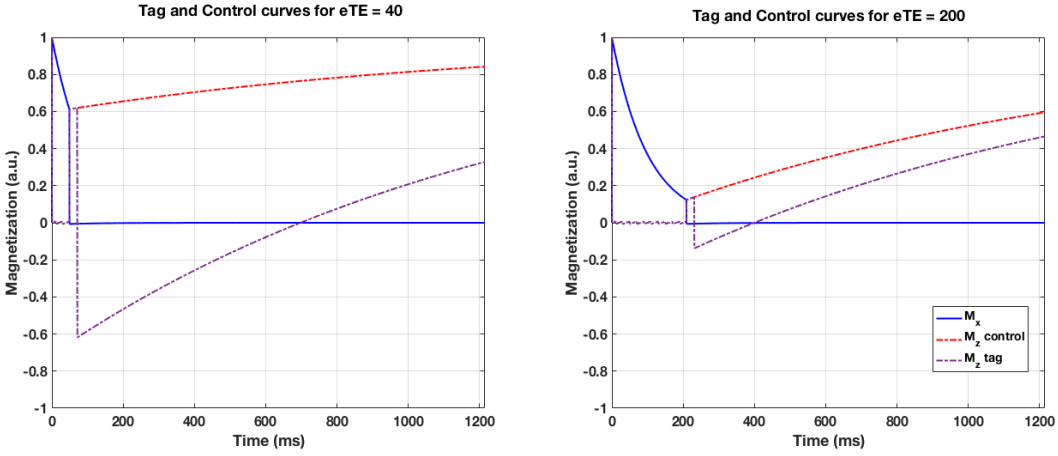


Figure 3.4 Bloch simulations showing the evolution in magnetisation for both tag and control conditions for two effective echo times eTE = 40 & 200 ms. The measured signal is proportional to the difference between the tag and control curves at the time of the readout.

Figure 3.6 shows the full pulse sequence for SL-TRUST, with the original TRUST sequence shown in Figure 3.2 for comparison. The geometric placement of various components of the SL-TRUST sequence are shown in Figure 3.5.

The following sections examine each component of the SL-TRUST sequence and outline how they were optimized to maximise signal, minimise noise, and maintain clinical applicability.

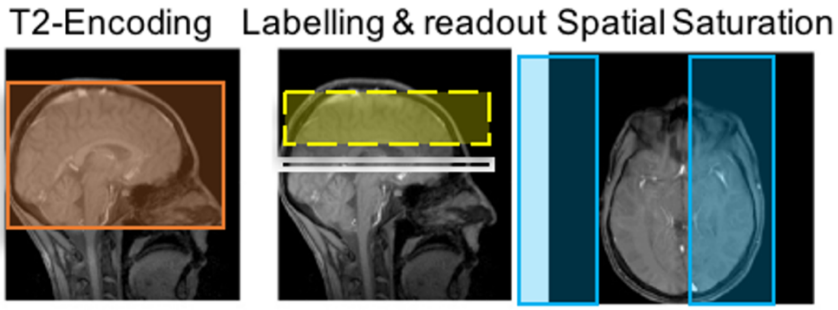


Figure 3.5 Geometric placement of each component of SL-TRUST for a hemispherical regional measurement.

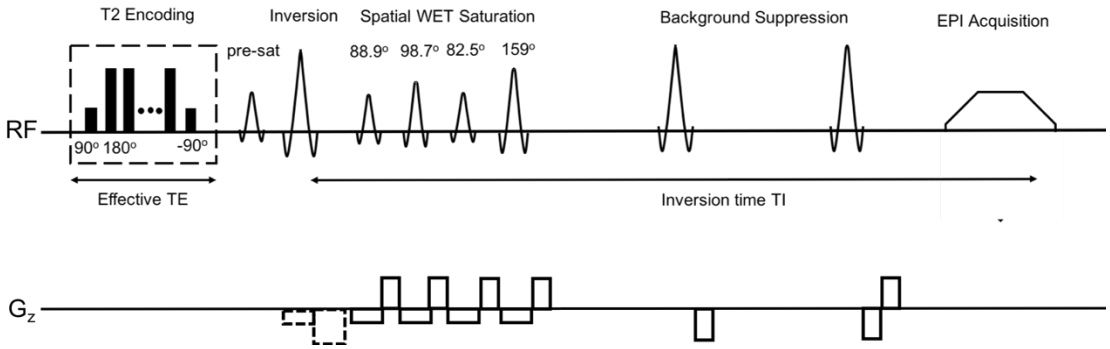


Figure 3.6 SL-TRUST pulse sequence diagram including the gradients in G_z to demonstrate the selective gradients and spoilers for the inversion and the background suppression pulses in z. Gradients and pulses not drawn to scale, for demonstrative purposes only. No gradients shown for the EPI acquisition block.

3.4 Optimizing sequence timings

There are a number of sequence timings which can be optimized within the sequence to ensure optimal performance. The following two sections focus on the optimization of the inversion time (TI) and repetition time (TR).

3.4.1 Inversion time TI

The inversion time (TI) is the time that elapses between the inversion "tag" and the readout. During this time the blood flows from the tagging slab, downstream through the superior sagittal sinus, into the imaging slice. This must be optimized such that it is long enough for blood to flow from the inversion slab into the readout slice, maximising signal, but short enough such that the signal has not decayed too significantly under T1 effects. The initial TRUST sequence uses an inversion time of 1200 ms, as this is the point at which the signal intensity appeared to plateau (8). The added advantage is that it is beyond the blood T1 nulling point (approximately 1088 ms assuming a $T1_{blood}$ = 1624 ms) (8) and as a result, the original TRUST sequence could perform a magnitude image subtraction as the polarity of the blood signal was always positive.

To establish an appropriate inversion time which could be used for both TRUST and SL-TRUST an experiment was conducted, acquired at the maximum image contrast (eTE = 0 ms), using a series of incrementing inversion times (TI = 100 – 1200 ms, $\Delta TI = 50\ ms$), in five healthy participants (mean age = 36 y, 2 males). In SL-TRUST a thin mid-sagittal saturation band was placed covering the sagittal sinus, to saturate those blood

spins that were already in the sagittal sinus and that would thus otherwise arrive first in the imaging plane.

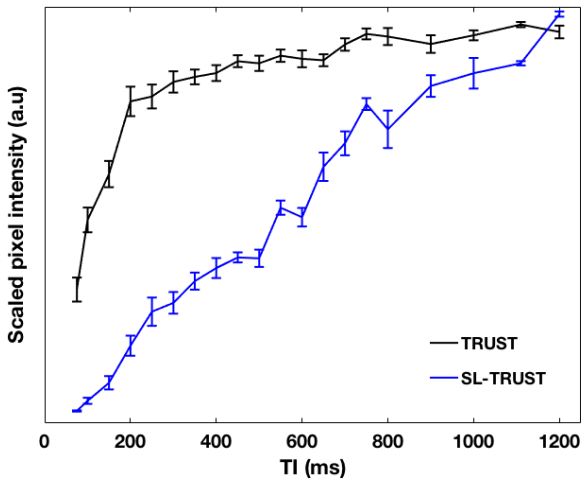


Figure 3.7 Curve showing tag-control difference signal versus Inversion time for TRUST and SL-TRUST. Due to saturation bands through the sagittal sinus in SL-TRUST the first spins contributing signal arrive later.

T1 decay correction was performed using $T1_{blood}$ = 1624 ms (8) and multiplying the signal intensity at each TI by a correction factor $2 * exp(-\frac{TI}{T1_{blood}})$. The results are shown in Figure 3.7. For TRUST the signal intensity plateaus earlier than reported by Lu et al, with maximum signal intensity reached by 800 ms. However, for SL-TRUST with saturation bands through the sagittal sinus this is delayed by approximately 400 ms, at which point the two curves intersect. It is not expected that the curves continue increasing in signal intensity for any inversion times longer than 1200 ms but instead that the curves begin to plateau. Further discussion of this assumption can be found in Chapter 6. For all future measurements in healthy participant cohorts, therefore, an inversion time of TI = 1200 ms is used.

It is possible that due to the localized targeting of SL-TRUST the optimal TI time may be more sensitive to differences in cerebral blood flow (CBF) which arise in clinical cohorts, such as stroke patients. In these populations some initial measurements or estimations of CBF would be helpful in order to adjust the inversion time accordingly and maximise signal. However, at very long inversion times there is a risk that the signal becomes sensitive to the T2 of capillary or tissue water, rather than the T2 of the blood, something that would have to be investigated further. This is due to the exchange of spins from within the tissue into the capillaries, and subsequently flow into the veins.

3.4.2 Repetition time TR

The repetition time TR is the duration between consecutive measurements. In the case of both TRUST and SL-TRUST, the TR must be long enough for adequate refreshment of the blood pool between measurements, and is therefore constrained to a certain degree by the brain physiology. The TR must also be sufficiently long for any residual magnetization effects to have dissipated by the time the following measurement begins. The T2-preparation RF pulses in early TRs may result in magnetization disturbances, this effect scales proportionally with the length of the T2-preparation and thus there is a risk of underestimating the venous blood T2 if the repetition time is too short. For this reason the initial TRUST sequence used a relatively long TR of 8 seconds (8). However, a long TR extends the overall scan time, and can therefore affect the clinical applicability. Later literature investigating the effect of TR on T2 by Xu et al. showed the effect described above could be mitigated by inserting a non-selective 90° saturation pulse at the end of

each TR to reset the magnetization. In doing so a minimum TR = 3 s was achieved, but at the cost of the measurement precision (67).

For the SL-TRUST sequence, three potential TRs were investigated, TR = 8, 6, 4 seconds, in 4 subjects (mean age = 39 y, 3 males), over 3-5 repeat measurements. SL-TRUST sequences both with and without background suppression were tested (see section 3.6.2 for full discussion of the background suppression), the results of which are shown in Table 3.1 and Figure 3.8. Table 3.1 shows the average T2 and the standard deviation across multiple measurements, for each subject at each TR. Figure 3.8 shows the underlying T2 values used to generate Table 3.1 in faded dashed lines, and the T2 derived from the mono-exponential decay of the average T2-decay curves of each measurement is shown in bold. A slight but not significant increase in T2 is observed using the shortest TR of 4 seconds compared to the longest, 8 seconds. Overall the systematic underestimation of T2 at shorter TR values reported by previous TRUST studies is not observed here (67). However, there is a lower overall signal intensity at shorter TRs. The average effect is a 6.13 % and 14.21% reduction in signal for TR = 6 and 4 s respectively, compared to TR = 8 s. Assuming the noise is constant and that the SNR scales with $\sqrt{N}$ where N is the number of repeat measurements, only 1.36 and 1.14 times more measurements are required to make up for this loss in signal as a result of using a shorter TR of 4 seconds. In comparison to doubling the scan time this is a net time cost benefit, therefore a TR = 4s was chosen for all subsequent SL-TRUST experiments.

Table 3.1 T2 dependence on TR for 4 subjects, both with and without background suppression. Mean calculated from the underlying data shown in Figure 3.8. (mean ± std across multiple measurements)

		T2 (ms) (mean ± std)		
	Subject #	**TR = 4 s**	**TR = 6 s**	**TR = 8 s**
NO BGS	1	86.0 ± 7.5	93.5 ± 6.6	94.5 ± 3.1
	2	83.5 ± 21.2	87.2 ± 21.1	89.8 ± 24.5
BGS	3	57.2 ± 2.1	55.5 ± 1.1	55.5 ± 1.3
	4	70.6 ± 6.2	67.1 ± 5.0	67.4 ± 4.6

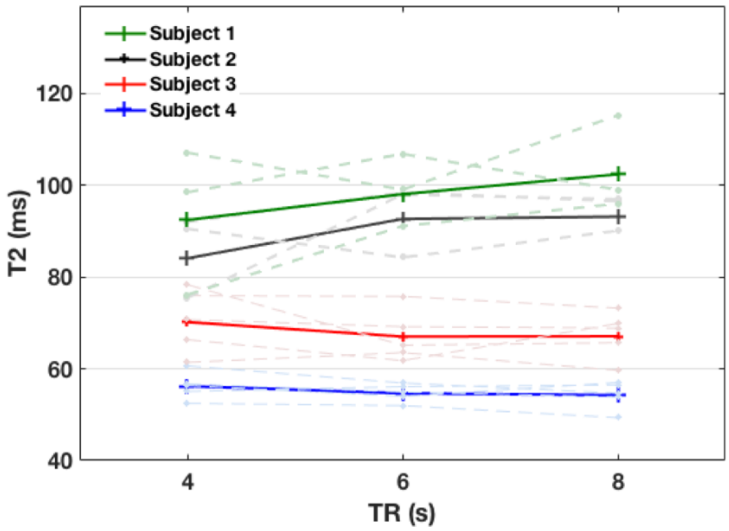


Figure 3.8 T2 values in the sagittal sinus for global SL-TRUST for a range of repetition times TR = 4, 6, 8 s at TI = 1200 ms. The T2 values from the averaged T2 curves are shown in bold, with the T2 values from individual underlying curves shown as dashed lines.

3.5 Spatial saturation

Effective and efficient spatial saturation is critical for the SL-TRUST sequence in order to achieve accurate signal localization, without contamination from neighbouring regions. This requires the saturation scheme to have both near perfect saturation of blood signal, and a sharp profile.

Spatial saturation is performed immediately after the inversion, targeting (unwanted) spins before they have flowed from the site of inversion and mixed with (wanted) spins from other regions.

Initially, a simple combination of two repeated 90° pulses was used, each followed by a spoiler gradient. Whilst this was sufficient for proof of concept, this simple scheme had poor saturation efficiency and profile, as shown in Figure 3.9.

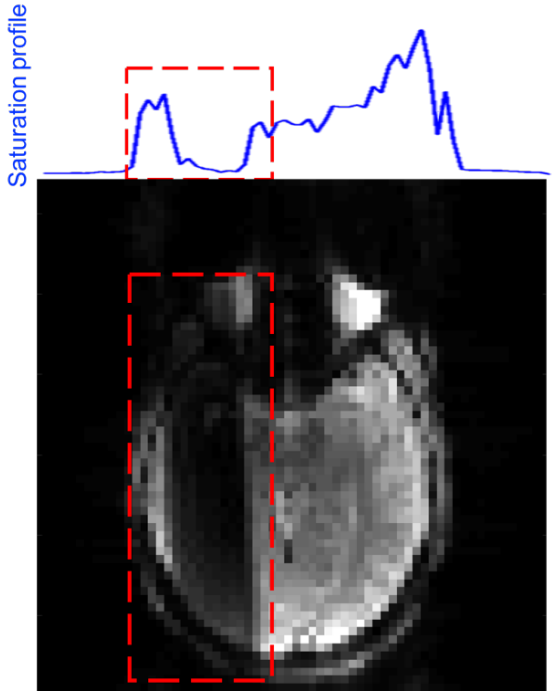


Figure 3.9 Poor saturation profile of standard product saturation pulses. The red box indicates the intended saturation region, representative of a hemispheric saturation.

3.5.1 WET saturation

The WET saturation scheme introduced in 2.5.1 was originally developed as a non-selective method in spectroscopy. However, it has since been demonstrated as a gradient selective saturation method with a scheme of four RF pulses (88.9°, 98.7°, 82.5°, 159°) with 10 ms intervals between pulse centres and was applied successfully in ASL (81,82).

Due to this success in a related MR sequence, the same WET saturation scheme was applied in SL-TRUST. Figure 3.10 shows the improvement in saturation efficiency and profile of the varying flip angle WET scheme in comparison to a Siemens product saturation pulse.

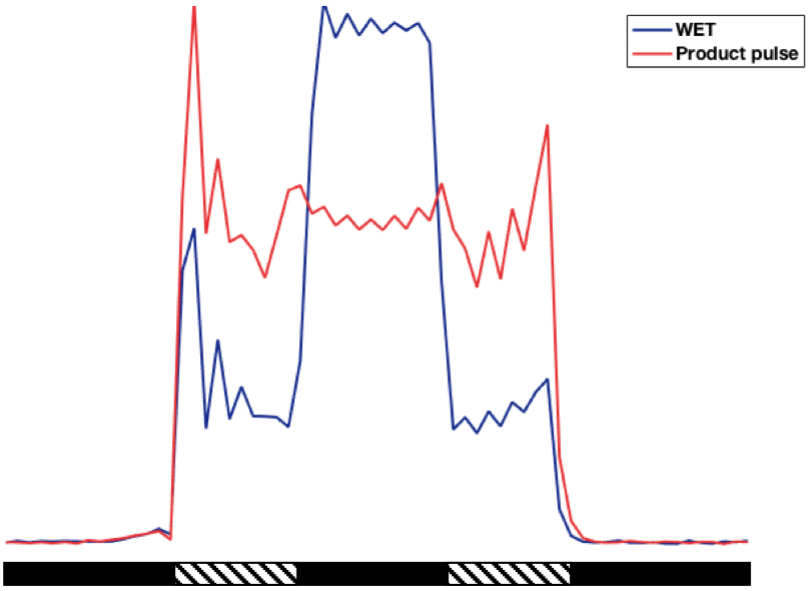


Figure 3.10 Comparison of two saturation schemes to saturate two slabs at the edges of a circular phantom, the desired saturated regions are shown as the crosshatched areas on the black band. The WET saturation (blue) is cosine modulated (see below) to produce two bands straddling the centre. Two product pulses (red) are positioned to saturate the same regions. There is some T1 recovery between the saturation and the acquisition meaning the signal is not completely nulled in the saturated regions in this example.

3.5.2 Cosine modulation

A drawback of the WET saturation scheme is the length of time required to play out the four RF pulses and their associated spoiler gradients. In order to achieve 3D localization at least 4 coronally- and sagitally-orientated saturation bands are required, 2 either side of the target region, in both the x and y dimensions, with the third axis defined by the axial inversion slab. Using WET in its current state and assuming an inter-pulse spacing of 10 ms, this would take over 160 ms.

To reduce the time taken to achieve full spatial saturation, the WET saturation pulses were cosine modulated, such that two parallel saturation bands that straddle the region that is to be retained are produced at the same time.

A modulation factor M is applied to each point (i) in the sinc pulse along a phase ramp PR:

$$PR = \frac{\left(\left(i - \frac{n}{2}\right)\ x\ tbw\ x\ \pi\right)}{n}$$

Equation 3.3

$$M = \cos\left(\frac{Distance\ between\ saturation\ bands}{Thickness\ of\ saturation\ bands}\ x\ PR\right)$$

Equation 3.4

where *n* is the number of points used to generate the pulse on the scanner, and tbw is the time-bandwidth product. Due to the additive nature of the phase, however, this results in the amplitude of the cosine modulated pulse being double that of the original sinc pulse,

see Figure 3.11. This lead to large voltage requests and RF clipping, overdriving the pulse amplitude and causing the amplifier to re-scale the pulses such that they no longer produce the correct flip angle. To circumvent this RF clipping, the two pulses were modified to be played out with a short time shift between them. This time shift was derived analytically to find a shift which reduces the amplitude of the two pulses such that they are sufficiently close or equal to the original amplitude, see Figure 3.11. This resulted in only a 25% increase in the overall pulse duration. To separate the two pulses, Euler's formula to express cosine as a weighted sum of two exponentials is used: $\cos(x) = \frac{e^{ix}+e^{-ix}}{2}$. The cosine modulation is applied as a sum of two exponentials which can be temporally separated so that they do not fully overlap.

In practice on the scanner the region to be retained is graphically prescribed by the user, with a maximum of two WET saturation schemes (therefore giving 4 saturation bands). The thickness of the saturation bands is defined such that they at least reach the outer edges of the brain. Thus, spatial saturation of large portions of the brain is achieved within the physiological time limitations of the sequence.

For the remainder of this thesis two regional SL-TRUST measurements are typically acquired: one isolates blood from a single hemisphere (referred to as RHS, denoting Right Hand Side), using just one WET saturation band (separated into two parallel bands as described above, with one band positioned outside the brain), and one localizes further to a 70x70 mm^3 tissue region above the middle cerebral artery, a large artery prone to stroke (referred to as MCA), using two WET saturation schemes. An example of the placement

of the WET saturation bands to target the MCA territory, using the arrangement described above, is shown in Figure 3.12.

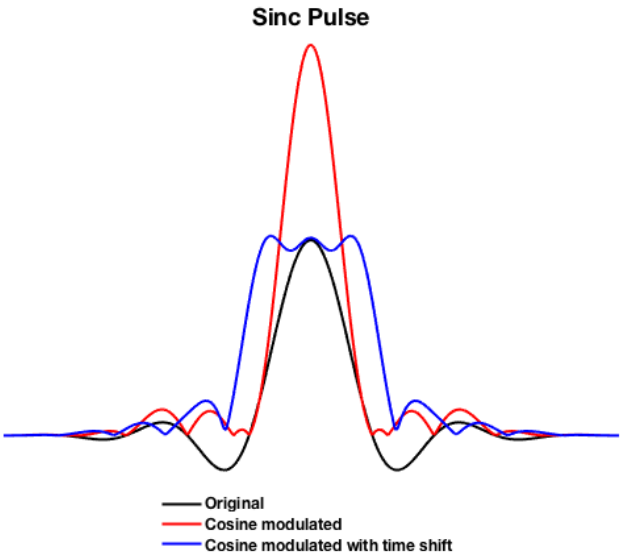


Figure 3.11 Cosine modulating a sinc pulse: Without an added time shift the amplitude of the pulse is doubled and thus risks being clipped.

To assess the saturation efficiency of the saturation pulses the amount of signal lost at eTE = 0 ms (maximum contrast/blood signal) is assessed in 6 subjects. Averaging across multiple measurements in each subject a signal decrease of 64.5 ± 15.4% and 78.8 ± 11.5% is found for RHS and MCA SL-TRUST respectively, in comparison to global SL-TRUST. This is an indicator of how much blood signal is removed. In the case of hemispherical saturation this is slightly higher than the 50% signal reduction that might be expected. This can possibly be explained by the placement of the saturation bands, which extends a short distance into the contralateral hemisphere in order to cover the sagittal sinus.

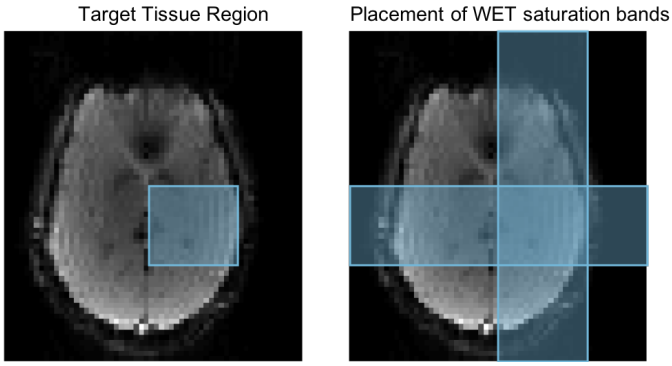


Figure 3.12 Illustration of the target MCA territory and the placement of two WET saturation bands by the user on the scanner to achieve this. In practice the regions straddling where the bands are placed are saturated. Therefore the overlapping region where the bands intersect is retained, and everything outside is removed.

3.6 Signal instability

Initial measurements for regional SL-TRUST revealed large fluctuations in the signal measured in the sagittal sinus, in comparison to TRUST or global SL-TRUST. Figure 3.13 shows a T2 curve which is the average of 5 repeat measurements (black curve), along with 2 examples of the underlying measurements which contribute to this plot (dotted curves). Although the averaged curve appears smooth, the noise in the measurement result in some significant fluctuations in the underlying individual curves. Due to the random nature of the fluctuations, increasing the number of measurements N did not reliably result in an improvement in the SNR, as the noise did not scale with $\sqrt{N}$. The bar chart shown in Figure 3.14 is the result of a study conducted on 12 healthy participants (mean age 28.7, 9 males) and shows the effect of this instability on the percentage error on the T2 values obtained using the regional SL-TRUST method.

The errors on T2 are found to be in the region of 12-15% for regional SL-TRUST methods, in comparison to less than 5% error in global TRUST T2 measurements.

The following sections outline two methods that were explored to tackle this signal instability and improve the T2 measurement precision. These methods addressed the hypotheses that these fluctuations were due to either pulsatile flow in the sagittal sinus or due to partial volume contributions from surrounding static tissue.

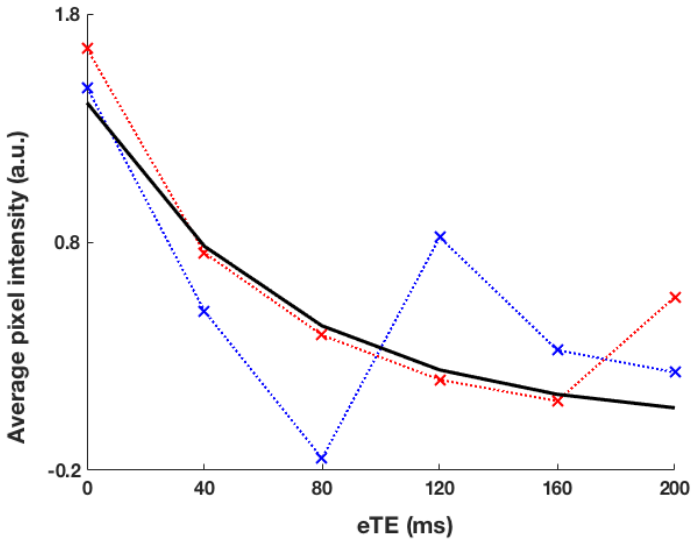


Figure 3.13 Average T2 curve (black) with underlying curves with significant signal instability (blue and red) for regional SL-TRUST

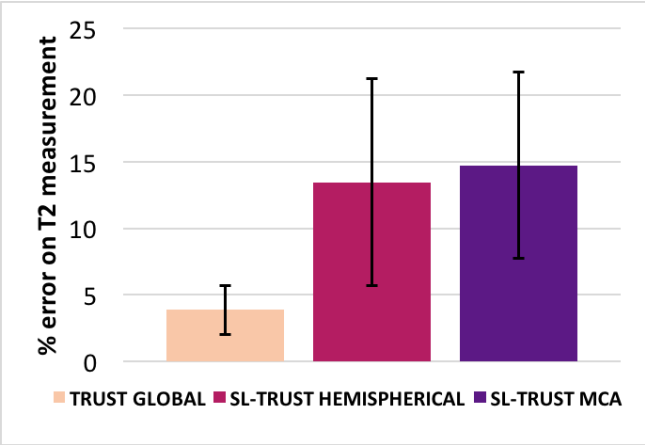
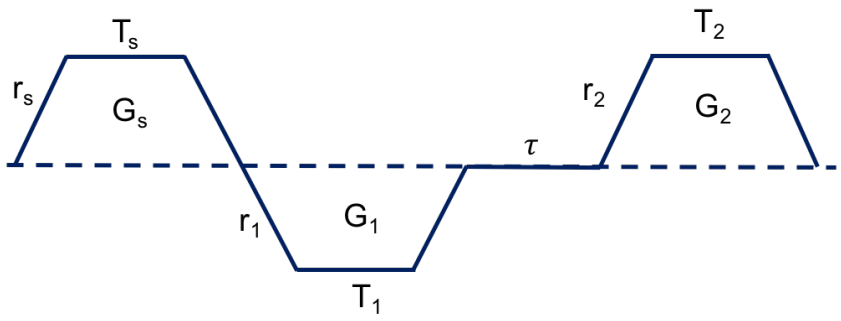


Figure 3.14 TRUST vs SL-TRUST percentage error (N = 12). The precision on TRUST T2 measurements is below 5% however for regional SL-TRUST measurements this increases to over 10%. This instability is on the same scale as any physiological changes which the method aims to detect.

3.6.1 Flow-compensated readout

As described in 2.5.4 flow-compensated readout methods can be used to mitigate the effects of moving spins accumulating a phase shift due experiencing varying gradient strengths in comparison to static spins.

In order to improve the spin coherence within the ROI in the sagittal sinus an additional gradient lobe G_1 was inserted into the readout module, such as the one shown in Chapter 2, operating in the slice-selective plane (the primary direction of blood motion). For ease, the figure is shown again here below.



Following the equations of Bernstein, King and Zhou an empirical solution for Lobe 1 is calculated, based on the following lobe parameters: $T_s = 1280\,us, r_s = 60\,us, A_s = 9.54\,mT/m$, $T2 = 450\,us, r_2 = 130\,us\,, A_2 = 21.55\,mT/m$. Thus $T_1 = 650\,us$, $r_1 = 190\,us$, $A_1 = -29.78\,mT/m$ and $\tau = 330\,us$. Inserting this extra lobe comes at a cost of lengthening the readout TE from 22 ms to 25 ms.

This new flow compensated readout was tested on 2 subjects and the change in noise in the T2 decay curves with and without a flow compensated readout was measured. Ten repeat measurements for both scans were obtained and thus the variation in T2 could be measured, along with the signal fluctuations at each eTE, and the fit of the T2 decay curve evaluated. It was found that using the flow-compensated readout did not improve any of these precision parameters. Figure 3.15 shows no significant reduction in the standard deviation at each eTE, indeed in some cases the error bars are larger than in the case of no flow-compensated readout. The average residuals on the fit were not improved, instead the residuals on the T2 curves shown in Figure 3.15 are 6% larger when using a flow compensated readout than without. A modest but insignificant reduction in the standard deviation across 10 repeat measurements for T2 is observed when using a flow-compensated readout, from 12.83 ms to 11.83 ms.

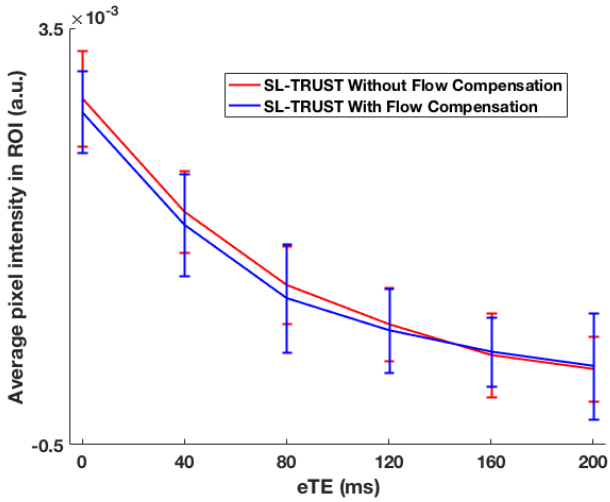


Figure 3.15 Effect of flow-compensated readout on the SL-TRUST T2 error bars.

There are several reasons why this may not have been effective. Firstly, lengthening the already long TE of 22 ms may exaggerate any dephasing effects, and also result in some signal loss due to T2 decay. It was assumed the spins are moving at uniform speed which may not be valid for highly pulsatile flow, whereby the blood alternates between being relatively stationary or slow moving, to accelerating through the vessel, this is similar to turbulent flow which cannot be fully corrected using flow compensation (46).

3.6.2 Background suppression

As explored in Chapter 2 background suppression is often utilized in MR sequences that have inherently low SNR or large background signals which may swamp the measured signal, for example in spectroscopy (large water peak) or ASL (static tissue signal).

Whilst pairwise subtraction of the tag and control images serves to eliminate the background signal from static brain tissue, the underlying noise in the SL-TRUST T2 curves do not follow the same scaling pattern observed for TRUST. Namely that in TRUST, at longer eTEs and as the signal magnitude decreases, so does the noise magnitude. In comparison, for SL-TRUST the noise appears constant. An example is shown in Figure 3.16.

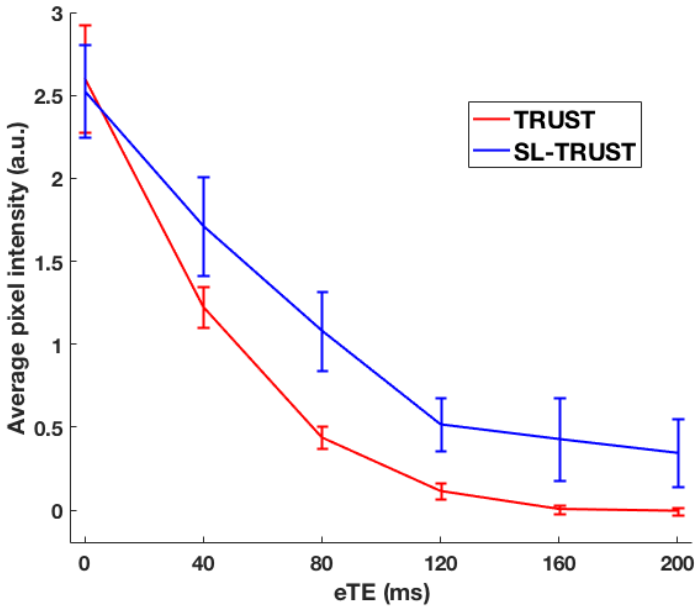


Figure 3.16 Scaling of error bars in TRUST vs SL-TRUST demonstrate how the residuals scale with eTE for TRUST but not for SL-TRUST. The residuals represent the variance at each eTE across multiple repeated measurements.

The hypothesis for this difference is that it stems from one of the key modifications made to the TRUST sequence, namely moving the T2-encoding module from immediately prior to the readout, to before the inversion. In TRUST this T2-encoding module acts as a suppression method, not only on the venous blood signal but the surrounding static

tissue is also attenuated. Therefore, at the time of readout for long effective echo times, the static tissue has been suppressed. In contrast, in SL-TRUST, the static tissue may partially or fully recover its magnetisation over the TI period, thus contributing relatively large signal at the time of readout. Even minimal errors in the pairwise subtraction may lead to relatively large signal contribution from background tissue. To test and correct for this, background suppression pulses were inserted with the aim of suppressing static tissue T1 at the time of the readout.

The multiple inversion recovery (MIR) suppression approach utilized here is based on the ASSIST technique mentioned in Chapter 2 which was developed for noise reduction in 3D perfusion imaging ASL MRI.

These two background suppression pulses are inserted in between the WET saturation scheme and the readout. Assuming brain tissue T1 ~ 1400 ms and T2 ~ 100 ms, a Bloch equation simulation was used to simulate the suppression of tissue at TI = 1200 ms for $T1_{opt}$ = 100-1000 ms in increments of 100 ms. This was compared to experimental data obtained in a healthy control. The results are shown in Figure 3.17. Thus a $T1_{opt}$ = 700 ms was used for SL-TRUST.

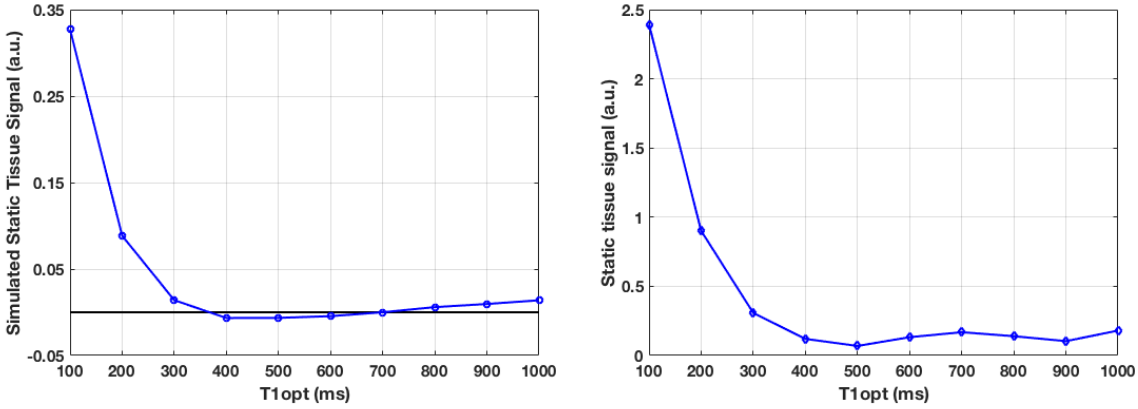


Figure 3.17 Simulation (LEFT) and experimental data (RIGHT) of the longitudinal magnetisation at TI = 1200 ms for a range of $T1_{opt}$ values.

To assess the improvement on the T2 measurement precision achieved using background suppression, a comparison the two versions of SL-TRUST (with and without background suppression) was performed in 4 healthy subjects (mean age 30.8 yrs, 2 males). The results of which are shown in Figure 3.18. The percentage error on T2 for SL-TRUST improves from 11.91% to 6.65%. The magnitude of background signal from static tissue was found to be reduced by 96.1 ± 0.6%, averaged across subjects.

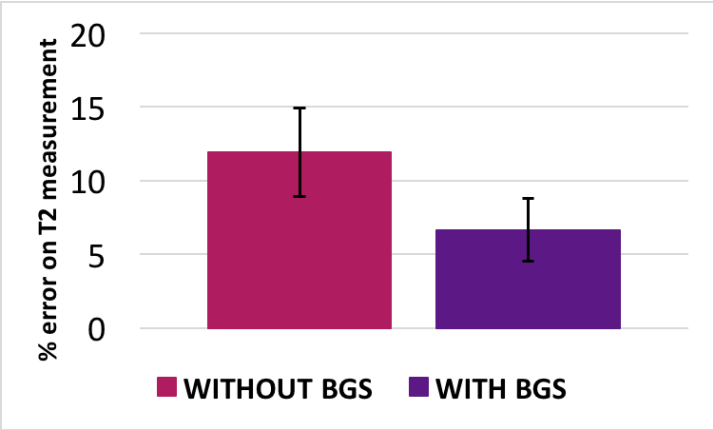


Figure 3.18 Percentage error on SL-TRUST T2 without and with background suppression (BGS) (N = 4, mean age 30.8 yrs, 2M)

Following the insertion of background suppression pulses the experiment to test the dependence of the T2 measurement on the sequence repetition time TR was repeated. The results have been shown previously in Table 3.1 in 3.4.2 and show further evidence of the variance across multiple measurements of T2 being reduced using background suppression. Importantly, for the T2 values given in Table 3.1 the use of background suppression means the OEF values now lie in the more realistic range of 30-45%, rather than 10-20%.

3.7 Post processing

With each step of the acquisition sequence optimized, this section describes the post-processing steps which transform the images acquired using SL-TRUST to measurements of venous blood T2.

Pairwise subtraction of tag-control image pairs yields a difference image such as those previously shown in Figure 3.1 for TRUST. The ROI around the sagittal sinus is identified manually, using the highest contrast image eTE = 0s. The signal in 4 voxels is averaged and a plot of signal intensity in the sagittal sinus is plotted for each eTE. A mono-exponential fit given by Equation 3.2 is applied to the resulting curve to give the decay time constant of the curve, and thus T2.

As outlined previously, the regional SL-TRUST method suffered from poor SNR in comparison to TRUST, due to the smaller volumes from which signal is ultimately derived. Signal instability results in unreliable T2 values and large errors, well outside the desired precision for the technique. In addition to the careful consideration of the acquisition methods which have been outlined previously, a number of post processing steps with the aim of maximising available SNR and minimising the effects of motion were explored.

3.7.1 Motion correction

Previous work in TRUST has demonstrated that whilst it is considered a robust method, in the presence of motion the T2 values can fluctuate by approximately 7-10 ms (83). This bias is almost half of the physiological change most studies try to detect in disease.

The first step of motion correction was always to inspect the images manually to see if any visible motion had occurred. If motion occurred between measurements, the ROI over the sagittal sinus was changed appropriately. The ROI **within** measurements was kept constant.

Correction of motion effects within measurements (if any) was attempted using the MCFLIRT tool in FSL (84). MCFLIRT is an intra-modal correction tool, originally designed for application in fMRI time series data. The method uses a series of cost-functions at increasingly fine resolutions to register a time series to a template image, typically one chosen in the middle of the time series. For the purpose of SL-TRUST an additional parameter was used in the correction to account for the varying contrast between images.

MCFLIRT motion correction parameters showed motion correction of approximately 0.3 mm across image groups within scans. However, interpolation and smoothing algorithms contained within MCFLIRT resulted in blurring of tissue signal into the region of interest containing the blood vessel. Personal correspondence with, and advice from, FSL developers indicated that 2D motion correction is challenging for images with multiple saturation bands and under such small motion effects. With the added risk of inducing partial volume effects, the cost of motion correction outweighed the benefits in healthy controls.

3.7.2 Adaptive combine coil reconstruction

The final aspect of the post-processing pipeline to be discussed (although it is the first to be applied) is the coil combination and image reconstruction.

Due to the highly localized origin of the signal, and proximity to a small number of coils, the hypothesis was that the SNR could be improved using a custom reconstruction technique that focused on the posterior coils. The adaptive combine technique based on

the work of Walsh et al. described in 2.4.2 was implemented, first in a phantom and then in all subsequent human data (37). This approach assigns weightings of each coil contribution across the image and thus down weights noise contributions from those coils furthest from the ROI.

The adaptive combine method was implemented using the average of the first two image measurements (tag and control for eTE = 0ms) as the data with which to estimate the coil sensitivities. The SNR was computed using the mean pixel intensity in an ROI of a single image, and the standard deviation in the same ROI of an image which was the subtraction of two images acquired with identical scan parameters. The image SNR is calculated using $SNR = S\sqrt{2}/\sigma$, where the $\sqrt{2}$ arises due to the noise being derived from the subtraction of two images (85). Figure 3.19 shows the signal and noise contributions in a phantom as more coils are added to the reconstruction, and compares adaptive combine to the standard sum of squares approach. This was calculated using an ROI in the phantom which would correspond roughly to the position of the superior sagittal sinus in a subject. Using only a small number of coils there is less signal using the adaptive combine method but there is also less noise. Coils 20-22 are those closest to the ROI (the back of the head/phantom) and thus there is a sudden increase in signal when those coils are included. As more coils are included the noise in the sum of squares reconstructed images continues to increase whilst it remains constant or decreases for the adaptive combine method. Overall the adaptive combine method gave a 23-fold increase in SNR compared to the standard sum of squares approach.

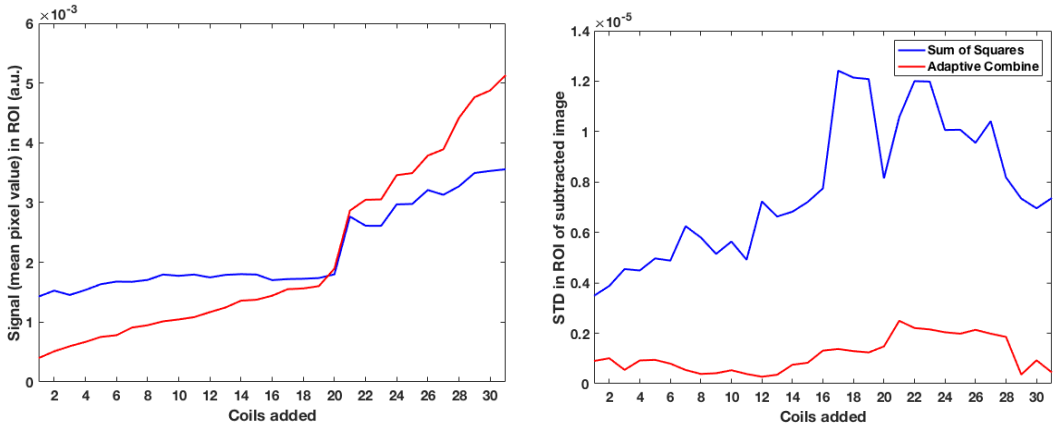


Figure 3.19 How the signal (left) and standard deviation (noise) (right) in the sagittal sinus ROI evolve as more coils are added for both sum of squares and adaptive combine methods. Coils 20-22 are those closest to the ROI therefore contribute large amounts of signal.

3.8 Discussion

Summary of key findings:

- A new MR sequence for measuring regional T2 values in the brain is developed for implementation at 3T.
- WET saturation scheme allows regional localization of venous blood signal. For hemispherical saturation the venous blood signal is reduced by 64.5 ± 15.4%.
- Background suppression compensates the static tissue recovery that occurs in SL-TRUST due to moving the T2-encoding module from immediately before the readout.
- Using a $T1_{opt}$ = 700 ms the signal from static tissue is reduced by 96.1±0.6% and a 6.65% percentage error across multiple repeat measurements of T2 using regional SL-TRUST is achieved.
- Adaptive combine reconstruction of all 32 coils improves the image SNR 23-fold in comparison to root sum-of-squares.
- The recommended TI and TR times for SL-TRUST are found to be 1200 ms and 4 s respectively.

In this chapter the composite pieces of a novel sequence, Selective Localised TRUST, based on the MR sequence TRUST, are outlined. These modifications enable the signal from spatially encoded blood spins in the brain vasculature to be subsequently decoded in the superior sagittal sinus draining vein and spatially localised measurements of venous blood T2 are obtained. Each component in the sequence has been optimized and tested with the aim of ensuring measurements of venous blood T2 using SL-TRUST are robust

and accurate. Example T2 decay curves for the final SL-TRUST method, are shown in Figure 3.20.

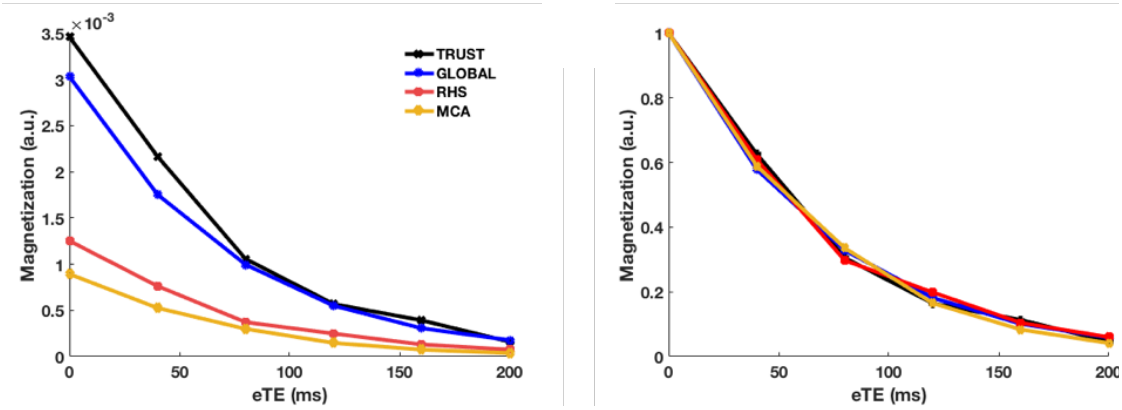


Figure 3.20 LEFT: Example T2-decay curves using the final developed protocol for SL-TRUST, in a single subject from a single measurement. Both regional (RHS & MCA) and global SL-TRUST are shown, as well as the original TRUST for comparison. The drop in signal intensity as a result of WET saturation in the regional method is indicative of how much signal is removed in each case. RIGHT: Normalised curves showing a well matched T2 value across the whole brain for this subject.

The full outline of the sequence is as follows: An MLEV-4 T2-encoding module, with an inter-echo spacing of 10 ms, applies a T2-weighting with multiples of 40 ms to both tissue and blood spins. A tag inversion pulse covering a brain slab is followed by a 5 mm EPI readout slice, placed 20 mm below the tagging plane, with a 1200 ms inversion time (TI) separating the two. During this inversion time one or two sets of 4 cosine modulated RF pulses with varying flip angles (88.9°, 98.7°, 82.5°, and 159°) at 10 ms intervals are inserted to achieve a spatially selective WET saturation. Following WET saturation, two inversion pulses null the background static tissue at the time of the readout. The sequence

is repeated with a repetition time (TR) of 4 s, for six effective Echo Times (0, 40, 80, 120, 160, 200 ms).

Reconstruction of images obtained using SL-TRUST is performed using an adaptive combine reconstruction method to improve SNR, however this is not a requirement. The ROI is identified manually. There is scope here for an automated approach of identifying the ROI. With an image resolution of 64x64 there were typically 4 sagittal sinus blood voxels, the average pixel signal intensity of which formed the point on the T2-decay curve for a specified eTE. Previous work by Lu et al. 2008 found that varying the number of voxels used in the ROI had no effect on the resulting T2 measurement (8).

No motion correction is employed and flow correction was not found to influence the measurement. If desired, one possible solution to the difficulties of post-processing motion correction of these images in 2D is the addition of prospective motion navigators. The SL-TRUST sequence lends itself well to the inclusion of motion navigators due to the ample dead time, and indeed this was investigated by Stout et al. for the TRUST sequence (83). In that study, a volume navigator was included during the inversion time and used as a retrospective motion correction tool.

No work was conducted to reduce the readout TE of the acquisition although this has been shown to improve measurement precision in previous TRUST literature. Lu et al. shortened the echo time TE to as low as 3.6 ms using partial-Fourier acquisition, thus improving the signal stability (80).

A small study in 4 healthy subjects found that across repeat measurements within the same scan session the variance in T2 for regional SL-TRUST was comparable to those

obtained using TRUST. This was primarily achieved by inserting background suppression pulses to remove signal from the static tissue in the image slice. The variance of regional SL-TRUST T2 measurements is investigated in more detail in the following chapter.

Chapter 4 Spatially localized measures of oxygen extraction fraction using Selective Localized TRUST

4.1 Introduction

This chapter presents the findings from a cohort study of N = 6 healthy participants, demonstrating the reliability of the T2 measurements acquired using SL-TRUST. Reproducibility of regional SL-TRUST is compared to global TRUST, both within and across scan sessions, and subjects. The study includes a measure of venous blood T1 in order to estimate subject-specific haematocrit values, and thus translate the T2 measurements into those of cerebral OEF. The results of this study were previously published as O'Brien C, Okell TW, Chiew M, Jezzard P. Volume-localized measurement of oxygen extraction fraction in the brain using MRI. *Magn Reson Med* . 2019; 82(4): 1412–1423.

Finally, findings from initial tests of SL-TRUST in a stroke population are presented (N = 2). These were acquired with the help of radiographers A. Fletcher and P. Manley, and clinicians J. Garrard and J. Kennedy.

4.2 Measuring venous blood haematocrit using MRI

Conversion of venous blood T2 values to OEF is achieved using the model described in 2.7.2, for ease repeated here below:

$$\frac{1}{T2} = A + B \cdot (1 - Y) + C \cdot (1 - Y)^2$$

$$A = a_1 + a_2 \cdot hct + a_3 \cdot hct^2$$

$$B = b_1 \cdot hct + b_2 \cdot hct^2$$

$$C = c_1 \cdot hct \cdot (1 - hct)$$

Where a_1 = -13.5, a_2 = 80.2, a_3 = -75.9, b_1 = -0.5, b_2 = 3.4 and c_1 = 247.4 (s^{-1}), derived from experimental work by Lu et al. for τ_{CPMG} = 10 ms (67). The parameters A,B, and C are also dependent on the haematocrit (hct). Often, the haematocrit is assumed to be uniform across all subjects (40-54% for men and 37-47% for women (86)), however this assumption may not be valid in patient populations where haematocrit fluctuates or is abnormal. As demonstrated in Figure 4.1, for a given T2 there can be a range of venous blood oxygenation levels depending on the haematocrit. For T2 = 68 ms there is a 4% variation in OEF over a physiologically normal range of hct = 0.38-0.46.

In clinical populations haematocrit can be determined via a blood sample. As the aim of this work is to develop a completely non-invasive method of measuring OEF, and due to restrictions on the ethics of the study no blood samples were taken. Instead, this study exploits the linear relationship between the longitudinal relaxation rate R1 and the blood haematocrit. This is due to the fast exchange regime of water protons between the blood cell and plasma compartments of the blood (87).

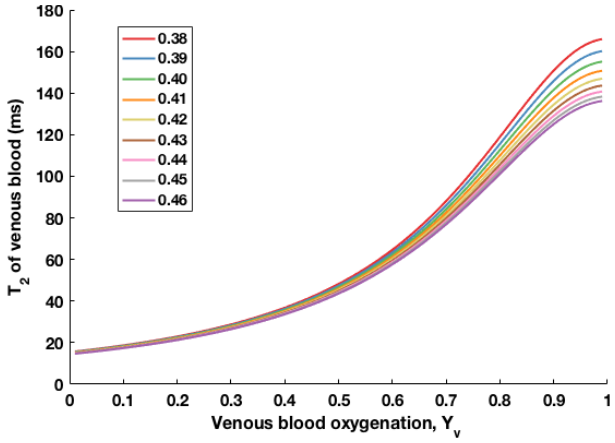


Figure 4.1 Relationship between venous blood oxygenation and venous blood T2 for a range of haematocrit values for τ_{CPMG} = 10ms.

Before continuing, it must be acknowledged that the relationship between the four parameters: venous blood T2, T1, and blood haematocrit hct and oxygenation Y_v is complex, and a level of dependency exists between them all. It is well known however that the relationship between T2 and oxygenation is stronger than between T1 and oxygenation. Therefore this work, like many others, assumes that blood T1 is independent of blood oxygenation (88). This same assumption was made by J.B. De Vis et al. in their study estimating T1 using haematocrit in neonates, who also showed the relatively small change in T1 for changes in Y_v within the physiologically expected range (0.6-0.7) (87). It is for this reason that studies often neglect subject specific haematocrit values from their estimation of Y_v. Indeed when looking at relative values of OEF, as is often the case, haematocrit can be assumed to be uniform unless there is a specific condition or reason why it may be different. For absolute values of OEF, haematocrit is required.

There is an increasing amount of literature which aims to measure blood T1 and thus derive this relationship to blood haematocrit especially under conditions where

haematocrit is known to vary, such as in neonates. The majority of these studies, however, focus on measurements in large veins or arteries, such as the internal jugular vein, and few have attempted it in the superior sagittal sinus (89,90). Additionally, these are all derived using different MR acquisition methods, experimental conditions, and in different population groups.

A summary of just some of these models, all performed at 3 Tesla, is given in Table 4.1 (87,90-92). The table demonstrates the subtle differences in the coefficients found by each study, all of which follow the same linear relationship.

Table 4.1 Summary of studies determining the linear relationship $\frac{1}{T1} = a \cdot hct + b$

Model	**Study Details**	**a**	**b**
Varela, 2011	Neonates	0.5	0.37
Lu, 2004	In vitro bovine blood	0.83	0.28
JB De Vis, 2014	Neonates	0.25	0.46
Shimada, 2012	Healthy Male Adults	0.7	0.27

Shimada's model, given in full in Equation 4.1 is the model chosen for this study, since the measurements were in a human adult population most similar to those used in this study and were also conducted *in vivo*.

$$\frac{1}{T_1} = (0.7 \pm 0.11) \cdot hct + (0.27 \pm 0.05)$$

Equation 4.1

The acquisition protocol in the Shimada study used an inversion recovery (IR)-prepared fast low-angle shot gradient-echo sequence and a 20 mm readout slice through the internal jugular vein (90). The nonselective IR pulse was applied to the head and neck region using a body coil and the relationship found using a weighted linear regression model with the variance in the haematocrit values as the weighting.

4.2.1 Measuring T1

A number of sophisticated approaches for measuring T1 in fast flowing blood exist, for example using a Look-locker approach whereby multiple small-flip-angle excitation pulses achieve a full T1 measurement in a single TR. This can be utilized without the need for correction due to using multiple excitation pulses, so long as the time between pulses is longer than the time for blood to be refreshed in the readout slice (89). This has even been applied in the superior sagittal sinus for measurement of T1 of venous blood in both adults and children in a sequence called Inversion Recovery(IR)-TrueFISP, and achieved scan times of under 1 minute (93). In general, previous results have demonstrated that *in vitro* measurements are approximately 200 ms shorter than those measured *in vivo* (88,89,94).

Since the primary objective of this thesis is developing a robust method of measuring T2, and without access to the IR-TrueFISP sequence described above, a relatively simple inversion recovery sequence is implemented here, utilizing an on/off-resonance global

inversion pulse such as the tag inversion used in the SL-TRUST sequence, in order to perform pairwise subtraction and reduce partial volume effects. Slice-selective background suppression pulses, similar to those described in 3.6.2, are inserted to saturate the static tissue signal. The background suppression pulses are only inserted once the time elapsed between the second background suppression inversion pulse, and the readout is sufficient for the blood in the readout slice to have been replenished. Assuming the velocity of blood in the superior sagittal sinus to be approximately 13 cm/s, and a 10 mm slice this equates approximately to 100 ms.

For the multi-TI measurement of T1, an initial TI = 100 ms was used, with ΔTI = 550 ms, TR = 10 s, slice thickness = 10 mm, 9 increments, and 2 averages. The total scan time per T1 measurement was approximately 4 minutes.

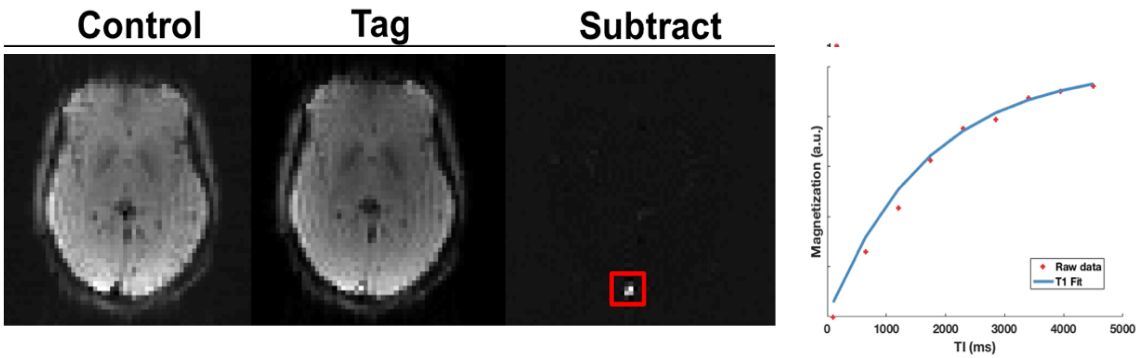


Figure 4.2 Example images and resulting inversion recovery curve for T1 measurement (without background suppression applied)

4.3 SL-TRUST reproducibility study

Table 4.2 shows the reproducibility coefficients that have been demonstrated in current literature for whole brain TRUST measurements of OEF.

Table 4.2 Coefficients of Variation of OEF for TRUST Liu et al. 2013

N = 7	(Mean ± SD %)
Intrasession	3.19 ± 1.20
Intersession	8.16 ± 4.46
Intersubject	15.61

The aim of the study was to demonstrate comparable reproducibility for both global and regionally-specific T2 and OEF measurements acquired using SL-TRUST. The robustness and reproducibility of SL-TRUST was assessed in whole brain as well as in a single hemisphere, and in 70x70x80 mm^3 MCA-territory tissue regions in 6 subjects across 4 repeat scan sessions. Repeat measurements were also acquired within each scan session. This allows the inter- and intra-scan Coefficient of Variation to be calculated for each measurement, along with inter-subject variability. An additional venous blood T1 measurement, also in the sagittal sinus, was included to estimate subject-specific haematocrit levels, rather than assuming uniform haematocrit across all subjects.

A Bland-Altman plot analysis was performed to assess the agreement between global measures obtained using TRUST, and global and regional ones measured using SL-TRUST.

4.3.1 Data collection

Reproducibility data were acquired in 6 healthy volunteers (mean age 29.2 years, 3 males) under a technical development protocol approved by the local ethics committee. All experiments were performed on a 3 Tesla [T], Siemens Verio scanner (Siemens Healthineers, Erlangen, Germany), with a 32-channel head receive coil and body transmit. Each participant underwent 4 separate scan sessions over the course of two weeks to assess the method reproducibility. The scan protocol for each session included a whole-brain (global) conventional TRUST measurement, a global SL-TRUST measurement, a hemispherical SL-TRUST measurement, and a SL-TRUST measurement prescribed over a 70x70x80 mm^3 tissue region located in the middle cerebral artery territory. The order of scans in the protocol was randomized to avoid time-dependent bias due to participant fatigue. In total this protocol of measurements took approximately 9 minutes. During the initial scan session the protocol was repeated an additional two times, once without repositioning of the subject, and once after removing and repositioning the subject within the scanner. In each of the three follow up scan sessions the protocol was repeated one additional time, without repositioning of the subject. During one of the four scan sessions, an additional venous blood T1 measurement was acquired using the multi-inversion recovery sequence described above. Three T1 measurements were acquired during the scan, an initial T1 measurement (later used to estimate subject-specific haematocrit), and two follow up measurements with and without repositioning of the subject, in order to calculate the inter and intra scan coefficients of variability in T1. In all cases the readout slice was angled to be parallel to the anterior commissure - posterior commissure line.

Only one subject did not complete all of the 4 scan sessions within a two week period. For this subject only three complete scans were acquired and used in subsequent analyses. Additionally, only a single T1 measurement was obtained for this subject. Therefore the inter-subject CoV for T1 is only calculated across 5 subjects.

4.3.2 Coefficients of Variation

The following metrics were calculated for T2 and T1 to assess reproducibility:

(i) Intra-session coefficient of variation (CoV) (which reflects the measurement noise) was calculated as:

$$CoV_{intra-session} = \frac{1}{I \cdot J} \sum_{i} \sum_{j} \frac{|M_{ij1} - M_{ij2}|}{\sqrt{2} \cdot mean(M_{ij1}, M_{ij2})}$$

Equation 4.2

where M_{ijk} represents measurement $\#k\ (k = 1,2)$ of Subject $\#i\ (i = 1,2,3..I)$ in Session $\#j\ (j = 1,2,3,...J)$.

(ii) Inter-session CoV was calculated as:

$$CoV_{inter-session} = \frac{1}{I \cdot K} \sum_{i} \sum_{k} \frac{SD_j(M_{ijk})}{mean_j(M_{ijk})}$$

Equation 4.3

where $mean_j$ and SD_j are mean and standard deviation across sessions, respectively.

(iii) Finally, the inter-subject CoV was calculated as:

$$CoV_{inter-subject} = \frac{1}{J \cdot K} \sum_{j} \sum_{k} \frac{SD_i(M_{ijk})}{mean_i(M_{ijk})}$$

Equation 4.4

Subject repositioning and day-to-day physiology differences are contained within the inter-session CoV. These contributions can be estimated using $\sqrt{CoV^2_{inter-session} - CoV^2_{intra-session}}$. Similarly, inter-subject CoV contains physiological differences between subjects, which can be considerable. These can be estimated using $\sqrt{CoV^2_{inter-subject} - CoV^2_{inter-session}}$ (77).

4.3.3 T2 and OEF for TRUST and SL-TRUST using uniform haematocrit

Table 4.4 shows the T2 and OEF measurements (from a single scan session) for both TRUST and each SL-TRUST measurement (one global and two regionally specific), using uniform haematocrit for male and female subjects. Using a uniform haematocrit the average T2 in the sagittal sinus was found to be 63.2 ± 9.6 ms, 65.3± 8.8 ms, and 68.3 ± 10.2 ms (mean ± SD) for TRUST, global SL-TRUST, and regional SL-TRUST, respectively. Figure 4.3 shows the average and standard deviation of the T2 measurement for each scan type and for each subject, taken across all scan sessions. Inter-subject differences can be observed across all techniques with some participants showing consistently higher (or lower) T2 values.

Bland Altman plots comparing TRUST and SL-TRUST T2 values in Figure 4.4 show that there is a slight systematic bias between TRUST and regional SL-TRUST T2 measurements. The largest deviation in the mean difference is approximately 5 ms, and the 95% confidence intervals do not contain zero mean difference which indicates an overall significant difference between the two measurements.

Using a uniform haematocrit of 0.4 and 0.43 for female and male participants respectively, the average OEF was found to be 40.5 $\pm$ 5.2%, 37.8 $\pm$ 4.6%, 36.9 $\pm$ 4.8%, and 36.1 $\pm$ 5.8% for TRUST, global SL-TRUST, and hemispheric SL-TRUST and 3D-localized SL-TRUST respectively (averaging across all subjects and all scans).

Table 4.3 shows the intra- and inter-session, and inter-subject coefficients of variation for both T2 and OEF for TRUST and SL-TRUST. Overall, good agreement was found between the reproducibility of OEF measurements using TRUST and SL-TRUST in this study and those from a previous TRUST reproducibility study by Liu et al. previously shown in Table 4.2.

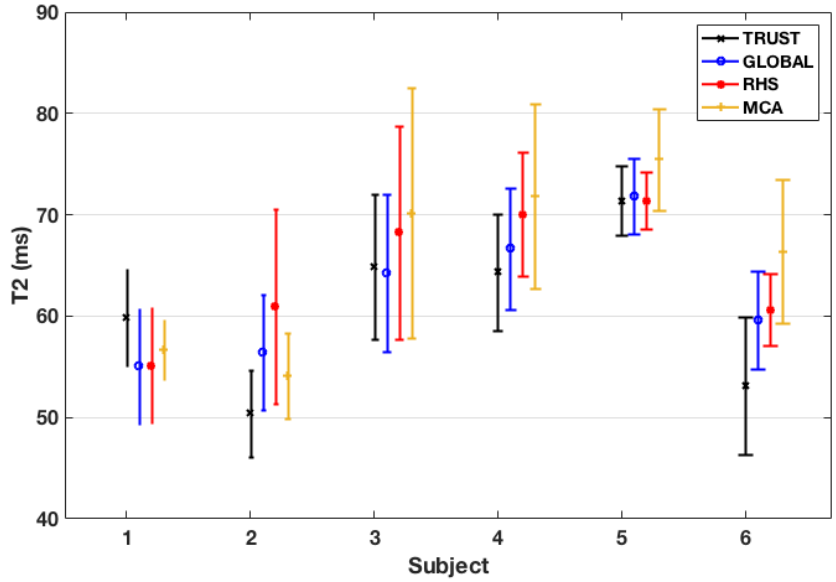


Figure 4.3 Average and standard deviation of T2 values across all scan sessions for each of the six subjects for TRUST and global and regional SL-TRUST.

Table 4.3 Coefficients of Variation for TRUST and SL-TRUST

CoV (%)	**TRUST**		**GLOBAL**		**RHS**		**MCA**	
	T2	**OEF**	**T2**	**OEF**	**T2**	**OEF**	**T2**	**OEF**
Intra-session	4.70	3.87	4.41	3.96	5.71	5.31	4.46	4.50
Inter-session	8.71	7.33	7.80	7.13	8.73	8.17	8.70	8.42
Inter-subject	14.04	12.07	14.38	13.21	14.19	13.88	17.75	16.77

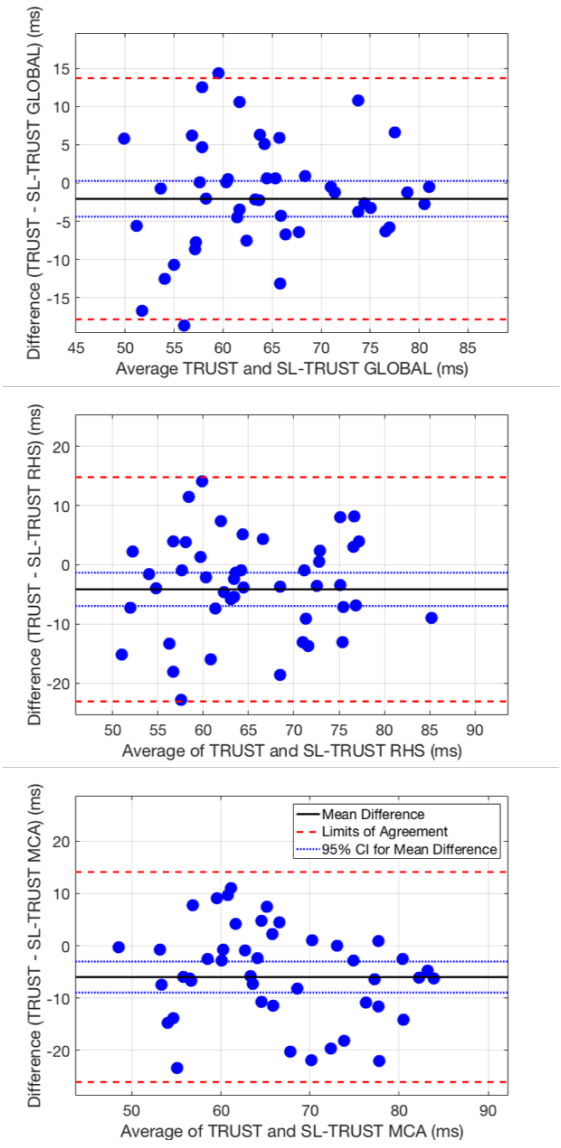


Figure 4.4 Bland-Altman correlation plots for T2-measurements using TRUST vs global (top), hemispherical (middle), and regional (bottom) SL-TRUST. The solid line (black) is the mean difference between the 2 measurements and the dashed lines indicate the 95% confidence interval (blue) and the agreement limit (red). A slight negative bias of around 5 ms is observed between TRUST and SL-TRUST

The intra- and inter-session CoV for global OEF measured using SL-TRUST was found to be 3.96% and 7.13%, which is comparable to those found for TRUST: 3.25% and

6.76% in this study, and 3.19% and 8.16% found by Liu et al. (77). A similar accuracy was found for spatially-localized SL-TRUST measurements, despite the reduced signal. As predicted, the inter-session CoV is larger than the intra-session CoV due to subject repositioning and day-to-day physiological differences. The variation due to these differences was calculated to be on average 5.91% across all methods. The inter-subject CoV on T2 for TRUST and SL-TRUST are all <15% with the exception of SL-TRUST MCA which is slightly higher at 17.75%. These are comparable to the 15.61% inter-subject CoV found by Liu et al. for the original TRUST sequence (77).

Table 4.4 Example T2 measurements and the resulting OEF values calculated using uniform haematocrit values of 0.4 for female subjects and 0.43 for male subjects.

Subject	**hct**	**T2 (ms) (±std)**				**OEF (%)**			
		TRUST	**SL-TRUST**			**TRUST**	**SL-TRUST**		
# (F/M)		GLOBAL	GLOBAL	RHS	MCA	GLOBAL	GLOBAL	RHS	MCA
1 (F)	0.4	64.0 ±1.6	52.3 ± 1.1	70.3 ± 4.3	55.6 ± 7.6	39.0 ± 1.0	45.9 ± 1.0	35.9 ± 2.7	43.8 ± 4.1
2 (F)	0.4	51.1 ± 1.1	47.0 ± 9.6	56.7 ± 4.0	58.7 ± 5.2	46.7 ± 1.1	49.7 ± 10.6	43.1 ± 3.2	42.0 ± 4.0
3 (M)	0.43	61.3 ± 3.8	68.1 ± 3.2	64.6 ± 3.6	59.5 ± 3.6	38.9 ± 2.4	35.4 ± 1.9	37.1 ± 2.3	40.0 ± 2.5
4 (M)	0.43	65.9 ± 3.6	62.8 ± 0.9	64.5 ± 1.3	64.3 ± 4.2	36.4 ± 2.1	38.1 ± 0.6	37.2 ± 0.8	37.3 ± 2.6
5 (F)	0.4	70.8 ± 3.6	79.9 ± 2.2	71.6 ± 3.7	80.4 ± 2.2	35.7 ± 2.0	31.7 ± 1.0	35.3 ± 2.0	31.5 ± 1.0
6 (M)	0.43	58.2 ± 1.0	60.2 ± 3.1	59.1 ± 2.4	66.2 ± 1.1	40.7 ± 0.7	39.6 ± 2.2	40.2 ± 1.8	36.3 ± 0.7

4.3.4 T2 and OEF for TRUST and SL-TRUST using subject-specific haematocrit

The T2-OEF conversion of the T2 values shown above was repeated using the subject-specific haematocrit calculated from venous blood T1 measurements in the sagittal sinus. For clarity and comparison, all of the tables below include the original T2 values, which are identical to those presented above. All new results not previously presented are highlighted in bold. The average subject T1 = 1892.6 ± 214.8 gave an average haematocrit of 0.38 ± 0.09 using the Shimada model (90) (6 subjects, mean age 29.2 yrs, 3 males), the full distribution of values are shown in Table 4.6. Although there is insufficient data to determine this statistically, no systematic difference between T1 values in males and females is observed.

The T1 values are in some cases slightly longer than expected and as a result, two of the haematocrit values are outside the expected physiological range (< 0.3). In these cases, the OEF values are consequently higher than expected (>50%) which is driven by these lower haematocrit values. Averaging across all subjects and all scans the average OEF was found to be 45.3 ± 9.0, 42.8 ± 7.4, 41.8 ± 7.6 and 41.1 ± 8.1 % for TRUST, global SL-TRUST, hemispherical, and 3D localized SL-TRUST respectively.

The changes in intra- and inter- session CoV is marginal, in the range of 0.5%, from Table 4.3. Table 4.5 shows the inter-subject coefficients of variation for OEF for TRUST and SL-TRUST obtained using subject-specific haematocrit in comparison to those using

uniform haematocrit values. These are found to be on average around 6% higher. This is due to the additional variance introduced by the subject-specific haematocrit measurement obtained from T1. The additional variance due to inter-subject physiological differences is calculated to be 19.66%. The intra- and inter-session CoV for T1 is calculated to be 2.54% and 4.71%, respectively and the intra-subject CoV for T1 is 15.8%.

Table 4.5 Comparison of Inter-subject CoV for uniform and subject specific haematocrit

OEF	**Inter-subject CoV (%)**	
	Uniform hct	**Subject Specific hct**
TRUST	12.07	**20.96**
GLOBAL	13.21	**20.28**
RHS	13.88	**21.11**
MCA	16.77	**20.30**

4.3.5 Sensitivity to changes in OEF

In one subject (Participant 3) the T2 was observed to fluctuate between consecutive scan sessions and a similar change was detected across TRUST and all SL-TRUST measurements, see Figure 4.5. In this subject, an increase of 19.05 ms is observed from

Session 1 to Session 2 using TRUST. This is matched with a corresponding increase of 17.86, 25.02, and 19.82 ms for each of the three SL-TRUST measurements. This corresponds to a 10.56% drop in OEF identified using TRUST and an average 10.0% decrease in OEF identified using SL-TRUST. This is similar in magnitude to the change in oxygenation observed in previous TRUST studies following a caffeine challenge, 7.0 ± 1.8%, which arises due to vasoconstriction effects (8). This may suggest evidence of SL-TRUST maintaining the sensitivity of TRUST to natural variation in T2.

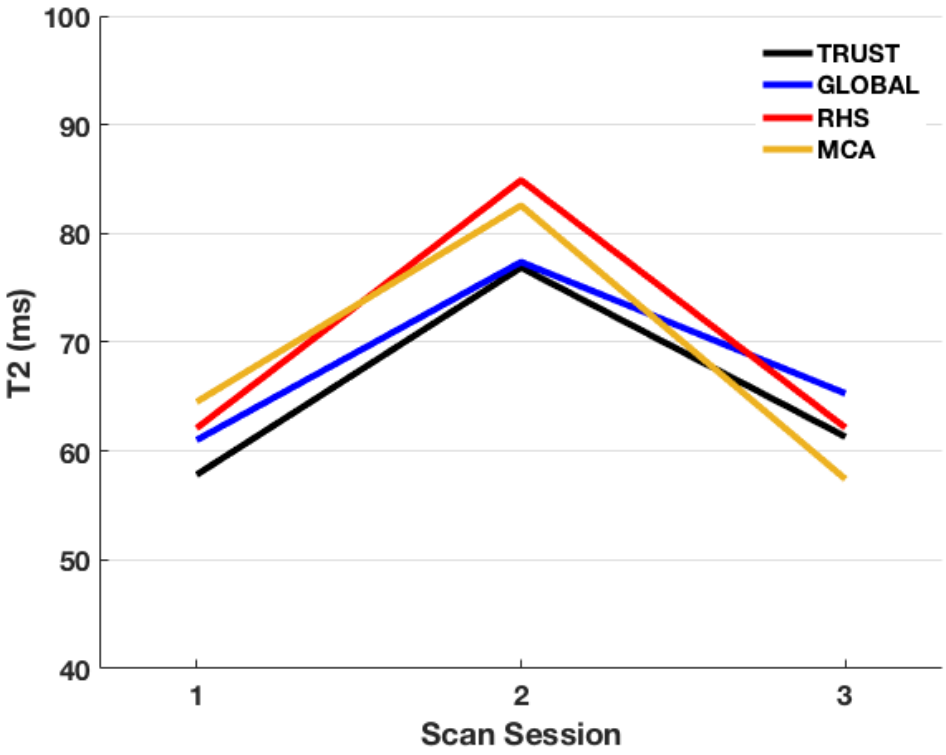


Figure 4.5 Fluctuation in T2 in a single subject over three scan sessions on separate days. The cause of the increase in T2 is not known however it is reassuring to see the same increase across all four measurements.

Table 4.6 Subject-specific T1 and corresponding hct values and the T2 and OEF values for TRUST and whole-brain and regional SL-TRUST measurements (± estimated error).

Subject	**T1 (ms)**	**hct**	**T2 (ms) (±std)**				**OEF (%)**			
			TRUST	**SL-TRUST**			**TRUST**	**SL-TRUST**		
# (F/M)			GLOBAL	GLOBAL	RHS	MCA	GLOBAL	GLOBAL	RHS	MCA
1 (F)	**1715.7 ± 74.4**	**0.447 ± 0.017**	64.0 ±1.6	52.3 ± 1.1	70.3 ± 4.3	55.6 ± 7.6	**36.8 ± 1.4**	**43.8 ± 3.3**	**33.6 ± 2.7**	**41.7 ± 4.4**
2 (F)	**2089.3 ± 95.4**	**0.298 ± 0.014**	51.1 ± 1.1	47.0 ± 9.6	56.7 ± 4.0	58.7 ± 5.2	**55.3 ± 2.7**	**58.2 ± 8.1**	**51.8 ± 2.7**	**50.7 ± 5.3**
3 (M)	**1562.4 ±85.5**	**0.529 ± 0.023**	61.3 ± 3.8	68.1 ± 3.2	64.6 ± 3.6	59.5 ± 3.6	**36.9 ± 1.9**	**33.2 ± 3.0**	**35.0 ± 3.2**	**37.9 ± 3.4**
4 (M)	**1801.4 ± 68.3**	**0.407 ± 0.014**	65.9 ± 3.6	62.8 ± 0.9	64.5 ± 1.3	64.3 ± 4.2	**37.6 ± 1.6**	**39.3 ± 2.7**	**38.4 ± 2.7**	**38.5 ± 2.9**
5 (F)	**2026.0 ± 67.6**	**0.319 ± 0.011**	70.8 ± 3.6	79.9 ± 2.2	71.6 ± 3.7	80.4 ± 2.2	**42.4 ± 1.8**	**38.7 ± 2.7**	**42.0 ± 3.0**	**38.5 ± 2.7**
6 (M)	**2160.6 ± 113.5**	**0.275 ± 0.016**	58.2 ± 1.0	60.2 ± 3.1	59.1 ± 2.4	66.2 ± 1.1	**53.8 ± 3.1**	**52.7 ± 5.8**	**53.3 ± 6.0**	**49.7 ± 5.8**

4.4 Application of SL-TRUST in a stroke population

In February 2019 the SL-TRUST sequence was inserted into the protocol of an ongoing study of ischemic stroke at the Acute Vascular Imaging Centre (AVIC) in the John Radcliffe Hospital in Oxford. As part of the study patients presenting with acute ischemic stroke are scanned within 18 hours of symptom onset, with further imaging performed 24-hours, 1-week, and 1-month after presentation, where possible. All experiments are performed in accordance with the relevant guidelines and regulations[3].

A number of different research scans are included in the protocol, from DWI to vessel-encoded ASL. The SL-TRUST sequence was included at the end of the protocol and acquires two 3D-localised regional measurements in patients, one targeting the area of infarction as identified on a DWI scan, and one located in the contralateral hemisphere, therefore providing a baseline measurement of OEF in presumed healthy tissue for each patient. SL-TRUST was applied only in acute patients (<18-hours after symptom onset and at 24-hours after presentation) as it is thought that during this timescale the OEF is most affected in stroke.

As is often the case with recruitment in acute patient studies, there is little control over the number of patients that come through the study over a particular time scale, and within those that are recruited there are often difficulties acquiring the data. Since February 2019

[3] Patients were recruited and consented under research protocols agreed by the UK National Research Ethics Service Committee South Central – Oxford C (refs: 12/SC/0292 and 13/SC/0362) with informed consent and a clear medical history given by the patient or representative. Patients with a contraindication to MRI, lacunar stroke defined on DWI, or severely impaired conscious level (score greater than 1 on question 1a of the National Institute for Health Stroke Scale) were not enrolled.

when the SL-TRUST sequence was first included in the protocol, until the submission of this thesis in September 2019, only three patients passing through the study have been scanned using SL-TRUST, all males, over the age of 50. Of these, one was discarded due to significant motion during the scan which could not be resolved using MCLFIRT motion correction in FSL (84) .

Of the two remaining subjects subject one had a lacunar stroke, left hemisphere (4357 mm^3), and subject 2 had a posterior circulation stroke, left hemisphere (374 mm^3).

The data acquired from both SL-TRUST scans were processed and analysed via an identical pipeline as those for healthy volunteers shown throughout this thesis. The resulting T2-decay curves for the remaining two subjects are shown in Figure 4.6 **Error! Reference source not found.**.

The T2 values were as follows, Subject 1: 56.0 ms & 57.93 ms, and Subject 2: 56.1 ms & 58.8 ms for the healthy and infarcted tissue areas, respectively. The normalized curves in **Error! Reference source not found.** Figure 4.6 reflect the fact that no discernible difference was found between the two brain regions.

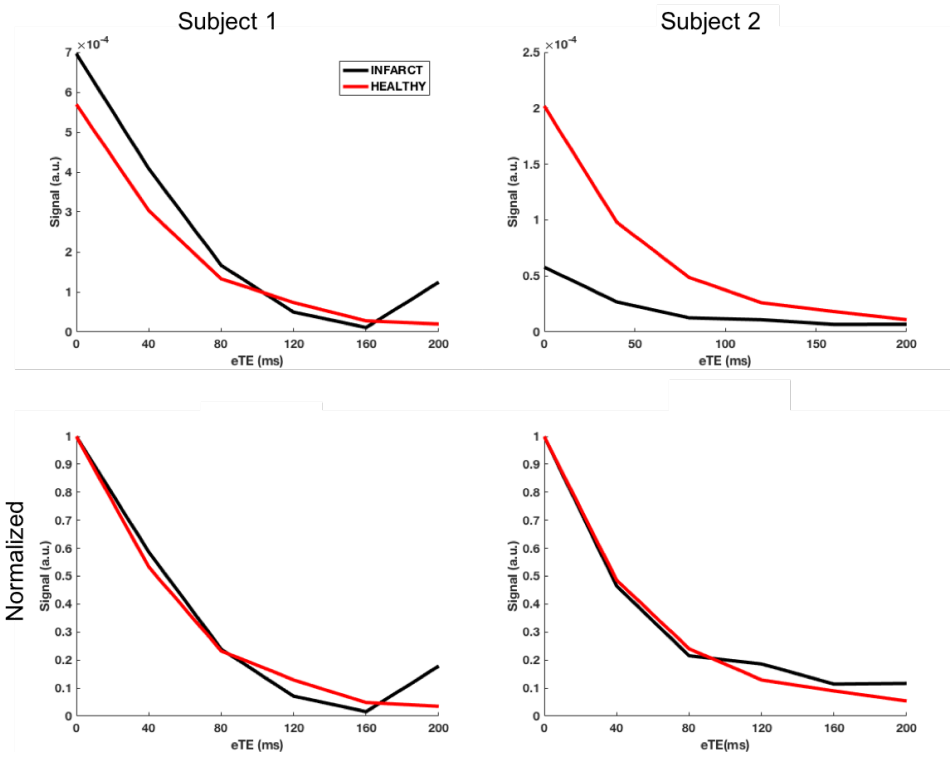


Figure 4.6 T2-decay curves for regional SL-TRUST in two stroke patients. The curves are for the T2 of venous blood spins from regions of infarct (black) and from contralateral healthy tissue. The original curves (top) are shown for comparison of the quantity of signal from each brain area arriving the sagittal sinus at TI = 1200 ms, and the normalized curves (bottom) show whether the T2 (and thus the OEF) from the two regions was well matched or altered due to the stroke.

4.5 Discussion

Summary of key findings:

- A reproducibility study showed that regional SL-TRUST measurements can be obtained with comparable reproducibility values as global TRUST.
- A measure of venous blood T1 gave subject specific haematocrit, a step towards achieving absolute OEF as well as just a relative measure.
- Fluctuations in OEF of up to 10% were observed, with near identical changes across all TRUST and SL-TRUST methods, indicating a retained sensitivity of SL-TRUST to changes in OEF.
- SL-TRUST was successfully applied in a clinical population but no regional OEF differences were observed.

Regional OEF values for both a single hemisphere and a 70x70x80 mm^3 region in the MCA territory of the brain have been obtained with similar precision and reproducibility compared to whole-brain conventional TRUST measurements. This suggests that the dominant source of noise is of physiological origin, and therefore scales correspondingly with the signal for smaller tissue regions. Whilst the global TRUST and SL-TRUST T2 values obtained are not significantly different, there is a significant difference between TRUST and regional SL-TRUST T2 values. This is acceptable given that the blood has originated from a different parts of the brain and may be more sensitive to changes due to activation or fatigue.

The inversion recovery acquisition found the average T1 across subjects to be 1892.6 ± 214.8 ms which corresponded to a haematocrit of 0.38 ± 0.09. Some subjects had hct values outside the physiologically expected range and as a result drove higher OEF values in those subjects. This indicates that the T1 acquisition requires some further thought, however there are already a number of developed sequences available for this task which could be applied here such as a Look-Locker approach for a faster estimation of T1 or performing the measurement in the internal jugular vein (89,93). The advantage of measuring haematocrit in larger veins such as the sagittal sinus and jugular vein is that no small vessel correction is required. In methods such as QUIXOTIC where measurement is in the capillaries, due to the Fahraeus effect a multiplication factor of 0.85 is needed to correct for differences in haematocrit in small vessels (68). Further improvements on the T1 method could also include measuring T1 over multiple days to investigate and account for day-to-day physiological differences.

None the less, the inclusion of an estimate of individual haematocrit values, via a non-invasive blood T1 measurement, would be particularly valuable in diseases or populations where red blood cell count or haemoglobin is expected to be different, and is key in achieving absolute measures of OEF (72,87).

Whilst it is disappointing that no differences in OEF were found between infarcted and healthy tissue in patient data, it was noted that the strokes were very small in the subjects recruited during this period of the study (375 mm^3 & 4357 mm^3). In particular for subject 2 the stroke occurred in the posterior circulatory system and therefore any changes in OEF are unlikely to be captured using this method due to the placement of the ROI.

Nevertheless, there are still some positive points to take away from this study. Firstly, it is valuable to know that viable T2 measurements can be acquired on a clinical population. Research studies restricted to a healthy population do not observe the same degree of motion typically found in patient cohorts, particularly elderly patient cohorts.

Data collection is on-going and there remains hope that differences in OEF will be identifiable in patients with larger strokes. In general, the OEF information provided by SL-TRUST in this study can be combined with information from other scans within the protocol, such as measures of CBF, to provide improved insight into the underlying physiology.

Further work on patient populations, if possible, could focus on establishing the optimal inversion time for SL-TRUST in clinical populations where CBF and inflow time could be altered due to physiology, occlusion, or natural aging.

Chapter 5 Remote reconstruction of SL-TRUST T2 maps using phase encoding

Thus far SL-TRUST has been shown to achieve regional specificity down to a 70×70×80 mm^3 region of tissue, enabling a comparison of two or three different brain regions. What may be more desirable, however, is the ability to produce a venous T2 "map" of the entire brain such that multiple regions can be compared from a single scan without prior knowledge of the tissue region of interest. It would be possible to produce such a map using the current method by performing multiple acquisitions and placing the WET saturation slabs over different brain regions each time, however this approach is not efficient, since the signal in each acquisition only arises from a small region of the brain at a time.

The aim of this chapter, therefore, is to develop a method whereby the spatial origins of venous blood spins over a larger field-of-view can be decoded from the measured signal intensity in the sagittal sinus.

A possible solution is found in the adoption of remote sensing methods, based on work developed originally for gas NMR experiments (95-97). In these methods, spatial information regarding a sample of interest is encoded in a polarized gas which is then

transported to a secondary location for detection and decoding. Despite mixing of the spins in the gas, the underlying spatial information regarding the encoding site within the sample is retained and is able to be reconstructed from the remotely acquired signal.

Successful application of these methods in SL-TRUST could enable the spatial information of blood spins across the entire brain to be encoded whilst in the vasculature, and subsequently decoded in a separate location, the sagittal sinus. If a successful map is produced, this can be combined with the T2 encoding module already used in SL-TRUST, to generate a series of brain maps under different T2-encoding conditions. This would allow the T2 of venous blood spins originating from across different regions of the brain to be calculated.

In this chapter the background and theory of these remote sensing methods is outlined, as well as a previous application of the principle in the brain, called Venous Territory Imaging using Remote Sensing (VENTI) (98). The method is then applied to the SL-TRUST sequence, with a number of verification and optimisation experiments performed, and examples of the resulting T2 maps obtained in healthy controls.

5.1 Remote spatial encoding in NMR

Conventional NMR experiments use a single RF coil for both the encoding and detection of the signal from the sample of interest. A trade-off or compromise must therefore be met between the encoding and detection efficiency. The principle of remote spatial encoding was designed to separate these two processes in NMR experiments such that the coils used could each be optimized for each stage. For example, it may be favourable

for image information to be encoded at low field, due to lower susceptibility gradients, whilst detection is performed on a high-field magnet to improve the SNR (95).

What sets remote spatial encoding apart is the ability to not just move the sample from one location to another, but bring with it the spatial information from the previous location. The original work was conducted to investigate the properties of porous materials using a flowing NMR gas (95,96). By manipulating the chemical shift of the gas as it flowed through a sample, structural and chemical properties of the sample could be probed at a later time point with a separate detection coil. This indirect measurement provides information about the interaction between the gas and the sample in the encoding environment, instead of the detection environment (97).

In 2004 Seeley et al. demonstrated reconstructed images of xenon-129 gas passing through phantom samples with voids which form the letters CAL. An image of where the xeneon-129 had accumulated within the phantom was successfully reconstructed at a different temporal and spatial location, see Figure 5.1 (97).

The aim in this chapter is to apply this principle in the case of the blood signal in the sagittal sinus in SL-TRUST, with the aim of decoding the origin of the blood spins within the encoding environment of the tissue. A low resolution map of the spatial origins of blood spins within the brain is produced, and the process repeated for multiple T2-encoding steps, using the same T2-encoding module previously outlined for SL-TRUST. By measuring the decay of the blood signal from different spatial positions in the brain, the T2 of the blood and therefore the oxygenation of the tissue can be inferred. This process is illustrated in Figure 5.2.

Before exploring how remote reconstruction is achieved in practice, and the application in SL-TRUST, a similar approach using these principles in the brain is outlined. The VENTI method by Wong & Guo provided the inspiration for this project and was perhaps the first attempt to apply these remote sensing techniques in the human brain to investigate blood flow (98).

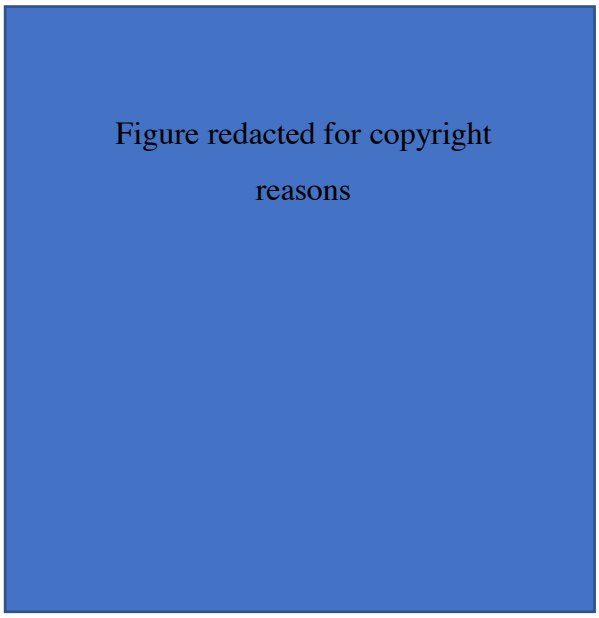


Figure 5.1 The inner structure of a phantom is reconstructed (A) by applying encoding gradients whilst xenon-129 gas passes through the phantom, after measuring the gas signal at a remote location. Three different measurements at different detection times (B, C, & D) are combined to produce a complete image (A). Figure produced by Seeley et al. 2004 (97) and reproduced with permission from author. DOI: 10.1016/j.jmr.2003.12.018. For copyright reasons this figure is redacted from the final published version of this thesis.

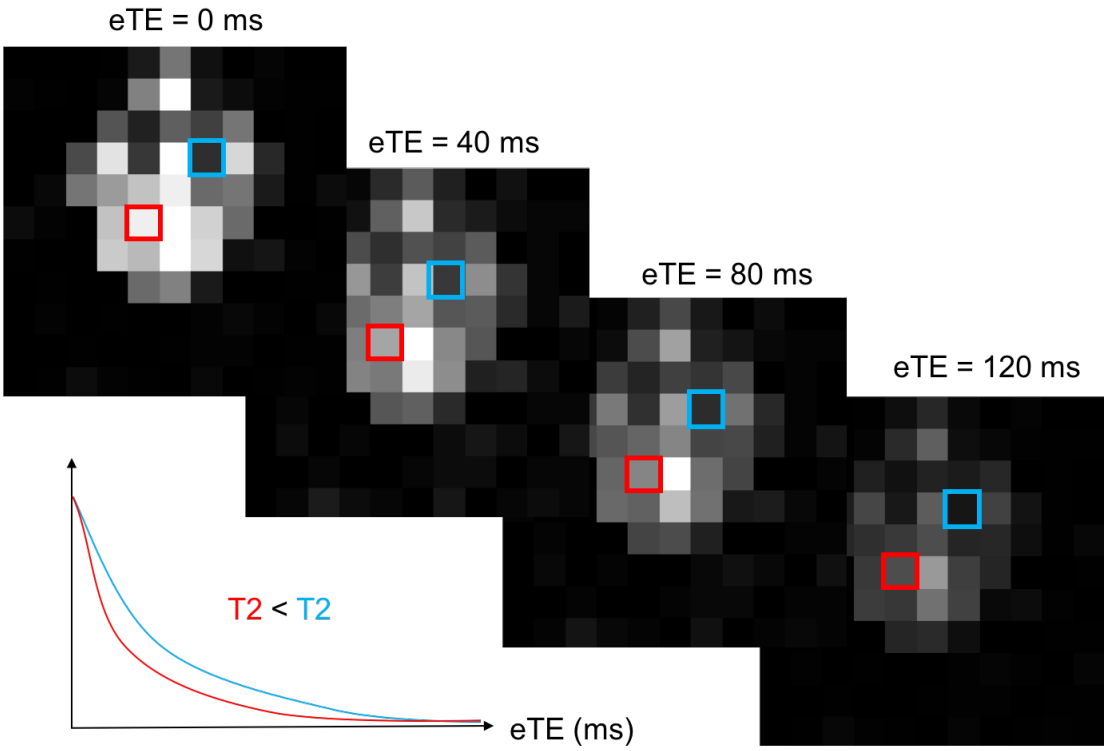


Figure 5.2 Illustration of the principle of remote reconstruction used in conjunction with SL-TRUST to measure the T2 of venous blood spins from across the brain. This shows a low-resolution 11×11 remotely-sensed image acquired axially through the brain. The reconstructed map at eTE = 0 ms is real data, however the signal decay in subsequent eTEs is simulated for demonstrative purposes and does not represent true decay under T2. The (simulated) T2 decay curves are normalised to enable the different T2 values to be visualised clearly.

5.1.1 VENTI: Venous Territory Imaging using Remote Sensing

Both vessel-encoded ASL perfusion and vessel-encoded ASL angiography have been successful in mapping the vascular territories of arterial blood. However, there is significantly less literature available which investigates or describes the venous vasculature and how blood is drained from the brain. Venous Territory Imaging using

Remote Sensing (VENTI) aimed to map these venous territories and measure intravenous T2 and as such infer the T2 of the tissue from which these veins drain.

To do so the VENTI method used remote sensing methods to spatially encode blood signal in the brain. Spin labelling and velocity selective pulse modules allowed for subtraction of static tissue signal, and isolation of venous blood spins (98).

The VENTI method was demonstrated by Wong in a single healthy subject and achieved a 2 cm resolution map showing 5 draining territories across the brain. An example of querying the data in reverse, to establish to which veins a particular region of tissue drains, showed not only individual veins for 4 territories but also a single path along the midline where the blood from all 4 regions had accumulated.

This chapter aims to apply the same spatial encoding described in VENTI, in conjunction with the SL-TRUST T2-encoding approach. Instead of querying multiple veins the aim is to query signal from tissue regions across the whole brain, by measuring in a single vein, the sagittal sinus.

5.1.2 Theory & phantom reconstruction

The principle of remote spatial encoding is to encode spatial information into the phase of the spins which, when constructively interfering to give a net magnetization vector with a certain amplitude and phase, is then stored along the longitudinal axis, where it can be measured at a later point. The spatial encoding is performed by applying a sinusoidal phase pattern across the sample using gradients along a certain direction.

In practice this is performed as follows: A hard 90° pulse flips the magnetisation in the sample into the x-y plane, followed by an evolution period τ_e. In NMR experiments this evolution period can be varied in order to probe flow properties and produce spectra of the sample. It is also a period during which a phase encoding gradient is used to produce a sinusoidal modulation in the phase of the spins along the direction of the applied gradient. A second 90° pulse flips the magnetisation back along the z-axis, storing a component of the net magnetization as information in the longitudinal plane. The second 90° pulse is phase cycled between the x and y directions to acquire both the real and the imaginary components of the original signal:

$$S_z = S_o \cos(\boldsymbol{k} \cdot \boldsymbol{r}) + iS_o \sin(\boldsymbol{k} \cdot \boldsymbol{r})$$

Equation 5.1

where $\boldsymbol{k}$ is the magnitude of the gradient zeroth moment and $\boldsymbol{r}$ is the spatial location of the spin.

In the same way 2D sampling of k-space in any MR method is determined by the gradient trajectories, the same concept is true here. Each acquisition of S_z represents a point in k-space corresponding to the phase accrual enforced on the spins by the combination of x-y gradients. Using Figure 2.9, the increment step between consecutive points in k-space determines the FOV of the image, and the maximum gradients in x and y are determined by the desired number of pixels in each dimension of the image, N. Using knowledge of the gradient moment it is also known that $k_{max} = \gamma G_{max} t$. For a gradient of fixed duration, t, the gradient amplitude, G_r, to acquire each step is therefore:

$$G_r = \frac{n}{2t}\left(\frac{1}{\gamma FOV}\right)$$

Equation 5.2

Where r is either x or y, and n = 1,2…., N. The factor of 2 arises from the fact that an NxN resolution image corresponds to ±N/2 steps in either direction out from the centre of k-space.

Figure 5.3 illustrates how the points in k-space are filled using the phase encode gradients on a circular phantom. The spatial pattern on the phantom corresponds to the coefficients of the gradients applied in each dimension, x and y. In this case the sum of the intensity across these images gives the signal for that point in k-space. This process must then be repeated to acquire the imaginary component by rotating the second 90° pulse. These two data points are then combined to produce a complex k-space array. For clarity the real and imaginary components are henceforth referred to as the cos- and sin-encoded components.

As each point in k-space is phase encoded and sampled independently (for both the k_x and k_y directions, unlike conventional 2D imaging which only phase encodes in k_y), and requires two acquisitions per point for the real and imaginary components, the resolution of the images is highly restricted. For that reason, due to time constraints (the full extent of which are described later), the resolution of the images produced using this method is much lower than is typical for conventional MRI, typically 11×11 for human experiments. For comparison, the VENTI method performed 8×8 Fourier encodes (98).

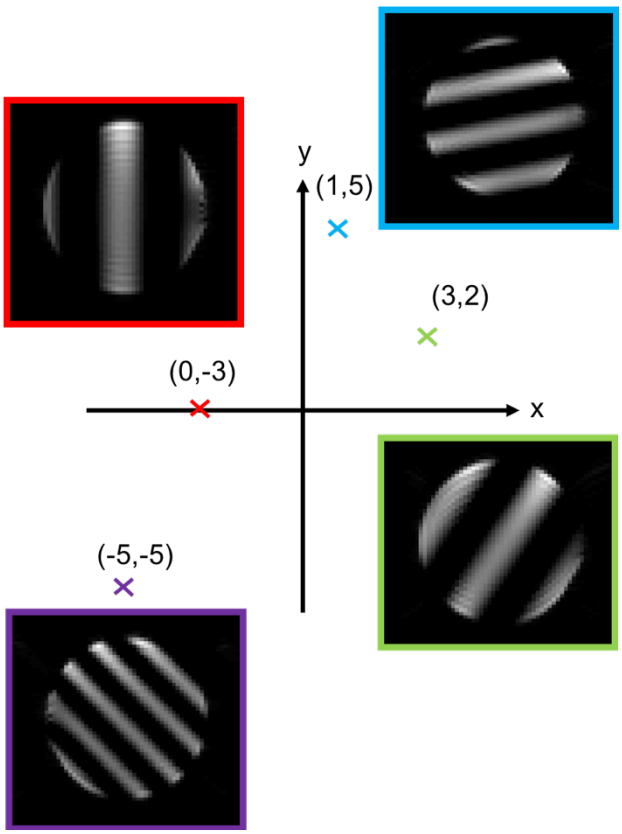


Figure 5.3 Example of phase encoding bands on a phantom within k-space. The net signal across the whole image is summed to give the relevant k-space signal. Note that the figure only shows the real components of the images.

Examples of reconstructed images of a phantom, using a k-space matrix constructed using the method described above, are shown in Figure 5.4. Both a higher resolution (25x25) reconstruction and an 11x11 reconstruction, showing the typical resolution achieved in a human brain, are shown. The figure also shows the effect of saturating signal from part of the phantom on the reconstruction.

It is important to note that these examples are **not** examples of remote reconstruction but rather a demonstration of how a k-space matrix can be filled, and successfully transformed into image space, when different phase encoding gradients are applied through the slice. For remote reconstruction in a brain the sum of the signal in pixels in the sagittal sinus is used to fill k-space. The signal in the sagittal sinus is the sum of all blood spins from across the brain and is therefore in effect the same as summing over the whole slice in a phantom image.

The 11×11 phantom reconstruction shown in Figure 5.4 demonstrates a phenomenon observed in the phantom reconstructions: a DC peak in the centre of the image. As discussed in 2.3.2 this arises from a uniform signal intensity offset across the whole of k-space which, when Fourier transformed into image space, appears as a high intensity peak at the centre of the image. In these cases it was necessary to either interpolate or dampen the signal intensity in this centre point in order to reveal the rest of the structure within the image. This effect was not as prominent in the human-reconstructed data due to the pairwise subtraction of tag and control images, which removed most of this baseline signal.

Another method of removing this DC peak would be to phase cycle the encoding pulses, however this is not explored in any more detail here.

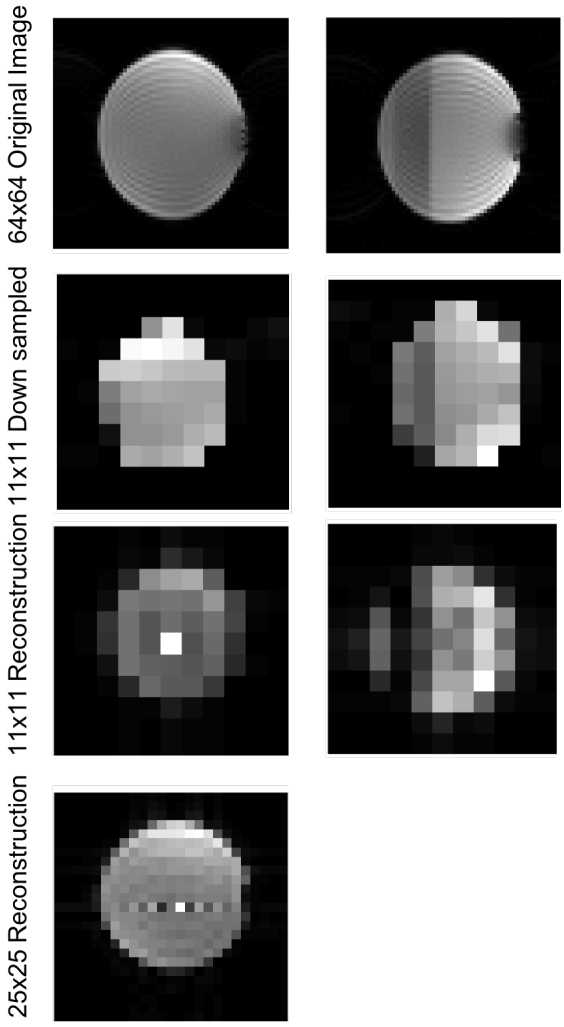


Figure 5.4 (LEFT) Phantom reconstructions at varying resolutions. (RIGHT) Example of a reconstruction where part of the phantom has been spatially saturated. The top row are the original 64x64 resolution images, the second row shows a downs sampled version of these images to match the resolution images in the third row which are produced using the acquisition and reconstruction described abov. The fourth row shows a 25x25 reconstructed image to demonstrate the possible resolution that could be achieved in brain using this method if significant acquisition acceleration were achieved. In all three reconstructed images a DC peak at the centre of the image has been interpolated although some residual signal can still be seen in the 11×11 reconstruction. Phantom images were acquired with the following sequence parameters: TR = 1s, TI = 50 ms, FOV = 170 mm.

5.2 Remote reconstruction in SL-TRUST

The principle of remote reconstruction in the case of SL-TRUST is that the same encoding patterns shown in Figure 5.3 are enforced on the blood spins in the brain. A tag or control inversion pulse selectively inverts a slab in the brain, providing the third axis of localisation. Following an inversion time, TI, spins accumulate in the sagittal sinus. Therefore, pairwise subtraction of tag and control images gives the total venous blood signal for those encoded spins in the sagittal sinus. The sum of the signal intensity in the sagittal sinus ROI gives the intensity in k-space for a particular phase encoding step. When this k-space matrix is transformed into image space the reconstructed image therefore represents the distribution of the venous spins in the brain at the time of encoding. The pulse sequence diagram is shown in **Error! Reference source not found.** and the details of the acquisition are described in further detail below.

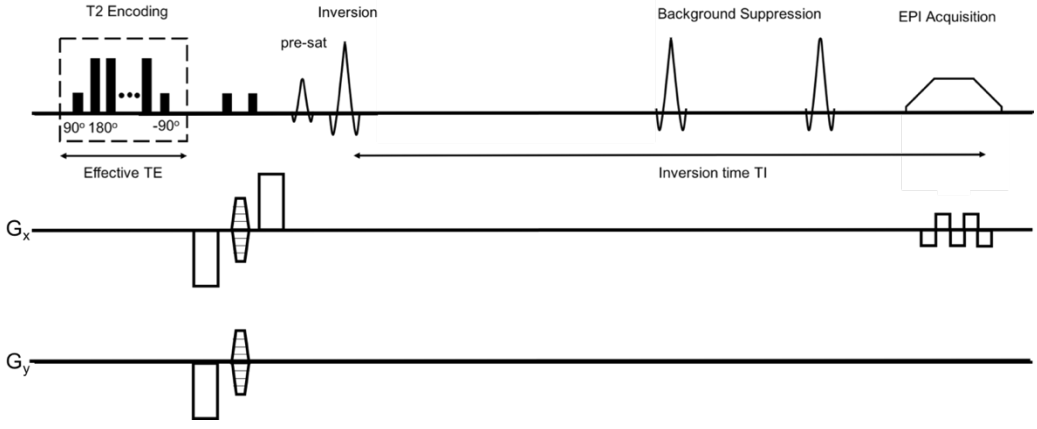


Figure 5.5 Pulse sequence diagram for SL-TRUST with phase encode gradients (and spoilers) in x and y. Gradients and pulses are not shown to scale. For illustrative purposes only.

5.2.1 Acquisition

In the context of SL-TRUST the phase encoding gradients described above are inserted in-between the T2-encoding module and the tag-control inversion pulse. The trapezoid-shaped gradient duration of the phase encode pulse was 1.5 ms. In practice the same 90° pulses used at the start and end of the T2-encoding module were replicated and used to tip the magnetisation into the transverse plane and back into the longitudinal plane. Early versions of the sequence acquired the cos and sin encoded components in separate scans. However, since the duration of each scan was up to 20 minutes this meant that there was a large time interval between the two (cos and sin) components at each point in k-space, leading to artefacts that resulted from scanner drift. Later versions of the pulse sequence therefore interleaved the two measurements in the same manner as the tag and control conditions are interleaved in the original TRUST/SL-TRUST sequence. An example of the parameters for the first few measurements of an 5x5 resolution scan are shown in Table 5.1. Other sequence parameters and timings were identical to those described for SL-TRUST in Chapter 3, except that the FOV was varied

Measurement	1	2	3	4	5	6	7	8	9	10	…	33	34	…	41
Tag/Control	T	C	T	C	T	C	T	C	T	C	…	T	C	…	T
Cos/Sin	cos	cos	sin	sin	cos	cos	sin	sin	cos	cos	…	cos	cos	…	cos
T2-encode	0	0	0	0	40	40	40	40	0	0	…	0	0	…	0
G_x	-2	-2	-2	-2	-2	-2	-2	-2	-1	-1	…	+2	+2	…	-2
G_y	-2	-2	-2	-2	-2	-2	-2	-2	-2	-2		-2	-2		-1

Table 5.1 Example measurement acquisition order for a 5x5 map with two T2-encode points

between 210-230 mm based on individual subject head size in order to maximise the proportion of signal in the image.

5.2.2 Reconstruction

Initial image reconstruction steps such as coil combination, pairwise subtraction, and sagittal sinus ROI identification were performed using the same processing steps as SL-TRUST, as outlined in 3.7.

An additional phase correction step is inserted following pairwise subtraction. The phase of each voxel in the cos encoded image, at zero phase encoding ($PE_x = 0$ & $PE_y = 0$), (example in a phantom shown in Figure 5.6), is used as a phase reference image which is applied to all subsequent phase encode steps on an individual voxelwise basis:

$$S_{corr}(k_x, k_y) \cdot \exp\left(-i \cdot angle\left(S_{0,0}(k_x, k_y)\right)\right)$$

Equation 5.3

therefore ensuring that any information contained within the phase due to polarity effects are transformed into the real component of the signal, which is then used to fill the k-space matrix. In the case of the phantom reconstructions demonstrated in Figure 5.4 this is performed over the whole image, whereas in the remote reconstructed human brain images this correction need only be performed in the voxels within the sagittal sinus ROI.

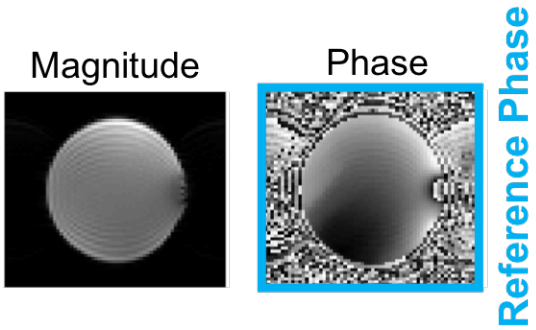


Figure 5.6 Magnitude and phase image at zero phase encoding of a cos encoded phantom. The phase image is used as a reference phase to perform phase correction on all other images.

Following phase correction, the real component of the signal intensity in the ROI for both the cos and sin encoding acquisitions are combined into a single complex number to fill the point in k-space which corresponds to the phase encode modulation applied. This whole process is illustrated in Figure 5.7 using a circular phantom. This k-space matrix is then transformed into image space using an Inverse Fast Fourier Transform (IFFT) in MATLAB.

The background suppression pulses used when the sequence is applied in humans mean that the phase encoding bands are not visible on the slice images, and therefore no examples are shown here. Figure 5.8 shows an example of a pairwise subtracted cos-encoded image at zero phase encoding, the k-space map and the resulting reconstruction representing the spatial distribution of underlying venous spins. For clarity, all remote reconstructed brain images shown in this chapter are orientated with the sagittal sinus near the bottom edge of the image.

For an NxN resolution reconstruction, with eTE_N effective echo times (points on the T2 decay curve), the total time to execute the sequence for a single T2 measurement would be $T = N^2 \cdot eTE_N \cdot TR \cdot 2 \cdot 2$ (s) where the two factors of 2 are for the tag/control

condition and for the cos/sin encoding acquisitions. For a typical SL-TRUST experiment TR = 4s, therefore to populate a full k-space matrix of resolution 11×11 and produce a single reconstruction such as the one shown in Figure 5.4 would take 32 minutes. Once this is extended to a full T2 mapping experiment using $eTE_N = 4$, the acquisition would take 128 minutes. To conduct any meaningful experiments using this method it was therefore critical to explore a means to reduce this acquisition time.

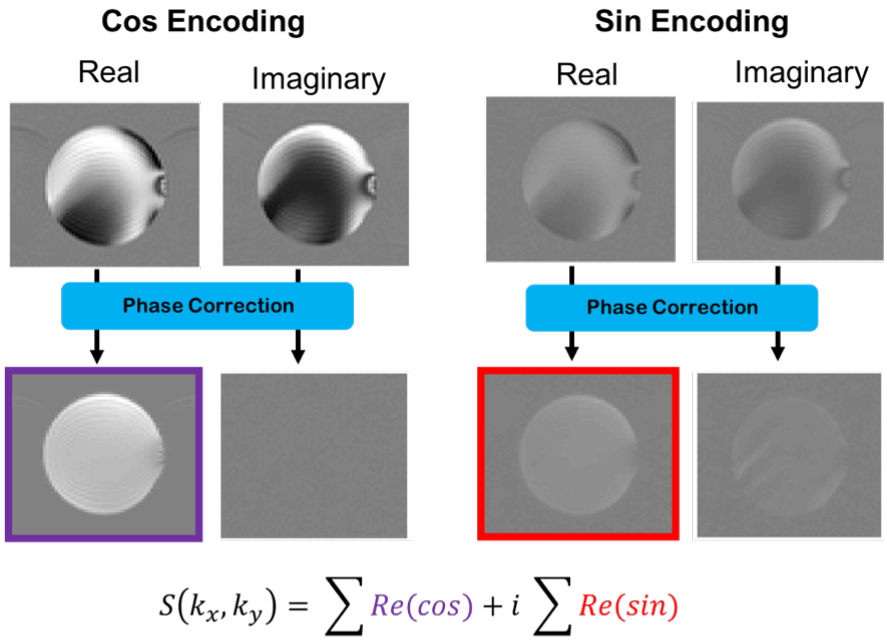


Figure 5.7 Reconstruction of k-space using real components of the cos and sin encoded acquisitions. This particular example demonstrates the centre of k-space, where no phase encoding gradients have been applied. The phase reference image is taken from the cos encoding acquisition and applied to all conditions, including later phase encode gradient steps. As a result, the phase images following phase correction are largely zero, with most of the information contained in the real images, the sum over which is then used to populate the k-space matrix.

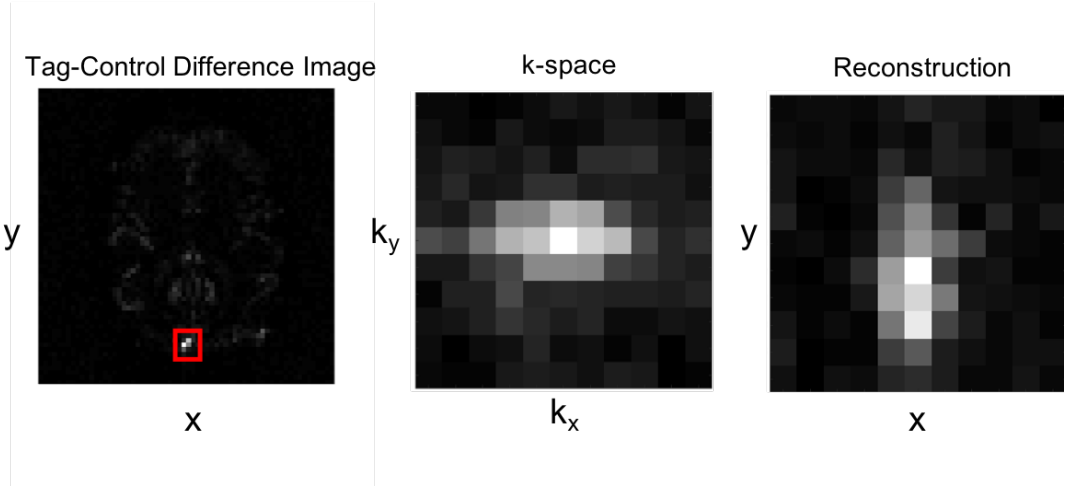


Figure 5.8 Example of a tag-control EPI difference image with the sagittal sinus ROI marked in red. The (magnitude plot) 11×11 k-space matrix and resulting low-resolution reconstruction of the venous blood spins. This k-space matrix is transformed into image space via a 2D Inverse Fourier transform.

5.2.3 Partial Fourier reconstruction

As outlined in 2.4.1, due to symmetry properties of the Fourier transform, half the information in k-space is related to the other half by the complex conjugate. Therefore, in some circumstances it is possible to only sample half of k-space and artificially generate the missing half.

Since in this method, each point in the remote reconstruction k-space matrix is sampled independently, the usual constraints and limitations of Phase- or Read-conjugate symmetry do not apply. There is a great deal more flexibility in the k-space sampling and thus the direction in which partial Fourier is performed is not of consequence.

5.2.3.1 Zero-filling

The most straightforward Partial Fourier reconstruction method is zero-filling, whereby no attempt is made to estimate the missing k-space data. However, this leads to a step function along the boundary in k-space causing significant blurring along the partial Fourier direction. This is demonstrated in Figure 5.9 where top-to-bottom partial Fourier is simulated in a phantom reconstruction. The difference image between fully and partially sampled reconstructions shows how the DC peak has been smeared across the sampling direction. This step function can be especially problematic when using the Fast Fourier Transform on low resolution data sets, such as is the case here.

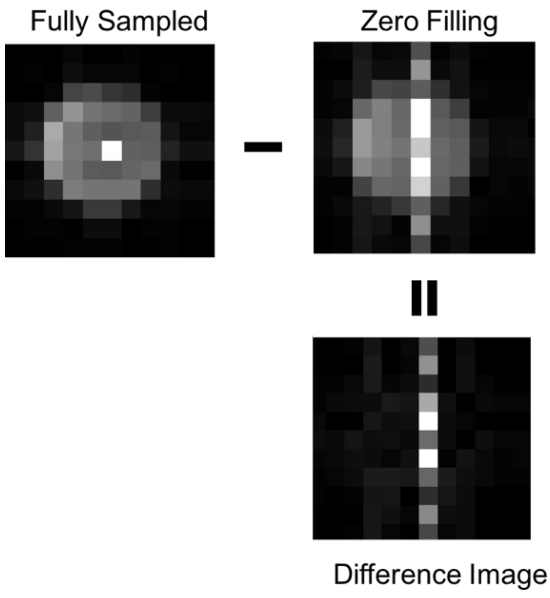


Figure 5.9 Example of smearing in zero filling partial Fourier reconstruction

5.2.3.2 Projection onto convex sets (POCS)

Projection onto convex sets is an iterative method of filling the empty k-space points and operates under constraints in both image and frequency space (99-101).

Using only the symmetrically sampled k-space data a phase correction image in image space is produced $m_s(x, y)$. This is used iteratively to apply a phase constraint such that the phase of the total k-space image conforms to this phase estimate. A Fourier transform of this phase corrected image gives the new k-space matrix. The portion of k-space which is synthesised is carried forwards whilst the original sampled k-space points are constrained, these two sections are combined to form a new and complete k-space matrix. The process continues iteratively updating k-space, as shown in Figure 5.10, until the difference between two consecutive iterations is below the noise floor of the MRI data (102). The method converges quickly, typically within 10-20 iterations.

Figure 5.11 demonstrates the improvement achieved using POCS in comparison to zero filling in a reconstruction of an EPI (64×64) image of a brain with 70% Partial Fourier acquisition simulated using a fully sampled data set.

In using 70% Partial Fourier and POCS reconstruction the duration of an 11x11 acquisition, with a TR = 4s, can be reduced to just over 23 minutes. Whilst this is clearly still too long for any form of clinical use, it does allow for multiple acquisitions within a single 1-1.5 hr scan slot which can be tolerated by healthy research participants. This allows for the investigations outlined below, used to verify and optimize SL-TRUST remote reconstruction using phase encoding.

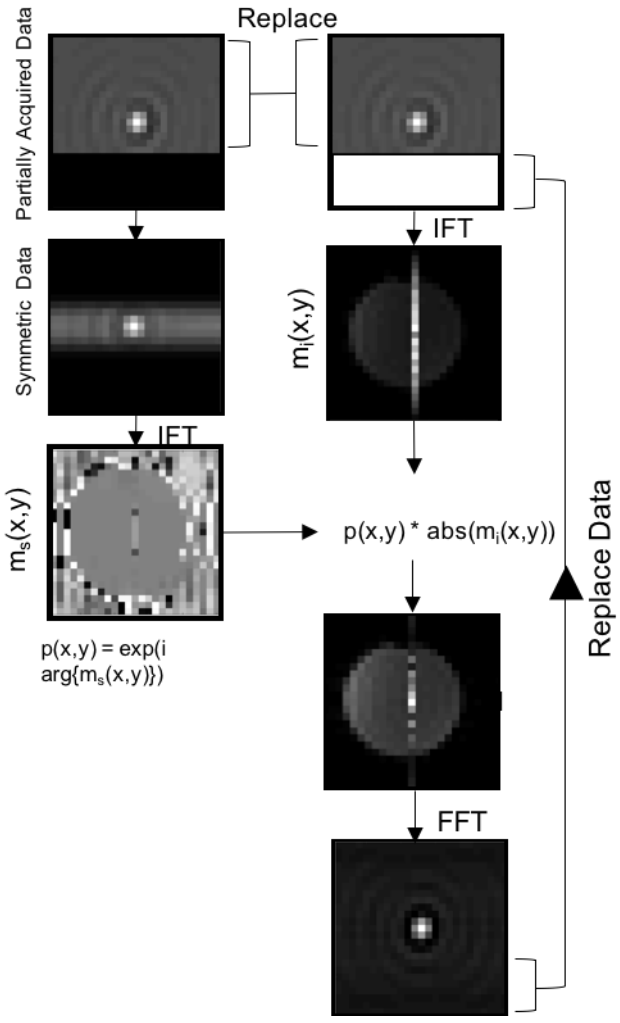


Figure 5.10 Iterative pipeline for POCS starting with creating a phase estimate using the symmetric parts of k-space. This is then used to produce an estimate of the un-sampled k-space points, which are inserted into the partially sampled k-space matrix. The sampled parts of k-space are retained at each iteration. Diagram based on lecture notes from John Pauly, Standford University (102).

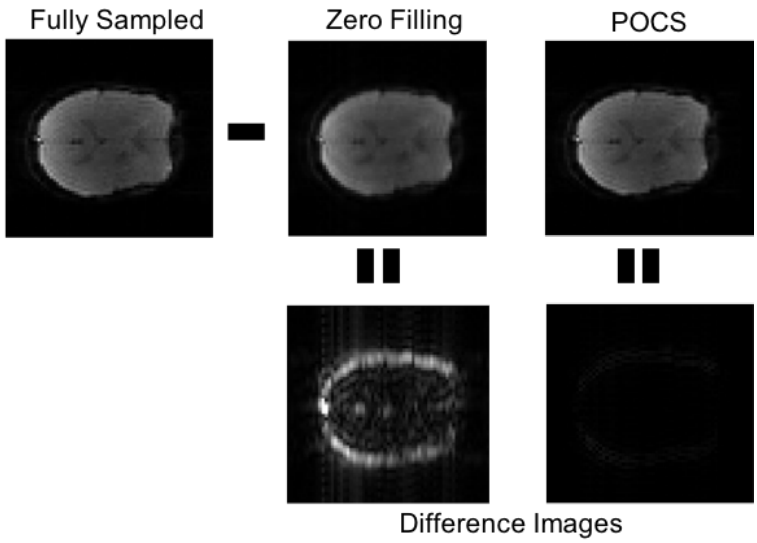


Figure 5.11 Comparison of POCS and Zero Filling reconstruction on an example EPI data set for 70% partial Fourier. Difference images use the same intensity scales to allow for direct comparison.

5.3 Validation and optimization

Before attempting to obtain T2 maps in healthy controls there were two key experiments required to verify the method and optimise the acquisition. These were performed in parallel, however are presented here in the following order: validation followed by optimization.

5.3.1 Validation: spatial dependence

Firstly, to verify that the method is sensitive to the spatial origins of the spins, WET saturation pulses, previously introduced and used for SL-TRUST in Chapter 3, were re-inserted to spatially saturate and remove signal from particular brain regions. The aim was to demonstrate that the lack of venous blood signal from those regions would be

visible on the remote reconstruction, thus verifying that the remote reconstruction maps were sensitive to the spatial origins of the spins. Two spatial regions were saturated: an entire hemisphere, and the frontal region, and the effect on the reconstructed images was observed. Figure 5.12 shows an example in a single subject (F, 23) of frontal region saturation alongside a whole brain reconstruction to demonstrate the removed signal. A further example shown in Figure 5.13 in a second subject (M, 31) compares frontal and hemispheric saturation.

As expected, the reconstructions show either zero or at least reduced signal in the regions of WET saturation, demonstrating that the method is sensitive to the spatial location of the spins at the time of phase encoding.

All of these acquisitions were performed using an inversion time of TI = 2 s. This differs from the inversion time previously used for SL-TRUST, which is discussed further in the next section.

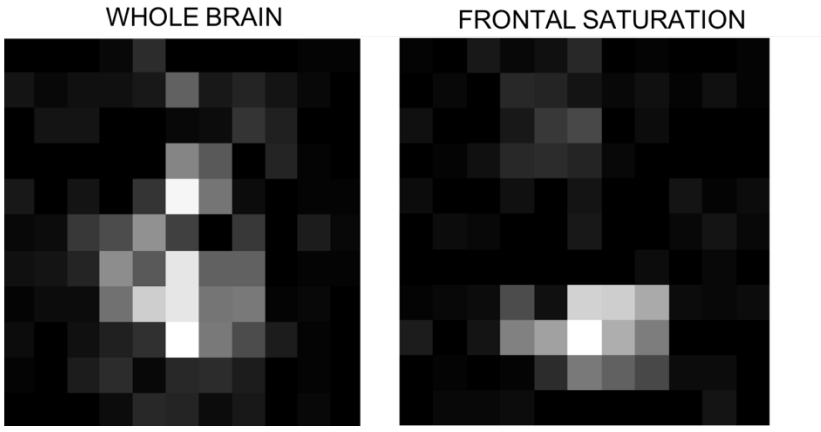


Figure 5.12 Whole brain reconstruction (left) in comparison to a frontal (right) WET saturation demonstrating the removed signal.

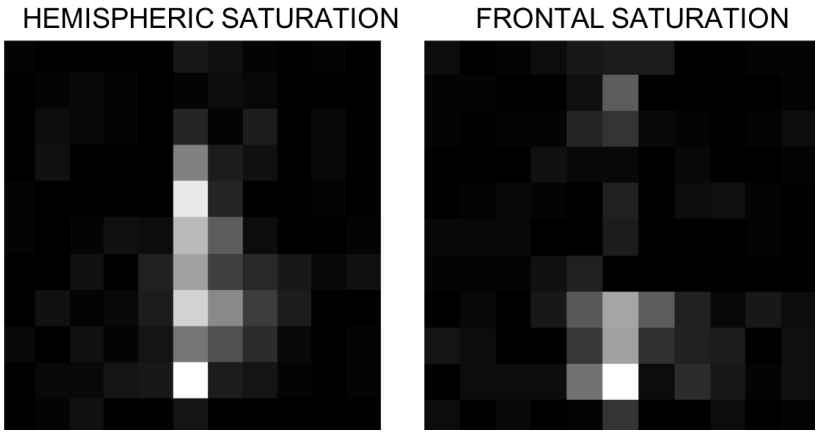


Figure 5.13 Comparison of remote reconstruction following WET saturation of a hemisphere (left) and a frontal region (right).

5.3.2 Optimization: TI dependence

Initial acquisitions using an inversion time identical to that used in TRUST and SL-TRUST TI = 1200 ms revealed what looked like the signal being concentrated down the midline of the brain. This is similar to the observations from the venous draining territory images obtained using VENTI described in 5.1.1 (98). To confirm this, and find an optimum inversion time for the SL-TRUST method a variety of inversion times TI = 1400, 1800, 2000, and 2200 ms were tested in a healthy control subject (F, 25). The results are shown in Figure 5.14.

At TI = 1400 ms most of the signal appears to be from the occipital lobe and midline, whereas when the TI is extended to TI = 1800 and 2000 ms more of the signal appears to be arriving from the more lateral brain regions. At the maximum tested inversion time of TI = 2200 ms the balance between the number of blood spins arriving versus the inherent T1 decay of the signal appears to reach a stage where there is a net loss of signal. TI = 2000 ms was tested in several other subjects, shown in Figure 5.14, and gave consistently good reconstructions and is therefore the recommended inversion time for this method at this stage.

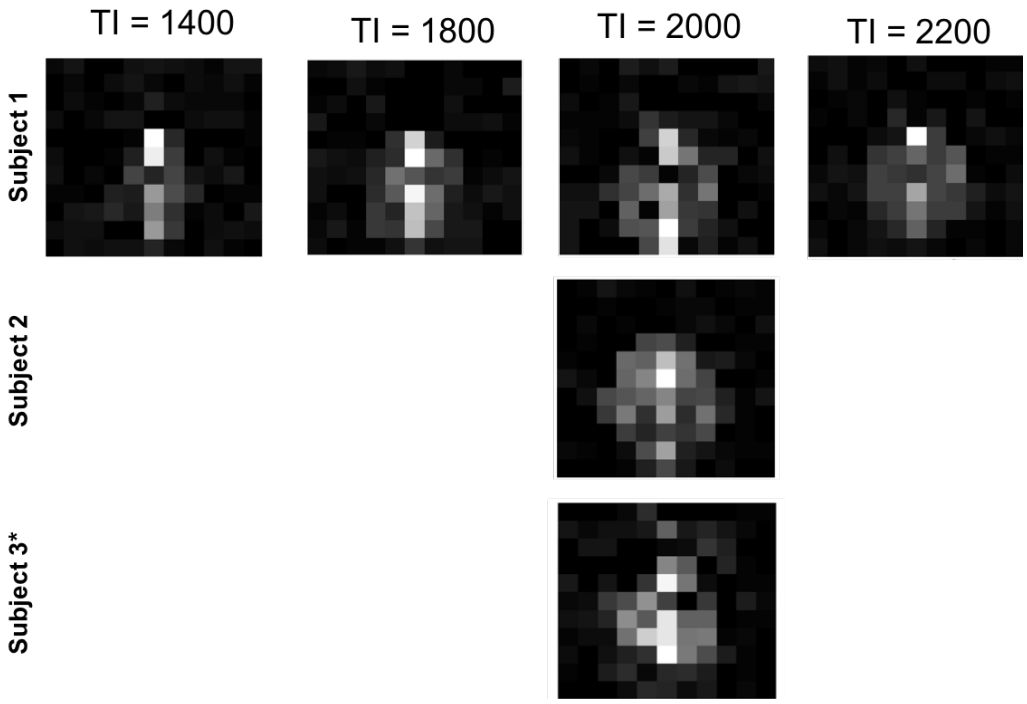


Figure 5.14 Inversion time dependence for phase encoding remote reconstruction. *Subject 3 was acquired without interleaved cos and sin encoding acquisitions and is therefore more noisy. (2F, 1M, average age = 25 years)

5.4 T2 mapping in healthy controls

Two full T2 maps in healthy controls were obtained using PE_{steps} = 7, eTE = 0, 40, 80, 120 ms, with 70% partial Fourier. The total scan duration was 37 minutes. A whole-brain conventional TRUST T2 measurement was acquired in the same scan session, for comparison. The acquisition protocol for TRUST is identical to that outlined previously, with the exception of the inversion time, TI = 2 s, to match that of the remote reconstruction SL-TRUST method. The two T2 maps are shown in Figure 5.15.

The average T2 across the two maps is 60.3 ± 14.3 ms and 63.1 ± 8.7 ms (mean ± std across all voxels in the brain). In comparison the TRUST T2 values were found to be 56.16 ms and 56.66 ms respectively. Overall, there is significant variation in T2 across the maps. The voxels with the highest blood signal have T2 values that match well with the T2 using whole-brain TRUST. Areas of poorer signal intensity tend to overestimate T2, with some values up to 90-100 ms long. These would translate to OEF values of around 20%, much lower than expected. These are visible in the images as brighter voxels around the edges of the brains.

Figure 5.16 shows the maps of one of the subjects shown in Figure 5.15, at each of the four eTE steps. Note that here the intensity values across the image corresponds to the amount of venous blood signal in that voxel at that time point, rather than the T2 value. Figure 5.16 also shows the resulting normalized T2 curves for two voxels within the map which demonstrate them matching well.

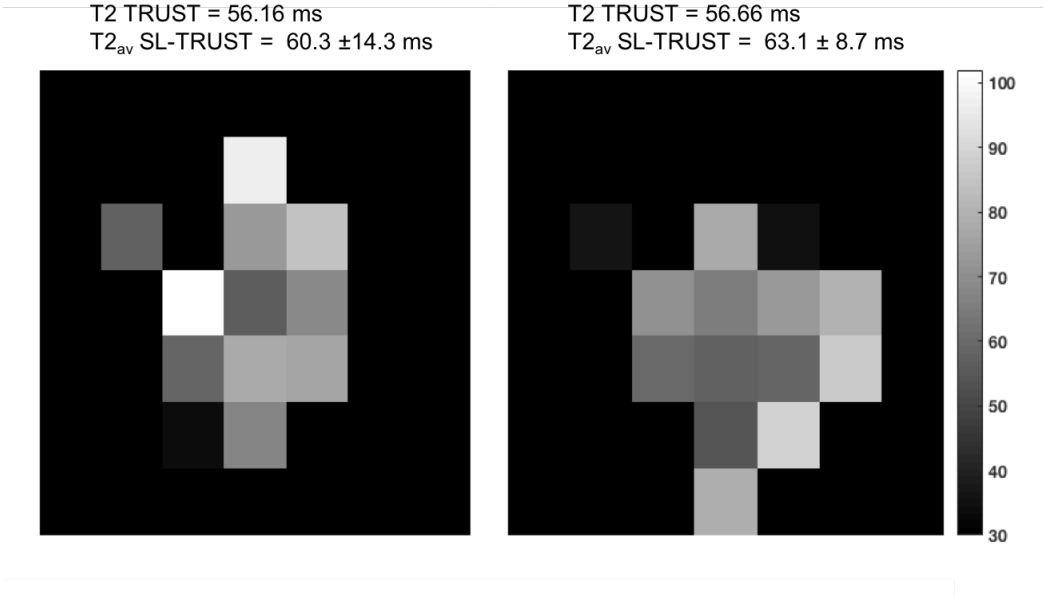


Figure 5.15 Two T2 remote reconstructed maps from healthy controls (F, 25 & M, 31). The pixel intensity corresponds to the T2 in that voxel (the surrounding black voxels are all zero signal intensity rather than areas of T2 = 30 ms as the colour bar suggests). The global T2 measured using TRUST is displayed above each image, along with the average T2 across all the brain voxels in the image. Whilst the average T2 is not unreasonable, there is significant variance in T2 values across the maps, with some T2 values up to 100 ms in some cases. Maps acquired using 70% Partial Fourier and POCS reconstruction, 4 eTE points (0, 40, 80, 120 ms), TR = 4s, TI = 2s. TRUST T2 measurements acquired using 6 eTEs (0, 40, 80, 120, 160, 200 ms), TR = 8s, TI = 2s.

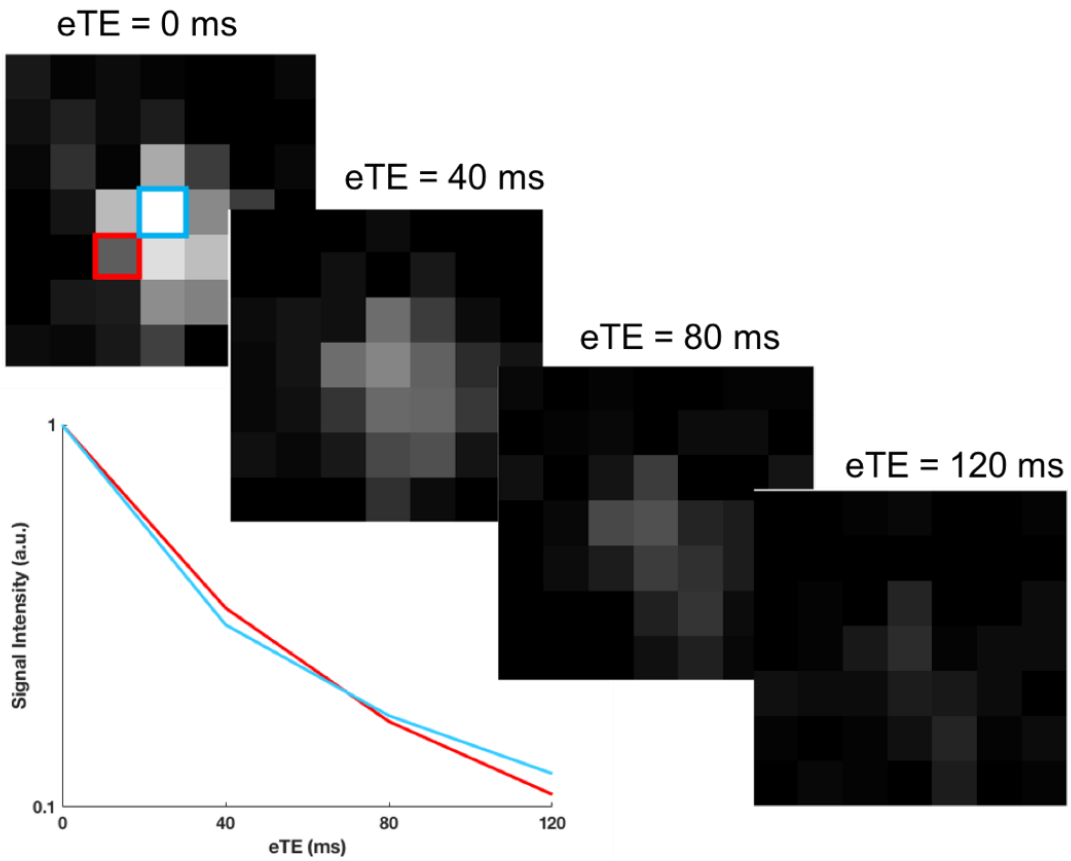


Figure 5.16 Maps at varying eTE for a single subject and the T2 decay curves (normalised) for two representative voxels within the maps. The signal intensity represents the amount of blood signal originating from that region of the brain.

5.5 Discussion

Summary of key findings:

- A new method of remote reconstruction to acquire a T2 map of a slab in the brain was successfully incorporated into the SL-TRUST sequence at 3T.
- The optimum inversion time to capture blood spins deeper into the vasculature was found to be TI = 2 s
- Partial Fourier sampling and reconstruction was used to speed up acquisition time.
- 7x7 resolution T2 maps of venous blood spins, using 4 effective echo times took 37 minutes

Using principles from gas NMR experiments whole-brain maps of venous blood T2 were reconstructed using only the signal from venous blood spins signal measured in the sagittal sinus. Whilst still in its infancy, and with much scope for improvement, this work provides proof-of-concept for the methodology and some initial work to optimize and verify the method. These include investigating the optimum inversion time, TI, at which the method captures blood signal from more lateral regions of the brain than only the midline, which seems to arrive in the sagittal sinus first. For the purpose of this work an inversion time of TI = 2 s was chosen as being the most appropriate. Whilst this requires further quantitative assessment and validation in a larger subject cohort, it is reassuring

that this is the same time used in the VENTI approach on which this method is based (98).

Inclusion of the WET saturation scheme verified the specificity of the method to the spatial origins of venous blood spins in the brain. This could be utilized further to establish optimum inversion times from different regions of the brain. Similarly, further work to validate the optimum sequence parameters would benefit from the use of a flow phantom in order to investigate the effect of non-uniform flow and blood arrival times. As illustrated in Figure 5.1, Seeley et al. 2004 showed that, in order to capture a complete overall picture of the underlying structure of the phantom, multiple batches were required at various detection times (97).

Partial Fourier methods were successfully applied to reduce scans times for whole-brain T2 maps from over 2 hours to under 40 minutes. However, the achieved resolution is still very low, just 7×7 voxels. There is scope to speed up acquisition further using compressed sensing methods. Compressed sensing lends itself well to this technique, since the sampling of k-space can be truly random. Thus higher quality T2 reconstruction could be readily achieved.

The number of eTE sampling points is also limited to four: eTE = 0, 40, 80, 120 ms. The decision was taken to sample more points at lower echo times in order to capture the initial exponential decay. It was understood that a maximum eTE = 120 ms was likely too short to capture the full decay of the blood given the estimated T2 values were in the region of 50-70 ms. Therefore, the number of effective echo times eTE used to produce the T2 curves would ideally also be increased, in order to sample echo times later than

120 ms and thus capture the full T2 decay curve. Additionally some investigation into the most efficient distribution of sampling of eTE at low sampling numbers could be performed, however it should be noted that the increments of eTE are constrained by the number of refocusing pulses per increment and the inter-echo spacing between them.

The acquired T2 values are mostly within the expected range, with some particularly promising voxels in both subjects matching the T2 acquired using TRUST. However, there is a large degree of variance in T2 values across the brain using the currently implemented method and a tendency to overestimate T2 and thus underestimate OEF in voxels where there is less signal available. This same effect was observed in the development of regional SL-TRUST prior to implementing background suppression techniques and is therefore thought to be driven by poor SNR. This is made worse by the fact that only one T2 curve is acquired in this method, therefore unable to smooth out any noise effects using multiple averages.

Further improvements include incorporating the phase encoding gradients within the T2-encoding module, inserting them in-between the final 180° pulse and the second 90° pulse, instead of in a separate module. With a maximum gradient duration of 1.5 ms and a gap of 5 ms between these two pulses in the current T2-encoding module there is more than sufficient time for this to be feasible. This might also reduce signal loss by avoiding the unnecessary 90° pulses around the phase-encode gradient, especially if they are imperfect. The FOV dimensions could also be optimized. The FOV is currently constrained to be square. By making it rectangular and calculating the amplitudes of x and y gradients to correspond to these different dimensions in each direction, it is possible

to increase the number of voxels that contain brain tissue signal and reduce the unnecessary sparsity within the images.

Whilst this method is still some way from being applicable outside the realms of research, the method combines a number of different techniques effectively in order to produce whole-brain venous T2-maps whilst retaining the robust measuring approach in the sagittal sinus that has proven so successful in the original TRUST method. With some improvements this technique could provide valuable information regarding venous physiology and regional changes in T2, something that is still a unmet need.

Where this method benefits in comparison to methods such as VSEAN and TRU-PC described in 2.7 is the ability to produce maps through a whole slice or slab of the brain, rather than being limited to regions where we can image the blood vessels directly. In theory, by always measuring T2 in the sagittal sinus, the T2 values are also more robust, and not contaminated by phase contrast errors. Methods such as VSEAN are also limited to single slice maps. SL-TRUST can achieve T2 maps of a slab in the brain (compressed to 2D), with the width of the slab varied by varying the inversion slab thickness (within SNR limitations).

Chapter 6 Conclusions, recommendations & future work

6.1 Summary

The SL-TRUST sequence developed in this thesis was designed to address previous limitations of the TRUST method by enabling regionally specific measurements of OEF to be made. In Chapter 3 the steps taken to optimize the sequence to achieve this aim were outlined. These included the implementation of optimized WET saturation schemes for effective and efficient saturation of venous blood spins in brain tissue, and background suppression methods in the readout slice to help mitigate partial volume effects from surrounding static tissue and also to counteract the effect of moving the T2 encoding earlier in the sequence.

Chapter 3 also detailed some experiments to determine the optimum sequence timings for SL-TRUST, such as the inversion time and the repetition time of the sequence. Later work presented in Chapter 5 showed some findings that have implications not only on the chosen inversion time used for SL-TRUST, but also on the original sequence TRUST. These are discussed in more detail in this chapter.

In Chapter 4 a reproducibility study showed that an OEF comparison of 2 contralateral regions can be achieved in under 5 min on a standard 3T system with a CoV of under 5% using the SL-TRUST method. This is comparable both in precision and duration to whole-brain TRUST and the gold standard of PET O15. Chapter 4 also presented a method for measuring the T1 of venous blood in the sagittal sinus, in addition to the T2 measurement. Using a model relating T1 and haematocrit, derived empirically from *in vivo* experiments in male adults, individual haematocrit values were calculated and used in order to attempt to obtain absolute values of OEF. The T1 sequence, however, was not as robust as desired, and as a result a number of the haematocrit values were outside the expected physiological range. As such, it cannot be concluded that absolute values of OEF were obtained in this thesis. Nevertheless, there is evidence that SL-TRUST is sensitive to relative changes in OEF, with the same fluctuations across scan sessions in the same individual observed across the global TRUST and regional SL-TRUST methods. Possible validation of this sensitivity to changes in OEF include using gas challenges, however this would only reflect global OEF changes, not regional ones.

Data from two stroke patients did not yield regional OEF differences using the SL-TRUST sequence. It is thought that simple activation tasks used in fMRI, such as visual chequerboard tasks or finger tapping, would not result in a large enough spatial extent of change in OEF to be detected using this method. The best approach is therefore to continue validation in patient populations with regional OEF differences.

Finally, Chapter 5 presented a further adaptation of the SL-TRUST method. Here, by using remote reconstruction methods from NMR, low resolution T2 maps of tissue in

the brain were produced using the SL-TRUST sequence. This is achieved by encoding the spatial information of the venous blood spins into their phase, which is subsequently encoded into the longitudinal magnetisation and decoded at a later time point and location. Despite efforts to speed up the acquisition using partial Fourier methods, this approach is still highly time consuming and therefore at this stage does not have any realistic clinical applicability.

6.2 On-going and future work

This section presents a number of ideas that have been explored briefly, as well as some discussion and recommendations that have arisen as a result of the key work presented in this thesis. Finally, some further work being conducted by others in the group as extensions of the SL-TRUST method are shown.

6.2.1 Inversion time recommendations

Even within healthy populations there is some more work to be done to identify the optimum inversion time for both SL-TRUST, and the global method, TRUST.

In Chapter 3 the optimum inversion time for SL-TRUST was found to be TI = 1200 ms. This matched previous work using TRUST and therefore appeared to work well for both sequences, allowing a good comparison between the signal intensities obtained using each method.

Later work, however, when attempting to reconstruct the spatial origins of venous blood spins in Chapter 5, appeared to show that at TI = 1200 ms the majority of the blood spins

in the sagittal sinus originated from tissue located close to the midline of the brain. Instead, a longer inversion time of TI = 1400 - 2000 ms was required to target spins originating from more lateral regions of the brain.

In conventional TRUST the chosen inversion time is of less consequence, the only requirement is that it is sufficiently long for enough spins to have arrived in the sagittal sinus from the tagging slab to maximise the SNR, although it could call into question the "global" nature of the method if the target spins are primarily from the midline of the brain.

Conversely, in SL-TRUST the inversion time is more important and has further-reaching implications. Depending on the positioning of the target area SNR may be severely compromised, or the T2 measurement may be spatially biased within the target tissue. This may also explain the larger than expected drop in signal observed for regional SL-TRUST.

As such, it could be that spatial localization using SL-TRUST could be optimised further by using a longer inversion time. However, at these longer inversion times there is a trade-off between targeting spins from within the vasculature, and a loss of SNR due to T1 decay of the signal, which would also have to be taken into consideration.

6.2.2 SL-TRUST without pairwise subtraction

From observation of the tag images obtained using SL-TRUST it was noted that due to the effective removal of the static brain tissue signal using background suppression methods, the blood signal in the sagittal sinus was easily identifiable even prior to

pairwise subtraction. Without the requirement of a control image scan times can be halved, the benefits of which are clear: increasing clinical applicability, and allowing additional measurements within the same available scan time. This is precisely what was achieved in the original work applying multiple inversion recovery methods in angiographic sequences (42). Therefore, the idea of whether acquiring both a tag and a control image was necessary in SL-TRUST was briefly investigated. Using measurements from the first scan session in a subset of subjects used in the reproducibility study in Chapter 4, the analysis pipeline was repeated using only the tag images instead of tag-control pairwise subtracted images.

In the global case, when measuring the T2 using only the tag image the measured value was in most cases within the error bounds of the T2 obtained using pairwise subtraction. This was not the case for regional T2 values, see Table 6.1. This is thought to be due to residual background signal becoming more significant as the overall signal intensity of the blood signal decreases, resulting in a lengthening of the measured T2 values. In some cases the T2 for both the hemispherical and 3D-localized cases were clearly contaminated by non-blood signal, giving apparent blood T2 values of over 100 ms. An example of the offset observed in the T2 decay curves for a single subject is shown in Figure 6.1.

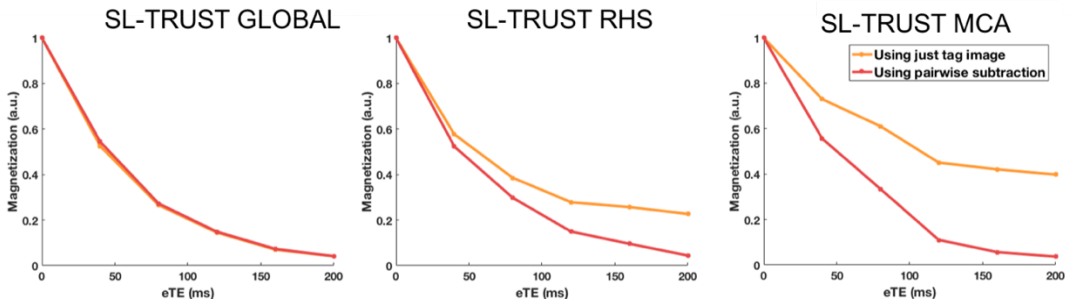


Figure 6.1 T2 decay curves for SL-TRUST with and without pairwise subtraction of tag and control images

Table 6.1 T2 values (mean ± std) for SL-TRUST when using pairwise subtraction method in comparison to when just the tag image is used. (Error calculated using the residuals of the fit)

	Using pairwise subtraction			**Using only tag image**		
Subject	**Global**	**RHS**	**MCA**	**Global**	**RHS**	**MCA**
1	50.7 ± 1.1	67.4 ± 7.3	53.8 ± 3.9	57.7 ± 1.0	93.3 ± 3.0	111.8 ± 9.0
2	65.3 ± 3.3	62.2 ±3.5	57.4 ± 3.4	59.2 ±3.7	70.1 ± 4.4	79.0 ± 5.3
3	60.5 ± 0.9	62.0 ± 1.2	61.9 ± 4.2	59.0 ± 0.5	97.1 ± 8.8	168.3 ± 6.1
4	76.1 ± 2.2	68.6 ± 3.4	76.6 ± 1.9	70.7 ± 2.0	73.6 ± 6.1	114.1 ± 5.7
5	61.3 ± 1.5	59.1 ±1.9	67.0 ± 6.1	62.2 ± 1.5	102.8 ± 8.6	201.5 ± 9.8

At this stage it would therefore not be recommended that the SL-TRUST method is a candidate for removing the pairwise subtracted condition in the acquisition, despite the use of background suppression in the sequence. There is, however, scope to investigate other means for removing the offset observed in Figure 6.1, such as a single control image at a later effective echo times in order to estimate and mitigate the offset.

6.2.3 Compressed sensing in phase encoded SL-TRUST

As mentioned briefly in 5.5 the phased encoded SL-TRUST approach to produce maps of T2 and therefore OEF could benefit greatly from compressed sensing methods to speed up the acquisition. Even with partial Fourier methods the acquisition time of higher resolution T2 maps (minimum 11x11) is still in the order of hours. Reducing this duration is critical, not just in terms of applying the method clinically, but also in progressing the method within research.

Compressed sensing lends itself well to this particular method as each point in k-space is sampled independently, and therefore k-space can be sampled completely randomly if required. Due to the sparsity within the image different sampling patterns could be used across multiple eTE points and a joint reconstruction approach used to generate the missing points at each time point.

Future work on producing T2 (and OEF) maps using the phase encoding and remote reconstruction approach will focus on implementing compressed sensing acqusitiion and reconstruction, in order to drive forwards further experiments to validate and test the method. This will begin by simulating compressed sensing in existing fully sampled data sets.

6.2.4 Applying SL-TRUST at 7 Tesla

The SL-TRUST sequence is already being adapted further in work beyond this thesis by Yan Tong in the FMRIB Physics group. Here SL-TRUST is being developed as a method at 7T and thus able to take advantage of parallel RF excitation capabilities to produce selective excitation pulses. Spatial localisation of a cylinder or 3D volume can in principle be achieved using these types of pulse to selectively invert an ROI, instead of

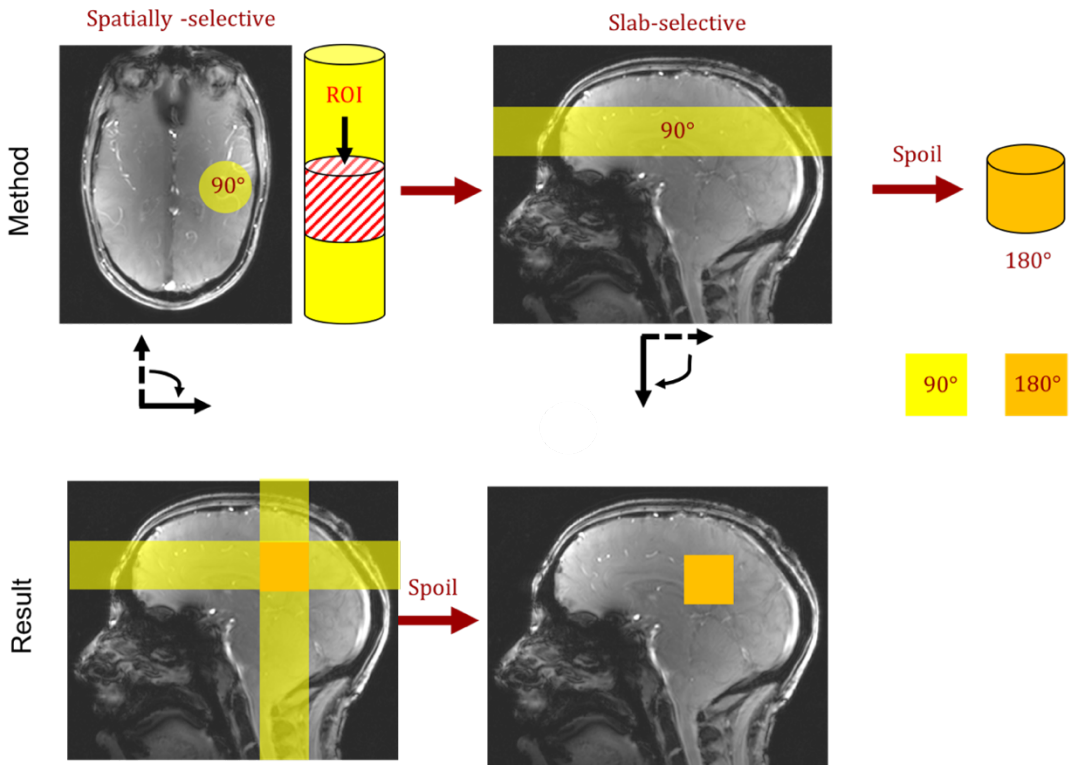


Figure 6.2 Label condition using two intersecting 2D cylindrically selective excitation RF pulses to give a 3D spatially selective inversion in an ROI within the brain. The control condition then uses a similar strategy except that one of the slab-selective pulses has opposite phase, thus the total angle in the ROI is zero. Image reproduced with permission from Yan Tong.

using (potentially imperfect) outer-volume saturation methods to provide the spatial localization.

Achieving a full 3D 180° selective inversion pulse in the head is an incredibly complex task, thus the current approach is to combine two selective excitation strategies which when combined result in a full inversion within a specified ROI, see Figure 6.2.

If successful, this would potentially constitute a significant advancement of the SL-TRUST method, negating the need for WET saturation pulses. The disadvantage is that the hardware required to deliver selective excitation pulses with a reasonable pulse length is currently not available on clinical scanners, since it requires multiple transmit channels, and is therefore not accessible for application in clinical populations at present.

6.3 Final remarks

SL-TRUST has demonstrated the potential to become a reliable, robust, and rapid method of quantifying regional OEF differences. Although there exist MR methods that can achieve higher spatial resolution OEF maps than SL-TRUST, these also suffer from unexplained systematic biases in the measurement and can be highly dependent on sequence parameters. Even localizing to individual hemisphere OEF, such as has been achieved here using SL-TRUST, has been identified as a powerful clinical tool (e.g., as a predictor of future stroke risk and collateral flow capacity in patients with complete carotid artery occlusion) (15). Overall, SL-TRUST allows for better understanding of brain physiology in both healthy and clinical populations in a non-invasive and time-efficient manner and can be performed easily on clinically available MRI scanners.

References

1. He X, Zhu M, Yablonskiy DA. Validation of oxygen extraction fraction measurement by qBOLD technique. Magn Reson Med 2008;60(4):882-888.
2. Bernstein M, King K, X J. Handbook of MRI Pulse Sequences: Elsevier Academic Press; 2004.
3. Brown R, Cheng Y, Haacke E, Thompson M, Venkatesan R. Magnetic Resonance Imaging: Physical Principles and Sequence Design: John Wiley & Sons, Inc; 2014.
4. Nishimura D. Principles of Magnetic Resonance Imaging: Standford University; 2010.
5. Purves D, Augustine GJ, Fitzpatrick D, Katz LC, LaMantia A-S, McNamara JO, Williams SM. The Blood Supply of the Brain and Spinal Cord: Sinauer Associates; 2001.
6. Tsivgoulis G, Alexandrov AV. Cerebral Hemodynamics in Acute Stroke: Pathophysiology and Clinical Implications. J Vasc Interv Neurol. Volume 1; 2008. p 65-69.
7. Mao D, Li Y, Liu P, Peng SL, Pillai JJ, Lu H. Three-dimensional mapping of brain venous oxygenation using R2* oximetry. Magn Reson Med 2018;79(3):1304-1313.
8. Lu H, Ge Y. Quantitative evaluation of oxygenation in venous vessels using T2-Relaxation-Under-Spin-Tagging MRI. Magn Reson Med 2008;60(2):357-363.
9. Wagner M, Jurcoane A, Volz S, Magerkurth J, Zanella FE, Neumann-Haefelin T, Deichmann R, Singer OC, Hattingen E. Age-related changes of cerebral autoregulation: new insights with quantitative T2'-mapping and pulsed arterial spin-labeling MR imaging. AJNR Am J Neuroradiol 2012;33(11):2081-2087.
10. Derdeyn CP, Videen TO, Yundt KD, Fritsch SM, Carpenter DA, Grubb RL, Powers WJ. Variability of cerebral blood volume and oxygen extraction: stages of cerebral haemodynamic impairment revisited. Brain 2002;125(Pt 3):595-607.
11. Watchmaker JM, Juttukonda MR, Davis LT, Scott AO, Faraco CC, Gindville MC, Jordan LC, Cogswell PM, Jefferson AL, Kirshner HS, Donahue MJ. Hemodynamic mechanisms underlying elevated oxygen extraction fraction (OEF) in moyamoya and sickle cell anemia patients. J Cereb Blood Flow Metab 2018;38(9):1618-1630.

12. Fan AP, Khalil AA, Fiebach JB, Zaharchuk G, Villringer A, Villringer K, Gauthier CJ. Elevated brain oxygen extraction fraction measured by MRI susceptibility relates to perfusion status in acute ischemic stroke. J Cereb Blood Flow Metab 2019:271678x19827944.

13. Aanerud J, Borghammer P, Chakravarty MM, Vang K, Rodell AB, Jonsdottir KY, Moller A, Ashkanian M, Vafaee MS, Iversen P, Johannsen P, Gjedde A. Brain energy metabolism and blood flow differences in healthy aging. J Cereb Blood Flow Metab 2012;32(7):1177-1187.

14. Kaku Y, Iihara K, Nakajima N, Kataoka H, Fukuda K, Masuoka J, Fukushima K, Iida H, Hashimoto N. Cerebral blood flow and metabolism of hyperperfusion after cerebral revascularization in patients with moyamoya disease. J Cereb Blood Flow Metab 2012;32(11):2066-2075.

15. P. DC, O. VT, L. GR, J. PW. Comparison of PET Oxygen Extraction Fraction Methods for the Prediction of Stroke Risk. J Nucl Med 2001;42:1195-1197.

16. Aanerud J, Borghammer P, Chakravarty MM, Vang K, Rodell AB, Jónsdottir KY, Møller A, Ashkanian M, Vafaee MS, Iversen P, Johannsen P, Gjedde A. Brain energy metabolism and blood flow differences in healthy aging. J Cereb Blood Flow Metab 2012;32(7):1177-1187.

17. Jiang D, Lin Z, Liu P, Sur S, Xu C, Hazel K, Pottanat G, Yasar S, Rosenberg P, Albert M, Lu H. Normal variations in brain oxygen extraction fraction are partly attributed to differences in end-tidal CO2. J Cereb Blood Flow Metab 2019.

18. Seiler A, Deichmann R, Pfeilschifter W, Hattingen E, Singer OC, Wagner M. T2-Imaging to Assess Cerebral Oxygen Extraction Fraction in Carotid Occlusive Disease: Influence of Cerebral Autoregulation and Cerebral Blood Volume. PLoS One 2016;11(8):e0161408.

19. Chaves C, Hreib K, Allam G, Liberman RF, Lee G, Caplan LR. Patterns of cerebral perfusion in patients with asymptomatic internal carotid artery disease. Cerebrovasc Dis 2006;22(5-6):396-401.

20. Care AISNCo. The Internet Stroke Centre: Brain Anatomy. Volume 2019: Genentech Inc.

21. Kilic T, Akakin A. Anatomy of cerebral veins and sinuses. Front Neurol Neurosci 2008;23:4-15.

22. Ferro JM, Canhao P, Stam J, Bousser MG, Barinagarrementeria F. Prognosis of cerebral vein and dural sinus thrombosis: results of the International Study on Cerebral Vein and Dural Sinus Thrombosis (ISCVT). Stroke 2004;35(3):664-670.

23. Alvis-Miranda HR, Milena Castellar-Leones S, Alcala-Cerra G, Rafael Moscote-Salazar L. Cerebral sinus venous thrombosis. J Neurosci Rural Pract. Volume 4; 2013. p 427-438.

24. Mintun MA, Raichle ME, Martin WR, Herscovitch P. Brain oxygen utilization measured with O-15 radiotracers and positron emission tomography. J Nucl Med 1984;25(2):177-187.

25. Lloyd-Fox S, Papademetriou M, Darboe MK, Everdell NL, Wegmuller R, Prentice AM, Moore SE, Elwell CE. Functional near infrared spectroscopy (fNIRS) to assess cognitive function in infants in rural Africa. Scientific Reports 2014;4:4740.

26. Balardin JB, Zimeo Morais GA, Furucho RA, Trambaiolli L, Vanzella P, Biazoli C, Sato JR. Imaging Brain Function with Functional Near-Infrared Spectroscopy in Unconstrained Environments. Front Hum Neurosci 2017;11.

27. Gomori JM, Grossman RI, Yu-Ip C, Asakura T. NMR Relaxation Times of Blood: Dependence on Field Strength, Oxidation State, and Cell Integrity. Journal of Computer Assisted Tomography 1987;11:684-690.

28. Silver MS, Joseph RI, Chen C-N, Sank VJ, Hoult DI. Selective population inversion in NMR. Nature 2019;310(5979):681-683.

29. Carr H, Purcell E. Effects of Diffusion on Free Precession in Nuclear Magnetic Resonance Experiments. Phys Rev 1954;94(3).

30. Meiboom S, Gill D. Modified Spin-Echo Method for Measuring Nuclear Relaxation Times. 1958;29.

31. Whitaker C. Evaluation of Hahn, CPMG, and Combined Spin Echo Analysis at 8 Tesla MRI (*Unpublished doctoral thesis)*. Ohio State University; 2004.

32. MH L, R F. Compensation for pulse imperfections in NMR spin-echo experiments. Journal of Magnetic Resonance 1981;43(1):65-80.

33. Brittain JH, Hu BS, Wright GA, Meyer CH, Macovski A, Nishimura DG. Coronary angiography with magnetization-prepared T2 contrast. Magn Reson Med 1995;33(5):689-696.

34. Nishimura DG, Macovski A, Jackson JI, Hu RS, Stevick CA, Axel L. Magnetic resonance angiography by selective inversion recovery using a compact gradient echo sequence. Magn Reson Med 1988;8(1):96-103.

35. Roemer PB, Edelstein WA, Hayes CE, Souza SP, Mueller OM. The NMR phased array. Magn Reson Med 1990;16(2):192-225.

36. Jakob PM, Griswold MA, Edelman RR, Sodickson DK. AUTO-SMASH: a self-calibrating technique for SMASH imaging. SiMultaneous Acquisition of Spatial Harmonics. Magma 1998;7(1):42-54.

37. Walsh DO, Gmitro AF, Marcellin MW. Adaptive reconstruction of phased array MR imagery. Magn Reson Med 2000;43(5):682-690.

38. Rosen B, Wedeen V, TJ. B. Selective Saturation NMR Imaging. Journal of Computer Assisted Tomography 1984;8:813-818.

39. Haase A, Frahm J, Hanicke W, Matthaei D. 1H NMR chemical shift selective (CHESS) imaging. Phys Med Biol 1985;30(4):341-344.

40. Ogg RJ, Kingsley PB, Taylor JS. WET, a T1- and B1-insensitive water-suppression method for in vivo localized 1H NMR spectroscopy. J Magn Reson B 1994;104(1):1-10.

41. Young I, Hall A, Bydder G. The Design of a Multiple Inversion Recovery Sequence for T1 Measurement. Magnetic Resonance in Medicine 1987;5:99-108.

42. Dixon WT, Sardashti M, Castillo M, Stomp GP. Multiple inversion recovery reduces static tissue signal in angiograms. Magn Reson Med 1991;18(2):257-268.

43. Mani S, Pauly J, Conolly S, Meyer C, Nishimura D. Background suppression with multiple inversion recovery nulling: Applications to projective angiography. Magnetic Resonance in Medicine 1997;37(6).

44. Ye FQ, Frank JA, Weinberger DR, McLaughlin AC. Noise reduction in 3D perfusion imaging by attenuating the static signal in arterial spin tagging (ASSIST). Magn Reson Med 2000;44(1):92-100.

45. Gunther M, Oshio K, Feinberg DA. Single-shot 3D imaging techniques improve arterial spin labeling perfusion measurements. Magn Reson Med 2005;54(2):491-498.

46. Hashemi R, Bradley W, Lisanti C. MRI: The Basics: Lippincott Williams and Wilksins; 2010. 400 p.

47. Pattany PM, Phillips JJ, Chiu LC, Lipcamon JD, Duerk JL, J.M. M, Mohapatra SN. Motion Artifact Suppression Technique (MAST) for MR Imaging. Journal of Computer Assisted Tomography 1987;11(3):369-377.

48. McGehee BE, Pollock JM, Maldjian JA. Brain perfusion imaging: How does it work and what should I use? J Magn Reson Imaging 2012;36(6):1257-1272.

49. Gordon Y, Partovi S, Müller-Eschner M, Amarteifio E, Bäuerle T, Weber MA, Kauczor HU, Rengier F. Dynamic contrast-enhanced magnetic resonance imaging: fundamentals and application to the evaluation of the peripheral perfusion. Cardiovasc Diagn Ther. Volume 4; 2014. p 147-164.

50. Jahng GH, Li KL, Ostergaard L, Calamante F. Perfusion Magnetic Resonance Imaging: A Comprehensive Update on Principles and Techniques. Korean J Radiol 2014;15(5):554-577.

51. Garcia J, Liu SZ, Louie AY. Biological effects of MRI contrast agents: gadolinium retention, potential mechanisms and a role for phosphorus. Philos Trans A Math Phys Eng Sci. Volume 375; 2017.

52. Wong EC. Vessel-encoded arterial spin-labeling using pseudocontinuous tagging. Magn Reson Med 2007;58(6):1086-1091.

53. Dai W, Garcia D, de Bazelaire C, Alsop DC. Continuous flow-driven inversion for arterial spin labeling using pulsed radio frequency and gradient fields. Magn Reson Med 2008;60(6):1488-1497.

54. Wong EC, Cronin M, Wu WC, Inglis B, Frank LR, Liu TT. Velocity-selective arterial spin labeling. Magn Reson Med 2006;55(6):1334-1341.

55. Norris DG, Schwarzbauer C. Velocity selective radiofrequency pulse trains. J Magn Reson 1999;137(1):231-236.

56. Petersen ET, Zimine I, Ho YC, Golay X. Non-invasive measurement of perfusion: a critical review of arterial spin labelling techniques. Br J Radiol 2006;79(944):688-701.

57. Ogawa S, Lee TM, Nayak AS, Glynn P. Oxygenation-sensitive contrast in magnetic resonance image of rodent brain at high magnetic fields. Magn Reson Med 1990;14(1):68-78.

58. Blockley NP, Griffeth VEM, Simon AB, Buxton RB. A review of calibrated blood oxygenation level-dependent (BOLD) methods for the measurement of task-induced changes in brain oxygen metabolism. NMR Biomed 2013;26(8):987-1003.

59. Davis TL, Kwong KK, Weisskoff RM, Rosen BR. Calibrated functional MRI: mapping the dynamics of oxidative metabolism. Proc Natl Acad Sci USA 1998;95(4):1834-1839.

60. van Zijl PC, Eleff SM, Ulatowski JA, Oja JM, Ulug AM, Traystman RJ, Kauppinen RA. Quantitative assessment of blood flow, blood volume and blood oxygenation effects in functional magnetic resonance imaging. Nat Med 1998;4(2):159-167.

61. Li TQ, Haefelin TN, Chan B, Kastrup A, Jonsson T, Glover GH, Moseley ME. Assessment of hemodynamic response during focal neural activity in human using bolus tracking, arterial spin labeling and BOLD techniques. Neuroimage 2000;12(4):442-451.

62. Hoge RD. Calibrated FMRI. Neuroimage 2012;62(2):930-937.

63. Bulte DP, Kelly M, Germuska M, Xie J, Chappell MA, Okell TW, Bright MG, Jezzard P. Quantitative measurement of cerebral physiology using respiratory-calibrated MRI. Neuroimage 2012;60(1):582-591.

64. Germuska M, Merola A, Murphy K, Babic A, Richmond L, Khot S, Hall JE, Wise RG. A forward modelling approach for the estimation of oxygen extraction fraction by calibrated fMRI. Neuroimage 2016;139:313-323.

65. Blockley NP, Griffeth VEM, Simon AB, Dubowitz DJ, Buxton RB. Calibrating the BOLD response without administering gases: Comparison of hypercapnia calibration with calibration using an asymmetric spin echo. Neuroimage 2015;104:423-429.

66. Golay X, Silvennoinen MJ, Zhou J, Clingman CS, Kauppinen RA, Pekar JJ, van Zijl PC. Measurement of tissue oxygen extraction ratios from venous blood T(2): increased precision and validation of principle. Magn Reson Med 2001;46(2):282-291.

67. Lu H, Xu F, Grgac K, Liu P, Qin Q, van Zijl P. Calibration and validation of TRUST MRI for the estimation of cerebral blood oxygenation. Magn Reson Med 2012;67(1):42-49.

68. Bolar DS, Rosen BR, Sorensen AG, Adalsteinsson E. QUantitative Imaging of eXtraction of oxygen and TIssue consumption (QUIXOTIC) using venular-

targeted velocity-selective spin labeling. Magn Reson Med 2011;66(6):1550-1562.

69. Guo J, Wong EC. Venous Oxygenation Mapping using Velocity-Selective Excitation and Arterial Nulling (VSEAN). Magn Reson Med 2012;68(5):1458-1471.

70. Krishnamurthy LC, Liu P, Ge Y, Lu H. Vessel-specific quantification of blood oxygenation with T2-relaxation-under-phase-contrast MRI. Magn Reson Med 2014;71(3):978-989.

71. Krishnamurthy LC, Mao D, King KS, Lu H. Correction and optimization of a T2-based approach to map blood oxygenation in small cerebral veins. Magn Reson Med 2016;75(3):1100-1109.

72. Jordan LC, Gindville MC, Scott AO, Juttukonda MR, Strother MK, Kassim AA, Chen SC, Lu H, Pruthi S, Shyr Y, Donahue MJ. Non-invasive imaging of oxygen extraction fraction in adults with sickle cell anaemia. Brain 2016;139(Pt 3):738-750.

73. Thomas BP, Sheng M, Tseng BY, Tarumi T, Martin-Cook K, Womack KB, Cullum MC, Levine BD, Zhang R, Lu H. Reduced global brain metabolism but maintained vascular function in amnestic mild cognitive impairment. J Cereb Blood Flow Metab. Volume 37; 2017. p 1508-1516.

74. Peng SL, Dumas JA, Park DC, Liu P, Filbey FM, McAdams CJ, Pinkham AE, Adinoff B, Zhang R, Lu H. Age-related increase of resting metabolic rate in the human brain. Neuroimage 2014;98:176-183.

75. Xu F, Uh J, Brier MR, Hart J, Yezhuvath US, Gu H, Yang Y, Lu H. The influence of carbon dioxide on brain activity and metabolism in conscious humans. J Cereb Blood Flow Metab. Volume 31; 2011. p 58-67.

76. Xu F, Liu P, Pekar JJ, Lu H. Does acute caffeine ingestion alter brain metabolism in young adults? Neuroimage 2015;110:39-47.

77. Liu P, Xu F, Lu H. Test-retest reproducibility of a rapid method to measure brain oxygen metabolism. Magn Reson Med 2013;69(3):675-681.

78. Liu P, Dimitrov I, Andrews T, Crane DE, Dariotis JK, Desmond J, Dumas J, Gilbert G, Kumar A, Maclntosh BJ, Tucholka A, Yang S, Xiao G, Lu H. Multisite evaluations of a T2 -relaxation-under-spin-tagging (TRUST) MRI technique to measure brain oxygenation. Magn Reson Med 2016;75(2):680-687.

79. Mahmoud H, Buchanan C, Francis ST, Selby NM. Imaging the kidney using magnetic resonance techniques: structure to function. Curr Opin Nephrol Hypertens 2016;25(6):487-493.

80. Xu F, Uh J, Liu P, Lu H. On improving the speed and reliability of T2-relaxation-under-spin-tagging (TRUST) MRI. Magn Reson Med 2012;68(1):198-204.

81. Gallichan D. Measuring cerebral blood flow using arterial spin labelling with magnetic resonance imaging (*Unpublished doctoral thesis)*: University of Oxford; 2007.

82. Golay X, Petersen E, F H. Pulsed star labeling of arterial regions (PULSAR): A robust regional perfusion technique for high field imaging. Magnetic Resonance in Medicine 2004;53(1):15-21.

83. Stout JN, Tisdall MD, McDaniel P, Gagoski B, Bolar DS, Grant PE, Adalsteinsson E. Assessing the effects of subject motion on T2 relaxation under spin tagging (TRUST) cerebral oxygenation measurements using volume navigators. Magn Reson Med 2017;78(6):2283-2289.

84. Jenkinson M, Bannister P, Brady M, Smith S. Improved optimization for the robust and accurate linear registration and motion correction of brain images. Neuroimage 2002;17(2):825-841.

85. McRobbie D, Moore E, Graves M, Prince M. MRI: From Picture to Proton. United States of America: Cambridge University Press; 2006.

86. Silverthorn DU. Human Physiology: An Integrated Approach: Pearson; 2013.

87. De Vis JB, Hendrikse J, Groenendaal F, de Vries LS, Kersbergen KJ, Benders MJ, Petersen ET. Impact of neonate haematocrit variability on the longitudinal relaxation time of blood: Implications for arterial spin labelling MRI. Neuroimage Clin 2014;4:517-525.

88. Grgac K, van Zijl PC, Qin Q. Hematocrit and oxygenation dependence of blood (1)H(2)O T(1) at 7 Tesla. Magn Reson Med 2013;70(4):1153-1159.

89. Qin Q, Strouse JJ, van Zijl PC. Fast Measurement of Blood T1 in the Human Jugular Vein at 3 Tesla. Magn Reson Med 2011;65(5):1297-1304.

90. Shimada K, Nagasaka T, Shidahara M, Machida Y, Tamura H. In vivo measurement of longitudinal relaxation time of human blood by inversion-recovery fast gradient-echo MR imaging at 3T. Magn Reson Med Sci 2012;11(4):265-271.

91. Varela M, Hajnal JV, Petersen ET, Golay X, Merchant N, Larkman DJ. A method for rapid in vivo measurement of blood T1. NMR Biomed 2011;24(1):80-88.

92. Lu H, Clingman C, Golay X, van Zijl PC. Determining the longitudinal relaxation time (T1) of blood at 3.0 Tesla. Magn Reson Med 2004;52(3):679-682.

93. Wu WC, Jain V, Li C, Giannetta M, Hurt H, Wehrli FW, Wang DJ. In vivo Venous Blood T1 Measurement using Inversion Recovery TrueFISP in Children and Adults. Magn Reson Med 2010;64(4):1140-1147.

94. Hales PW, Kirkham FJ, Clark CA. A general model to calculate the spin-lattice (T1) relaxation time of blood, accounting for haematocrit, oxygen saturation and magnetic field strength. J Cereb Blood Flow Metab 2016;36(2):370-374.

95. Moulé AJ, Spence MM, Han S-I, Seeley JA, Pierce KL, Saxena S, Pines A. Amplification of xenon NMR and MRI by remote detection. 2003.

96. Harel E, Granwehr J, Seeley JA, Pines A. Multiphase imaging of gas flow in a nanoporous material using remote-detection NMR. Nat Mater 2006;5(4):321-327.

97. Seeley JA, Han SI, Pines A. Remotely detected high-field MRI of porous samples. J Magn Reson 2004;167(2):282-290.

98. Wong E, Guo J. VENTI: Venous Territory Imaging using Remote Sensing. 2013; Salt Lake City, Utah, USA.

99. Sezan MI, Stark H. Image restoration by the method of convex projections: part 2 applications and numerical results. IEEE Trans Med Imaging 1982;1(2):95-101.

100. Sezan M, Stark H. Tomographic image reconstruction from incomplete view data by convex projections and direct fourier inversion. IEEE Trans Med Imaging 1984;3(2):91-98.

101. Liang Z, Boda F, Constable R, Haacke E, Lauterbur P, Smith M. Constrained Reconstruction Methods in MR Imaging. Review of Magnetic Resonance in Medicine 1992;4:67-185.

102. Pauly J. Lecture Notes: Chapter 2: Partial k-Space Reconstruction. Standford University. p 11-23.